PERKIN-ELMER

OPTICAL GROUP NORWALK, CONNECTICUT

ENGINEERING REPORT NO. 9365

LASER/OPTICS TECHNIQUES
3RD INTERIM SUMMARY REPORT

DATE: APRIL 30, 1968

PREPARED FOR: GEORGE C. MARSHALL SPACE FLIGHT CENTER
NATIONAL AERONAUTICS AND SPACE ADMINISTRATION
HUNTSVILLE, ALABAMA

CONTRACT NO. NAS 8-20115

Prepared by: Morley S. Lipsett
Morley S. Lipsett, Senior Physicist

Approved by: H.F. Wischnia
H.F. Wischnia, Manager, Scientific Payloads

SPO 27633

Contributors

M. S. Lipsett, Project Manager

A. Fuschetto

R. C. Liu

A. M. Ledger

L. P. Mott

W. N. Peters

R. R. Austin

G. Gottesman

E. R. Schlesinger

TABLE OF CONTENTS

TABLE OF CONTENTS (Continued)

TABLES

LIST OF ILLUSTRATIONS

LIST OF ILLUSTRATIONS (Continued)

LIST OF ILLUSTRATIONS (Continued)

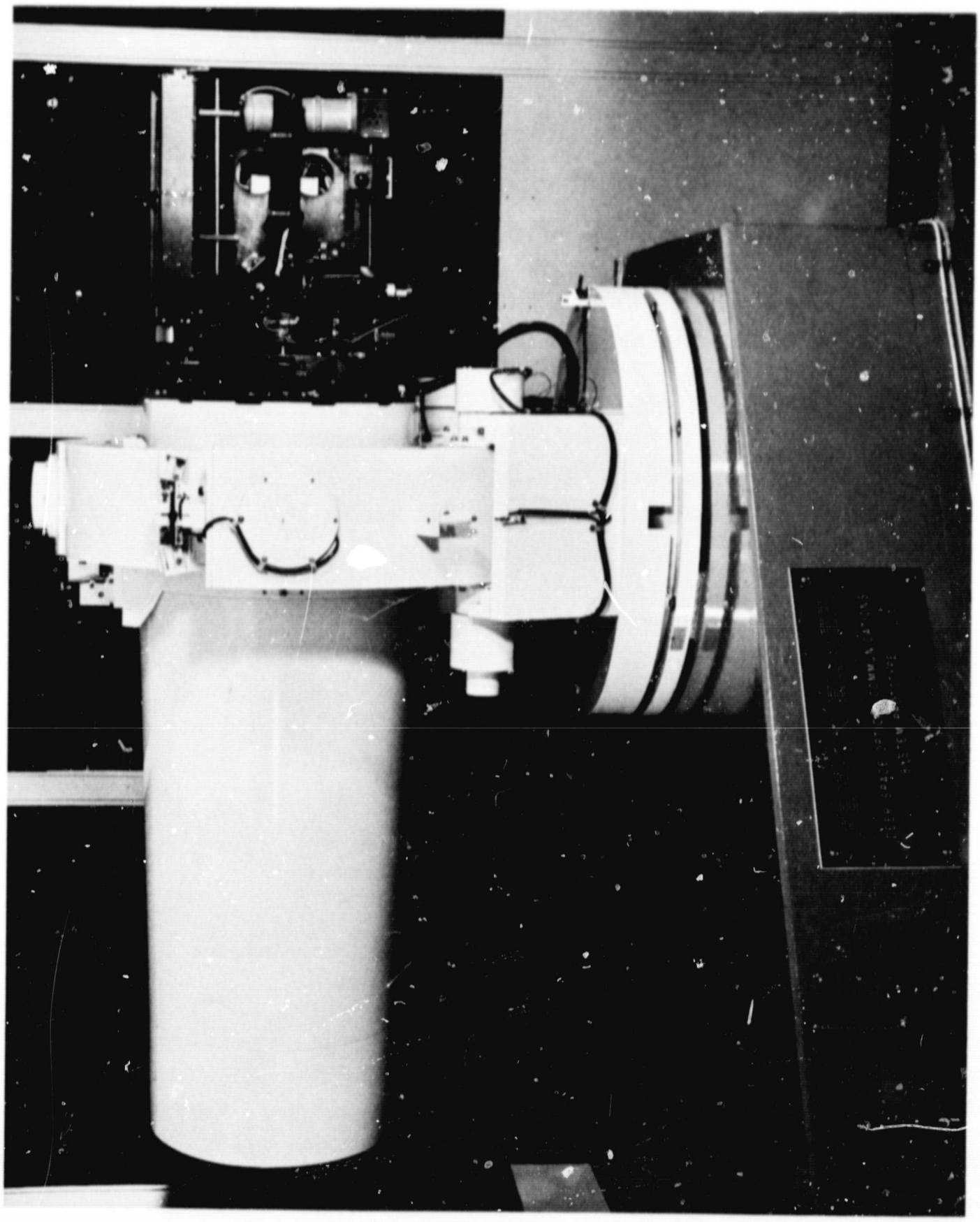

Figure 1-1. Laboratory Prototype Deep-Space Optical Communications System

SECTION I

SUMMARY

This report summarizes recent progress in the development of new optical instrumentation intended to achieve high-data-rate communication from deep space to earth. Previous work[1,2] dealt with the development of key hardware for a deep-space optical communications system as well as with certain basic problems associated with the concept of optical duplexing.

This work was continued under Contract NAS 8-20115, and the laboratory prototype communications system shown in Figure 1-1 was designed, packaged, manufactured, assembled, and tested.[3] This equipment comprises a laser telescope communications package and a four-axis mount, and is operated in conjunction with an earth beacon simulator. The laboratory setup is designed for performing experiments to evaluate the laser telescope under simulated space conditions.

A special feature of the instrumentation is that all key optical components are now reflective and hence are independent of wavelength or choice of laser. As new and more efficient lasers are developed in the future, the system can readily be modified to accommodate them.

The goal of the work described in this report was to develop an essentially complete laboratory version of a deep-space optical communications system along with its associated simulation and test instrumentation. The purpose was to set the stage for an extensive program of laboratory testing by which this new technology could be thoroughly validated and set in perspective for the designers of future spacecraft.

---

[1] Perkin-Elmer Engineering Report No. 8387 (Laser/Optics Techniques, First Interim Summary Report)

[2] Perkin-Elmer Engineering Report No. 8631 (Laser/Optics Techniques, Second Interim Summary Report)

[3] M.S. Lipsett, Instrumentation for Deep-Space Optical Communication, J. Opt. Soc. Am. 58 732 (1968)

SECTION II

OPTICAL DESIGN

2.1 INTRODUCTION

A major redesign of the transceiver optical configuration was carried out as the result of such newly imposed design goals as:

- showing feasibility of transmitter operation at other wavelengths, 10.6 microns in particular
- developing a new, all-reflective, lightweight, and compact version of the transfer lens
- rearranging the optics for efficient packaging of the "behind the telescope" equipment
- developing a new fine-guidance system of significantly reduced volume and weight and with other improved characteristics.

2.2 OPTICAL CONFIGURATION

The basic form of the redesigned transceiver optics is shown in Figure 2-1, where for clarity details of the fine-guidance and coarse-acquisition optics are not shown. The complete optical layout is shown in Figure 2-2. The main features of this design are as follows:

A plane mirror with an axial perforation is located at the focal plane of the telescope and is slightly inclined (the tilt is exaggerated in the figure) away from the axis as shown. The perforation serves as a field stop to admit incoming beacon light when it falls within the 2-arc-minute diameter field of view of the optical transceiver equipment. Beacon light so admitted is next collimated by a fixed tertiary mirror and reflected back toward the perforated

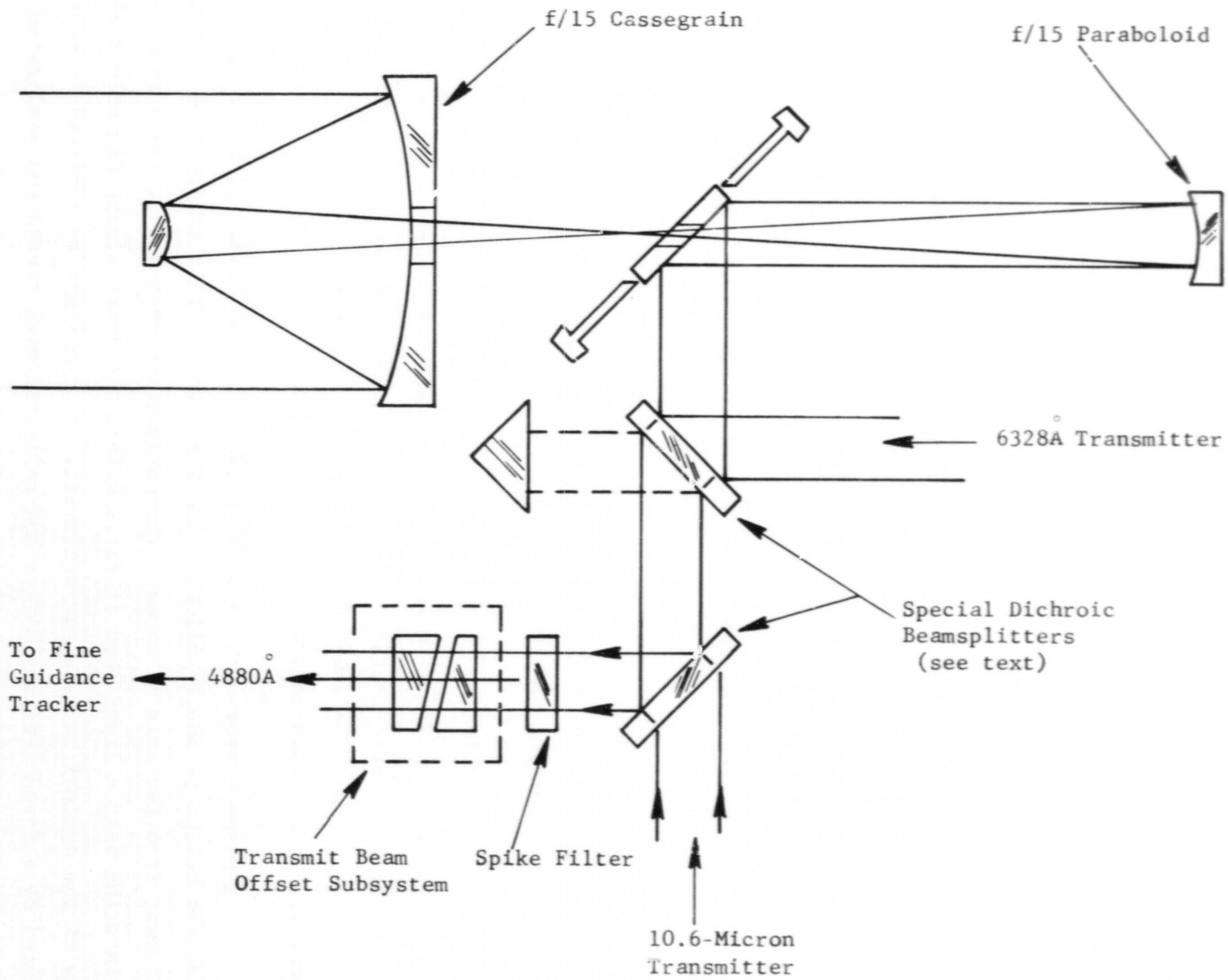

Figure 2-1. Optical Layout of Reflective Transfer Lens Version of Laser Telescope. Coarse Acquisition Subsystem Not Shown.

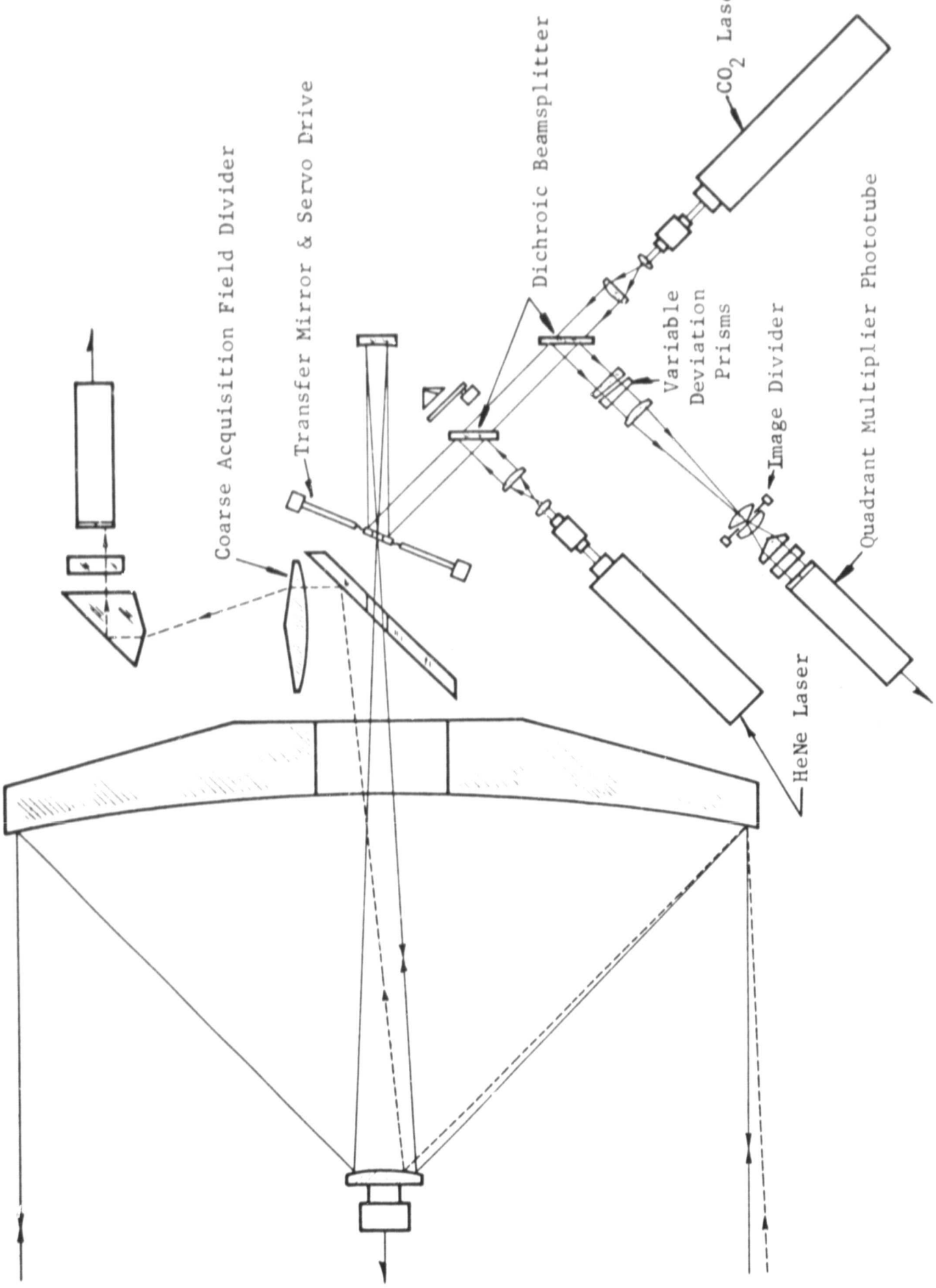

Figure 2-2. Optical Layout of Laser Telescope

flat which deflects the collimated beam toward two dichroic beamsplitters. The tertiary mirror is confocal with the Cassegrain focus and exactly compensates for the coma which, as is well known, limits the usable field of a conventional Cassegrain telescope. This three-mirror combination is therefore properly termed an aplanatic system (i.e., zero spherical aberration and zero coma), which is an added bonus of the new optical configuration.

The first beamsplitter transmits the beacon light; the second reflects it into the reimaging optics of the fine guidance system prior to which the beacon light is transmitted by a noise rejection filter and by the optical wedges of the transmit beam offset subsystem.

Collimated transmit light at 6328 Å is reflected by the first beamsplitter; then it follows a reverse path out the telescope as shown. Similarly, transmit light at 10.6 microns is transmitted by both beamsplitters. Then it, too, follows a reverse path from the perforated mirror to the tertiary mirror, through the perforation, and out the telescope.

2.3 TRANSFER MIRROR OPTICS

The perforated mirror is pivoted electrically about two crossed axes in such a way as to serve exactly as the previously refractive image transfer element. We therefore term it a "transfer mirror". A fuller description of the transfer mirror (and its associated servo drives) is given in Sections III and VI. Here we summarize its salient optical characteristics.

The transfer mirror is located at an image of the entrance pupil of the telescope. Hence, by matching the transmit beam to this pupil, the conditions of illumination of the telescope are independent of angular motions of the transfer mirror, i.e., the transfer mirror in this configuration steers the transmit beam exactly as if the telescope itself were being steered.

The transfer mirror is 12.7 mm in diameter; the diameter of the central perforation is 3.56 mm to serve as the field stop for the 2-arc-minute diameter fine-guidance field of view. The pupil diameter at the transfer mirror is 8 mm. This value was chosen (a) to match the central perforation of the

transfer mirror to the central obscuration of the telescope pupil, (b) to match the minimum acceptance angle of narrow-band predetection filters in the region of collimated light, and (c) to strike a balance between minimized clear apertures of the beamsplitters and minimized power densities at the beamsplitters from the 10.6-micron transmit laser.

The marginal rays at the transfer mirror corresponding to the 2-arc-minute fine-guidance field of view subtend an angle of 100 arc-minutes. But, as a ray is deflected through twice the deflection of a mirror on which it is incident, the transfer mirror must pivot only ±25 arc-minutes about two orthogonal axes to have a range corresponding to the 2-arc-minute fine-guidance field.

It should be noted that system focus is unaffected by translations of the transfer mirror since it is used in a region of collimated light. However, deflections of the transfer mirror will, in general, cause field rotations, which effect is a function of the optical geometry. In particular, if the angle between the telescope axis and the normal to the transfer mirror is θ, then for a transfer mirror deflection φ, the field rotates by an amount Ψ, where

$$\Psi \sim \tan^{-1} (2\varphi \sin\theta)$$

Because of this effect, the optics were arranged so that the transfer mirror operates at nearly normal incidence; specifically θ = 7.5 degrees (0.131 radian). Thus the maximum field rotation is

$$\begin{aligned} \Psi &\sim \pm \tan^{-1}(50 \times 2.91 \times 10^{-4} \times 0.131) \\ &= \tan^{-1} (1.9 \times 10^{-3}) \\ &\sim \pm 1.9 \times 10^{-3} \text{ radian } (\pm 6.5 \text{ arc-minutes}) \end{aligned}$$

This value is to be compared with a tolerance of ±2 degrees and ±13.5 arc-minutes for a synchronous orbit and Martian probe mission, respectively (see, for example, page 2-22 of Perkin-Elmer Engineering Report No. 8631).

2.4 TRANSMIT BEAM OFFSET

Servo-controlled Risley prisms serve to carry out boresight alignment and transmit beam offset functions. These have been taken out of the

transmit channel where they were originally located (Case I) and put into the receive channel (Case II) as part of the new optical configuration. This substitution is entirely optically equivalent to the previous arrangement.

In Case I, remote adjustment of the prism pair causes the transmit channel to be accurately offset from the receiver line of sight; and, in Case II, the receiver line of sight is offset from the transmit channel. An important asset of the Case II arrangement, which may be termed "an offset-tracker" configuration, is that the offset angle is independent of the wavelength of the transmitted beam. Offset tracking results in an intended interaction between the beam-offset servos and the transfer lens servos. This interaction sets bounds on the relative bandwidths of these servos. In particular, it is necessary that the response of the transfer mirror be much faster than the response of the prism servos.

2.5 BEAMSPLITTERS

Two unusual dichroic beamsplitter elements are specified in the layout shown in Figures 2-1 and 2-2. Ideally, one of these should have a transmittance of unity at 10.6 microns and a reflectivity of unity at 4880 Å. The other should have a transmittance of unity at both 4880 Å and 10.6 microns and reflectivity of unity at 6328 Å. In practice, we were able to approach these requirements closely enough during preliminary development to ensure the feasibility of the new optical design. For example, in preliminary experiments one beamsplitter was made having a transmittance of 82% at 10.6 microns, and reflectivity in excess of 99% at 4880 Å. A second beamsplitter was made having transmittances of 91% and 81% at 10.6 microns and 4880 Å, respectively, and a reflectivity in excess of 96% at 6328 Å, peaking to greater than 99% at 6500 Å. The reflectivity peak was readily shifted up to 6328 Å in future "runs" of this beamsplitter design.

Previous work, which led to the development of suitable dichroic beamsplitters for the earlier version of the Laser/Optics Techniques breadboard, also showed that scattered light at the beamsplitters was the primary source of channel crosstalk. We, therefore, carried out a systematic investigation of beamsplitter design from the scatter point of view prior to manufacture of the

beamsplitters for the new optical system.[1] A description of this work is given in Appendix A. Scatter measurements were made on optical surfaces prepared in a variety of ways and on multilayer dielectric coatings of the type required for the laser telescope. The additional knowledge gained was used to select fabrication techniques for the dichroic beamsplitters, which minimized the effect of scatter on channel separation.

Another fundamental aspect of dichroic beamsplitter design for the revised optical design of the laser telescope arises from the provision of a high-power CO_2 laser, 10.6-micron transmit channel.

In particular, the two beamsplitters are situated in the 10.6-micron channel in such a way that they must transmit a high-energy-density 10.6-micron beam without significant absorption losses. Absorption is the same as an ohmic loss and results in local heating of the beamsplitter substrate. Such heating is essentially non-uniform and will lead to an optical figure error at each surface of the beamsplitters. This, in turn, can result in appreciable degradation of the optical performance of the laser telescope. A study was therefore carried out to assess optical degradation of a beamsplitter for an incident CO_2 laser beam.

It was found theoretically that the effect would be significant for a 2-mm diameter, 0.5-watt CO_2 laser beam, but would be tolerable for an 8-mm diameter beam. Experimental measurements were made which confirmed this result. The experiment was conducted by forming a Fizeau interferometer at 6328 Å with a beamsplitter and a reference flat while the beamsplitter was exposed to various beam intensities from a commercial Perkin-Elmer Co_2 laser.

A report on this is included as Appendix B of this report. The principal conclusion is that several materials exist to support the design of an optical transceiver capable of operation at 10.6 microns, 6328 Å, and 4880 Å. The main choice is between barium fluoride, which absorbs slightly at 10:6 microns, and sodium chloride, which has negligible absorption at 10.6 microns but unfortunately is highly hygroscopic. Because it is much less hygroscopic than sodium chloride, barium fluoride was the material chosen for the laboratory-based laser telescope experiments. Its optical limitations in the presence of a high-power CO_2 laser beam are discussed in the appendix.

---

[1] R.R. Austin and L.P. Mott, Investigation of Low-Scatter Dichroic Beamsplitters and Their Design, J. Opt.Soc.Am. 58 736 (1968).

It is important to note that barium fluoride proved to be an extremely difficult material to fabricate with the interferometric precision as well as the low surface scatter needed for the laser telescope. Possibly this was due to the softness of the material and is likely to be a difficulty with sodium chloride substrates.

2.6 FINE-GUIDANCE OPTICS

The fine-guidance system has been redesigned using a new type of optical image divider and a quadrant multiplier phototube (QMP) for image position sensing.[2] The image-splitting optics are a variation on the Stratoscope II approach and rely on the sharp intersection of optical surfaces to effect image division with negligible light loss. In combination with a quadrant multiplier phototube, the new design for the fine-guidance optics offers the advantages of compactness and simplicity over the four-photomultiplier approach used previously.

This approach is especially suited to laser-beacon tracking. For example, the source can be chopped in square-wave fashion by switching from left to right circularly polarized light. Each state can subsequently be detected by a separate QMP for twofold detector redundancy without additional signal loss. Additional features of the QMP approach vis a vis other candidates are summarized in Table 2-1.

The simplified schematic of the fine-guidance portion of the optics (Figure 2-3) shows an on-axis diffraction image focused between the two elements of the field divider. The image is divided into four parts and the four emerging cones of light are brought back parallel to the optical axis by the use of a pyramid-shaped field corrector. This allows the placement of a narrow-band filter in the optical path since the energy is now passed through the filter at near normal incidence. The two-element image divider also serves as a field lens to image the entrance pupil of the optical system (primary mirror) onto the four quadrants of the photomultiplier tube. Given the size of the entrance

---

[2] R.C. Liu, M.S. Lipsett, and A.M. Ledger, Fine-Error Sensor for Null-Tracking Diffraction Images, J. Opt.Soc.Am. 58 718 (1968)

TABLE 2-1

COMPARISON OF IMAGE POSITION SENSORS FOR TRANSFER LENS SERVO

Device Description	Properties	Important Consequences of Properties
1. Optical Image Divider plus four photomultipliers. (ref. 1)	Image division takes place at intersection of optically polished surfaces. Useful image-divider apertures in excess of 1.5 inches can readily be obtained with very little light loss due to bluntness of surface intersections; i.e., the apex of a typical image divider can be manufactured to near perfect sharpness. Photomultipliers exposed instantaneously to entire field of view.	Each segment of quadrisected image falls on its own respective photomultiplier. Duty cycle of each photomultiplier can be 100% for maximum utilization of signal light. An insignificant amount of light is lost when image is centered on optical divider. May require a field stop for reduction of background light. For example, an iris diaphragm can be located close to the optical image divider so as to act as a variable field stop, and expose the photomultipliers to an adjustable field of view.
2. Optical Image Divider plus a single photomultiplier; quadrant encoding by a mechanical chopper. (ref. 2)	Optical properties as discussed in 1. A mechanical device, such as a motor-driven chopping wheel, or a tuning fork, is used to multiplex the intensity of all segments of an optically divided field for detection by a single photomultiplier.	Because signal is chopped, maximum duty cycle for one detector is 50%. However, two detectors may be arranged in a redundant configuration, such that the combined duty cycle is 100%. Questions may be raised as to the reliability of mechanical choppers. Tuning fork choppers may be used to advantage here.
3. Optical Image Divider used with a Quadrant Multiplier phototube. (Ref. 3)	Optical properties as for 1 and 2. The Quadrant Multiplier Phototube has been space-qualified. Multiplexing of the intensities of the segments of the optically divided image is carried out electronically by simple switching circuitry. For the special case of tracking a laser beacon, two PMT's can be used in a scheme that achieves detector redundancy without additionally sacrificing the signal-to-noise ratio.	Scan mode described in Ref. 3 produces a duty cycle of 50%. Thus, ratios of signal to noise in signal, and signal to background noise are $1/\sqrt{2}$ times the ratios attainable if all the signal is detected all the time (condition for maximum S/N). No moving parts are used. The mechanical configuration is simple and compact. The cathode switching frequency, the chopping frequency of the beacon light, and the transfer lens servo bandwidth must be mutually compatible.

References:

1. Perkin-Elmer Engineering Report No. 8387, Laser/Optics Techniques Summary Report.

2. Perkin-Elmer Engineering Report No. 8346, Princeton Advanced Satellite Study.

3. Perkin-Elmer Engineering Report No. 8631, Laser/Optics Techniques 2nd Interim Summary Report.

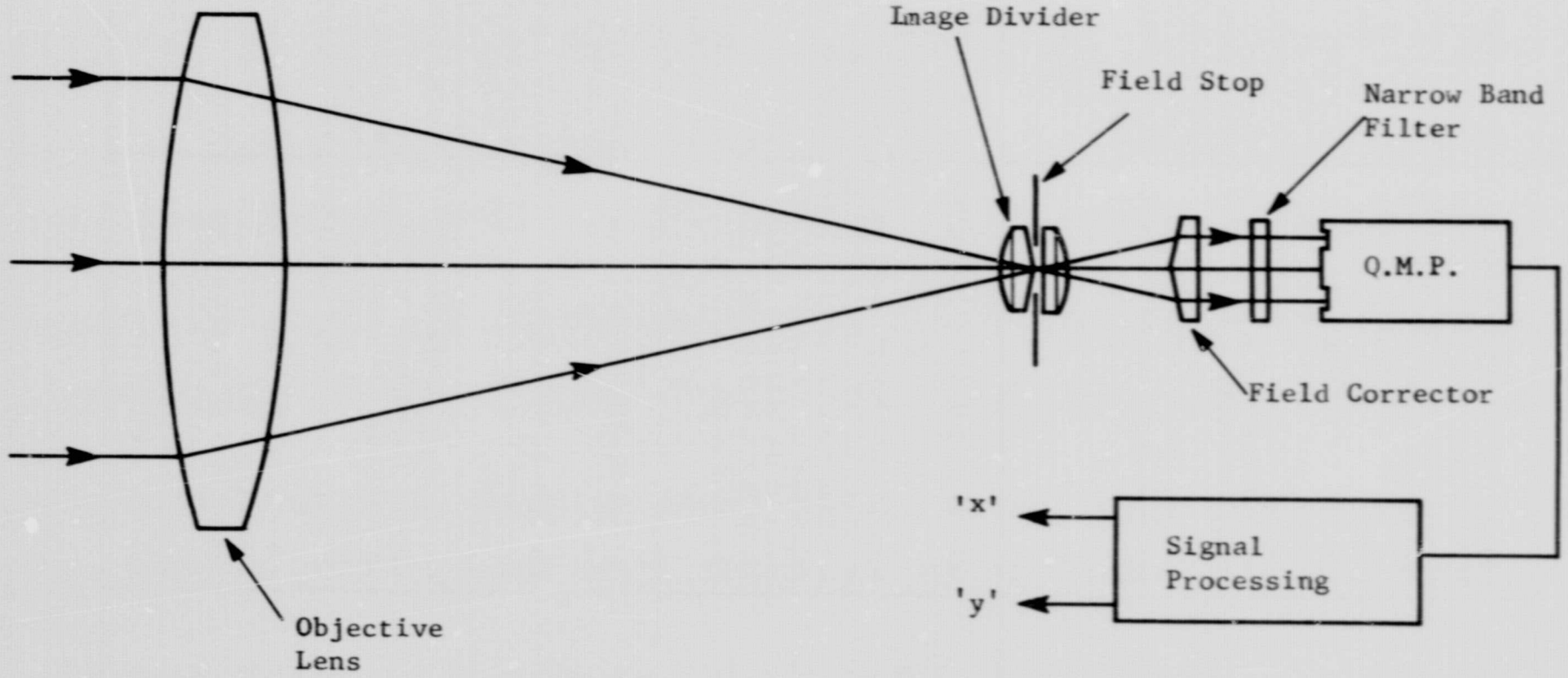

Figure 2-3. Fine-Guidance Portion of Optical System

pupil (or a relayed image of the entrance pupil) D, the distance of this pupil from the field divider V, and the photocathode size d, one chooses the focal length of the field lens as $f_r = dV/(d+D)$, so that the diameter of the exit pupil matches the photocathode size. The field lens is formed by the two outer surfaces of the image divider in combination (Figure 2-4), whereas the two inner surfaces are made in the form of a wedge to perform the field division. These wedges are rotated with respect to each other by 90 degrees to divide the field into four quadrants.

The advantages of this type of field divider over a conventional pyramid type are twofold:

1. The optical elements can be fabricated to have razor-sharp edges since we are only using the intersection of two planes on each optical element. The final imaging lens is chosen to have a large image size (~ 50 microns for the f/35 focal ratio employed) enabling very precise image division to be obtained at the final focal plane.

2. The two elements are separated slightly (by less than the depth of focus) to allow a variable field stop to be placed at the final focal plane of the instrument between the elements. The field stop is constructed as two thin metal vanes (0.003 inch thick) that slide against each other and are driven by a common screw thread. The opposing edges of the vanes are notched and result in an overall field of view that is square but continuously variable from zero to the maximum included field circle required by the fine-guidance system (2 arc-minutes).

An optical field corrector is used to bend the light from the four quadrants back parallel to the main optic axis. The fabrication of this field corrector is not critical since the edges of the pyramid face and the pyramid apex are not used. Figure 2-4 traces the light from an off-axis image (dotted lines) through the system. The first wedge serves to refract the light

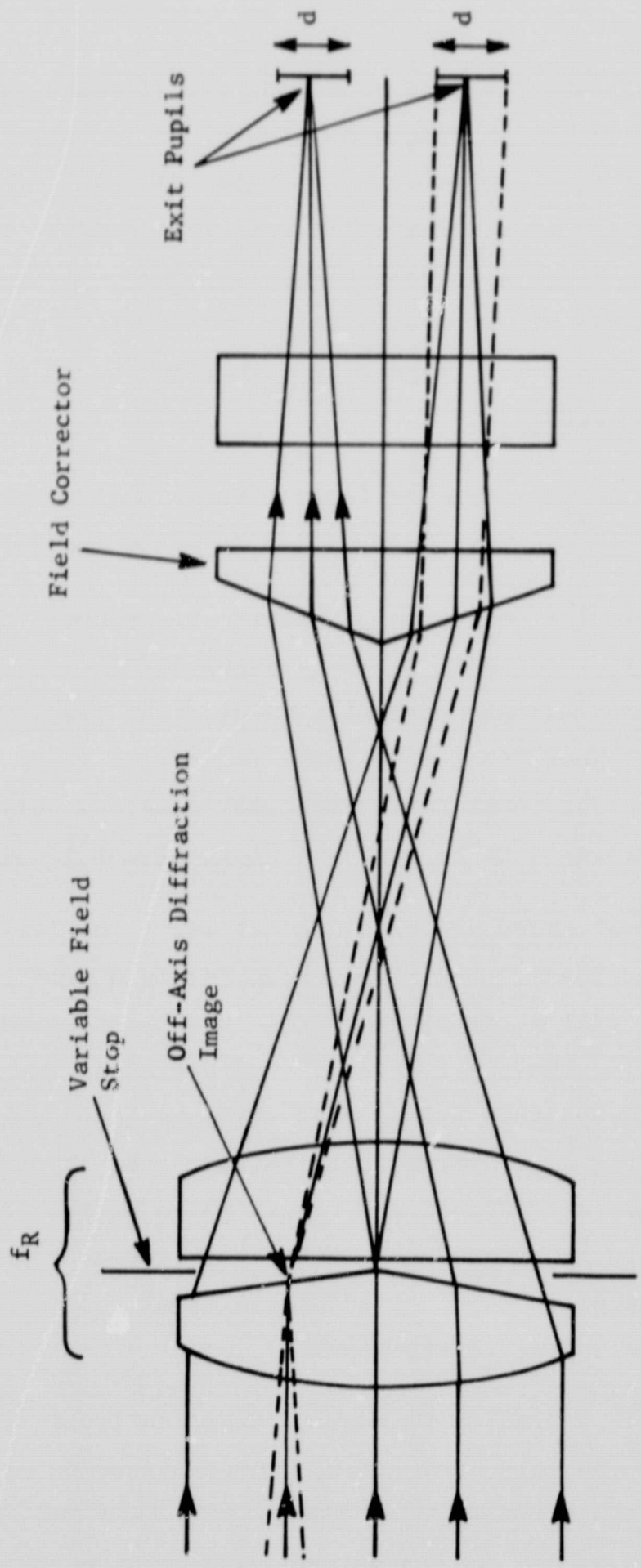

Figure 2-4. Ray Paths Through Optical Field Splitter and Field Corrector

through the system to illuminate the lower two quadrants on the phototube. The position of the image with respect to the second wedge determines the relative level of illumination of the two lower photocathodes. Figure 2-5 shows the pupil illumination from a Cassegrain telescope tracker for various positions of the diffraction image in the fine-guidance field. The position of the image is sensed electronically providing 'X' and 'Y' outputs to the transfer mirror for closed loop tracking as discussed in Section VI of this report.

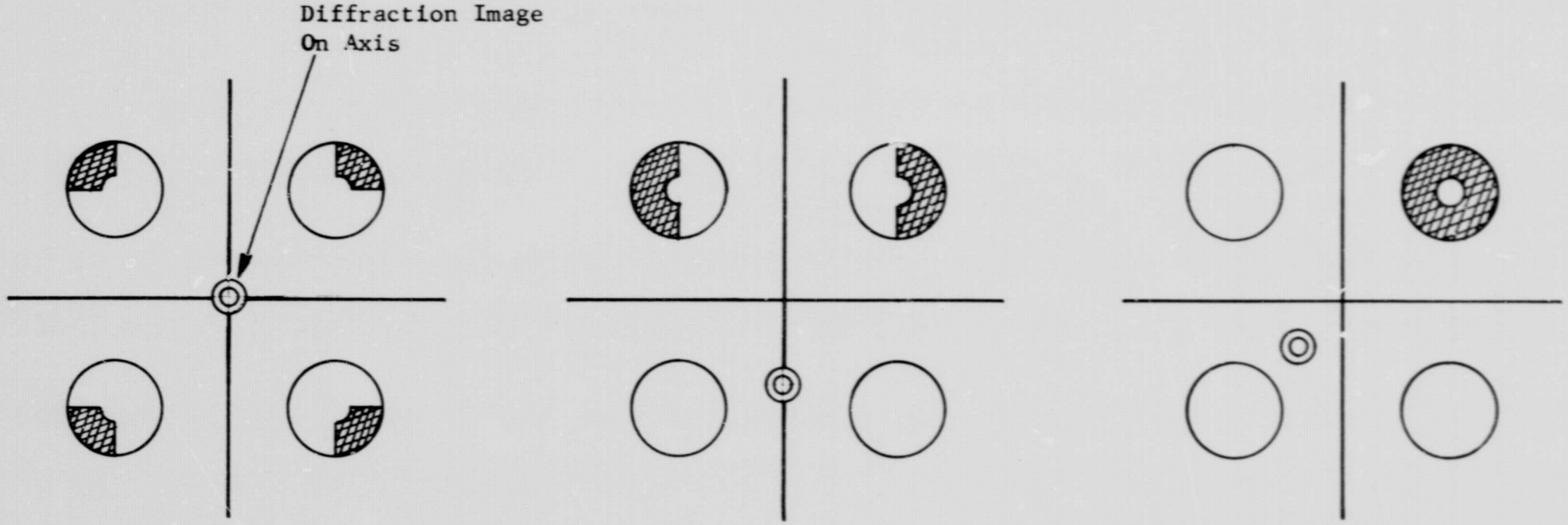

Figure 2.5 Pupil Illumination at the Quandrant Tube vs Location of Beacon Image at Image Splitter.

SECTION III

INSTRUMENT PACKAGE

3.1 INTRODUCTION

The revised design of the "behind-the-telescope" equipment which previously had been breadboarded on a 3 foot × 6 foot steel surface plate was packaged in the form of a compact 70-pound assembly that attaches to the original 16-inch telescope front end. This weight includes a dummy CO_2 laser and modulator, and the optics allow for installation of a sealed-off CO_2 laser in the future.

3.2 MECHANICAL CONFIGURATION

The mechanical layout of the instrument package is reproduced in Figures 3-1 and 3-2. The finished unit is shown attached to the rear of the telescope in Figure 1-1 and is shown in more detail with identifying callouts in Figure 3-3. The optical paths are folded and for overall compactness are at various levels with respect to the main mounting surface. All mirrors and beamsplitters operate at near normal incidence wherever practical in order to minimize changes in the polarization characteristics of the incident beams.[1]

3.3 TRANSMIT LASERS

A modified version of Perkin-Elmer's new tooling laser (helium-neon Model 5600) was selected for the laser telescope instrument package. This choice is based on the close match between the mechanical specifications of the Model 5600 laser to the alignment requirements of the system.

The Model 5600 laser features an accurately machined nose piece to which the axis of the output beam is made concentric to 0.001 inch. Beam alignment is within a few arc-minutes of the axis of the nose piece and is stable to less than 1 arc-second/hour for a 2-mm beam diameter. (This corresponds to an angular stability at the output of the laser telescope of

---

[1] W.N. Peters and R.J. Arguello, Fading and Polarization Noise of a PCM/PL System, IEEE Journal of Quantum Electronics, QE-3 No. 11, 532, (1967)

0.005 arc-second/hour.) The overall size of the Model 5600 laser is consistent with an existing design for a space-qualified helium-neon laser.[2]

As modified for the Laser/Optics Techniques Program, the Model 5600 laser features 2-milliwatt output power and leads terminated at a barrier strip for connection to the power supply located remotely at the main control console.

To ensure the feasibility of transceiver operation at 10.6 microns with the optical system employed in the laser telescope, breadboard experiments were carried out as described in Appendix B. A typical flowing-gas, water-cooled CO_2 laser was set up and used for this purpose. Sealed-off CO_2 lasers are not as yet sufficiently well developed for incorporation directly into the equipment package without seriously compromising the performance of the associated gimballed mount. Only one manufacturer (H Nu Systems) offers a "sealed-off" CO_2 laser, and, for this laser, cooling water must nevertheless be supplied through hoses. The instrument package does, however, provide for future incorporation of a CO_2 laser for transmit channel operation at 10.6 microns. In particular, the dichroic beamsplitters were specifically designed for receive channel operation at 4880 Å and transmit channel operation at either or both 6328 Å and 10.6 microns without modification. In addition, space was allocated in the design of the equipment package for a CO_2 laser and an associated modulator. This space is occupied by dummy CO_2 laser and modulator assemblies to maintain proper gimbal balance. To set the space and weight allotments for the CO_2 laser modulator, the current state of the art was surveyed and is summarized in Appendix C.

3.4 MODULATOR SUBASSEMBLY

A liberal amount of space was allocated between the helium-neon transmit laser and the first dichroic beamsplitter for a 6328 Å modulator subassembly. For the purpose of initial experiments with the equipment, the modulator subassembly shown in Figure 3-4 was added to the instrument package. This unit consists of two iris diaphragms, two objective lenses with focus adjustments, a precision pinhole plus mount, and a tuning fork chopper. The

---

[2] Perkin-Elmer Engineering Report No. 8765

FOLDOUT FRAME

FOLDOUT FRAME 2

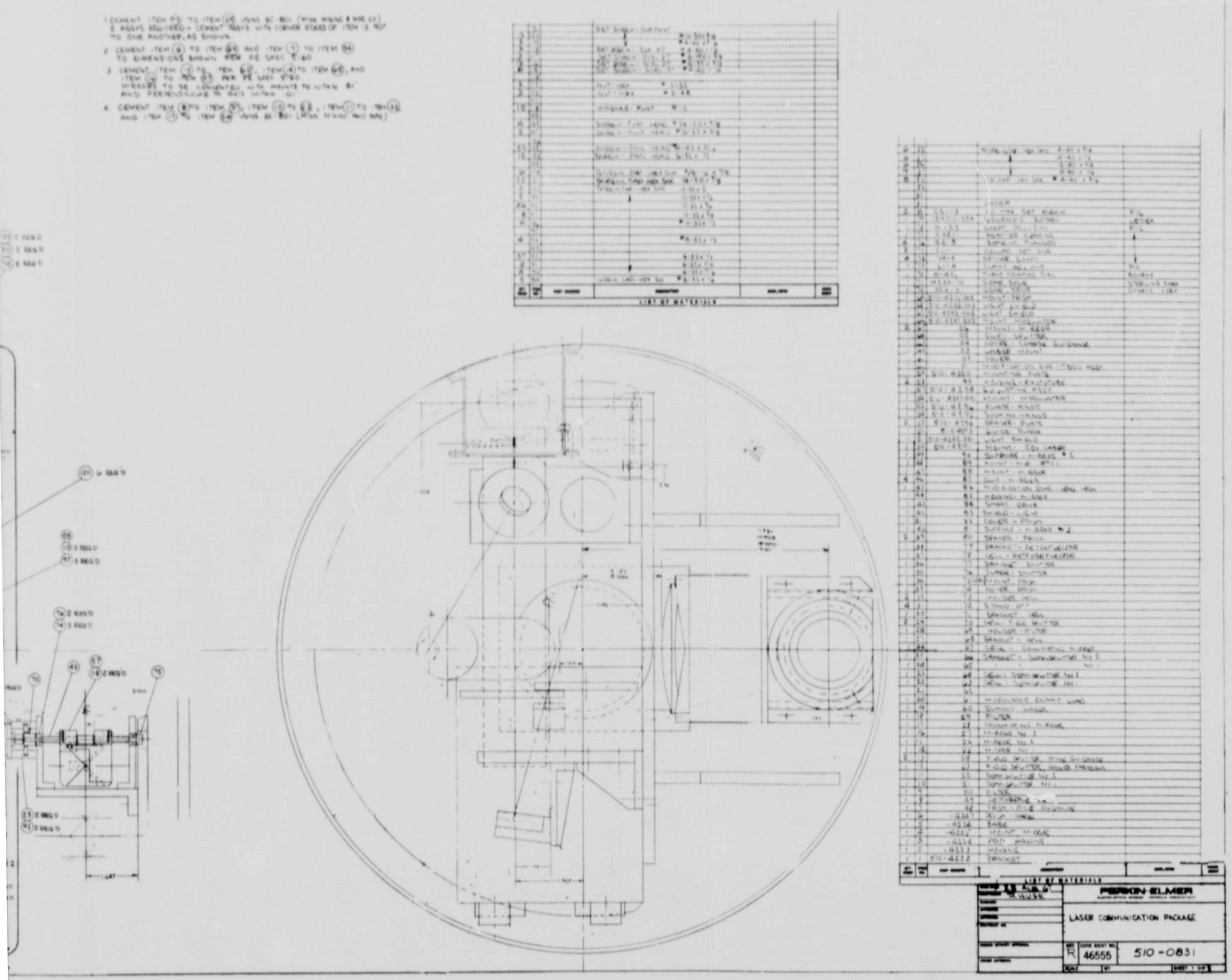

Figure 3-1. Mechanical Layout of Instrument Package - Plan and End Views

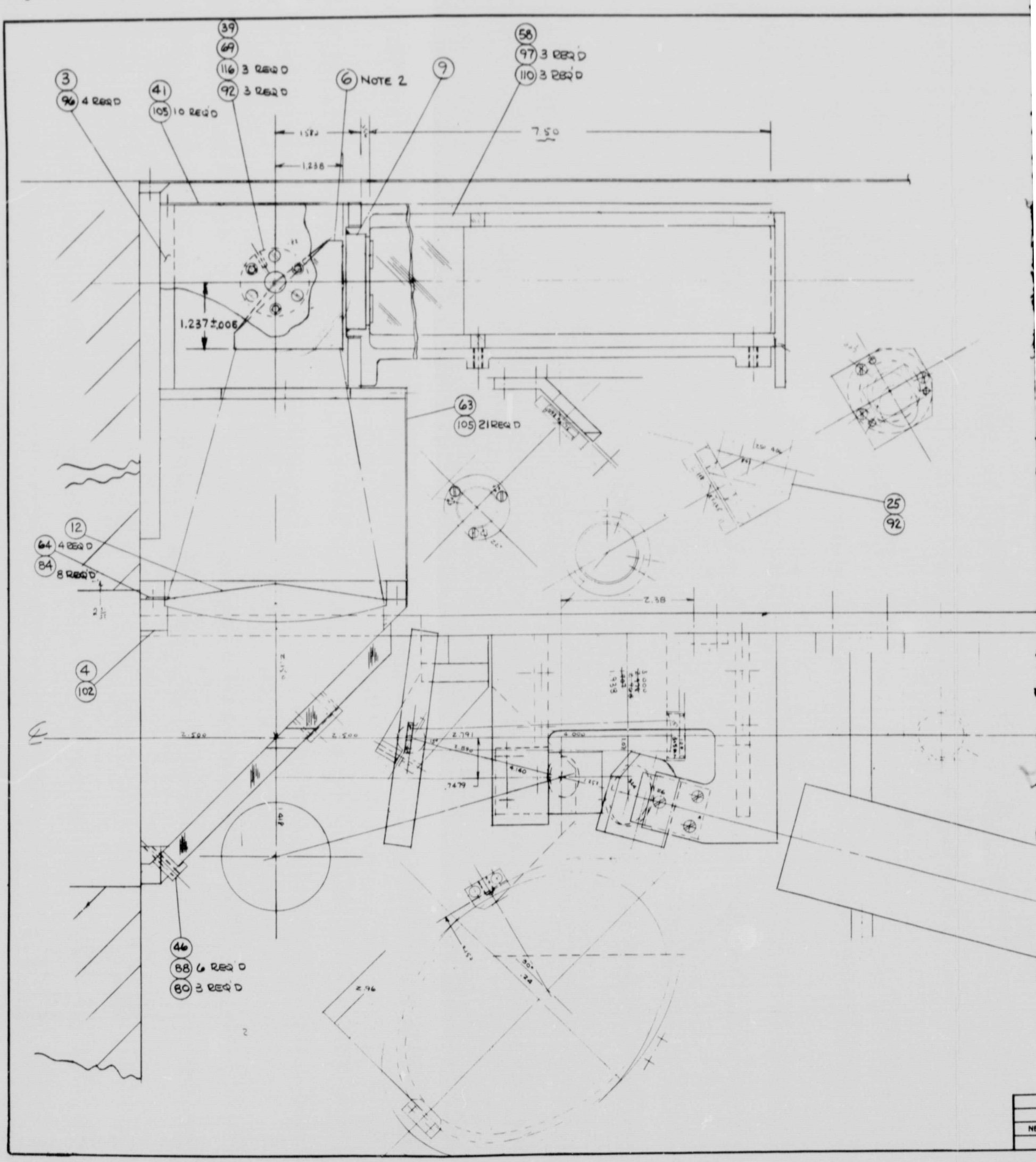

3-4 Figure 3-2. Mechanical Layout of Instrument Package - Top View

FOLDOUT FRAME 2

REVISIONS				
ZONE	LTR	DESCRIPTION	DATE	APPROVED

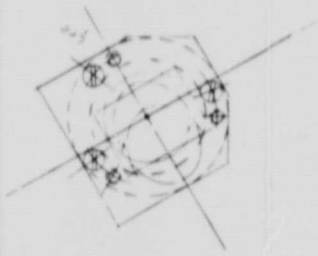

25
92

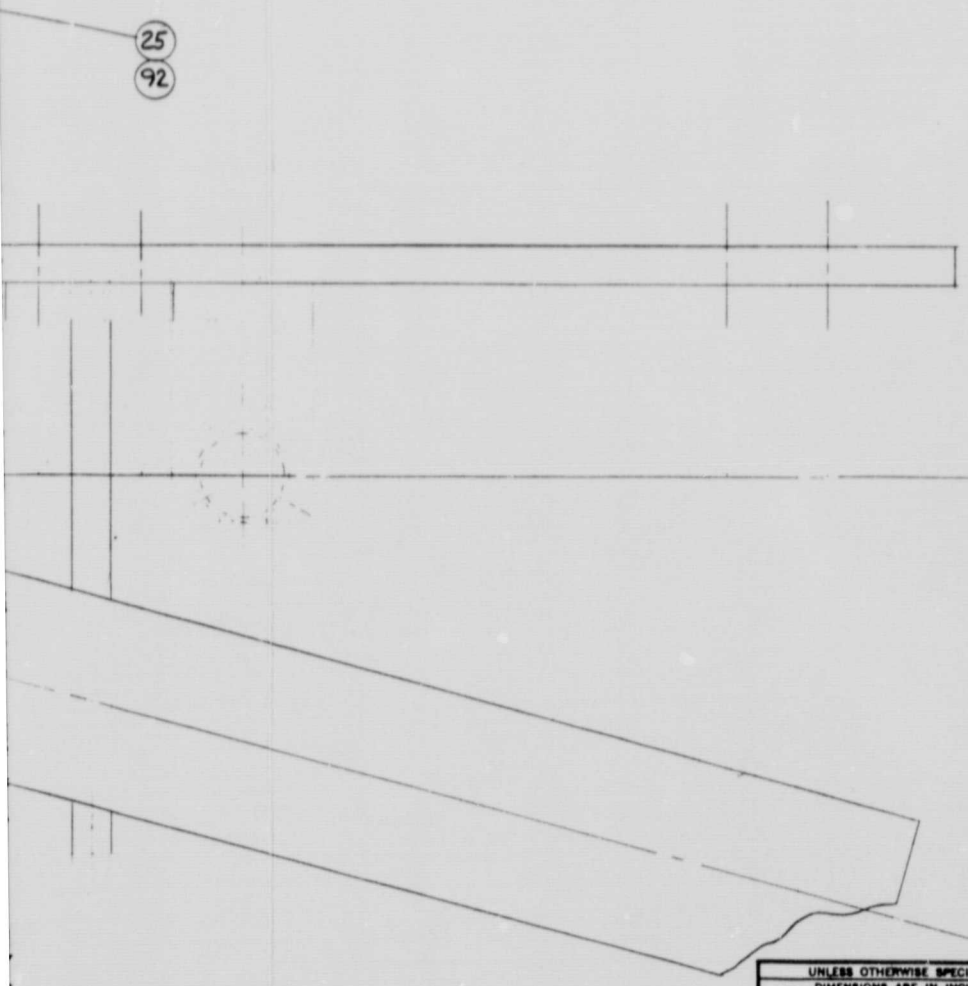

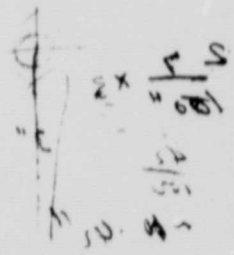

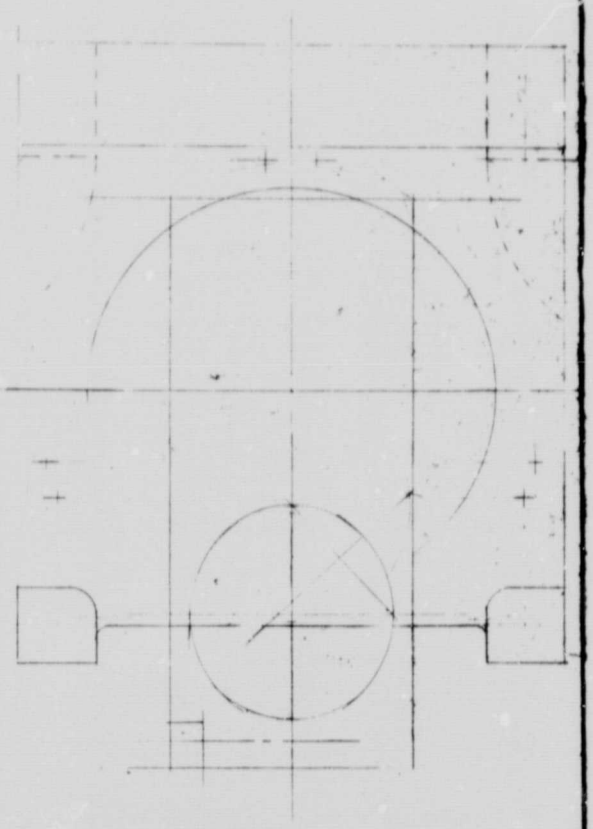

UNLESS OTHERWISE SPECIFIED
DIMENSIONS ARE IN INCHES
FRACTIONS ± DECIMALS .XX ± .XXX ± ANGLES ±
MACH COR—.005 TO .015 R OR CHAM
SH MATL—BREAK EDGES .005 MAX R
ALL √ SURFACES TO BE — √ AA
DIM AND TOL APPLY BEFORE FIN. TREAT.
MATERIAL —
FINISH —

ORIG DATE	28 AUG 67
DRAFTSMAN	RHUSE
CHECKER	
APPROVED	mlh.
APPROVED	
CONTRACT NO.	SPO 27 683
DESIGN ACTIVITY APPROVAL	
OTHER APPROVAL	

NEXT ASSY	QTY	USED ON	QTY
APPLICATION			

PERKIN-ELMER
ELECTRO-OPTICAL DIVISION NORWALK, CONNECTICUT

LASER COMMUNICATION PACKAGE

SIZE	COD[illegible]ENT NO.	
D	46[illegible]55	510-0831
SCALE [illegible]		SHEET 2 [illegible]

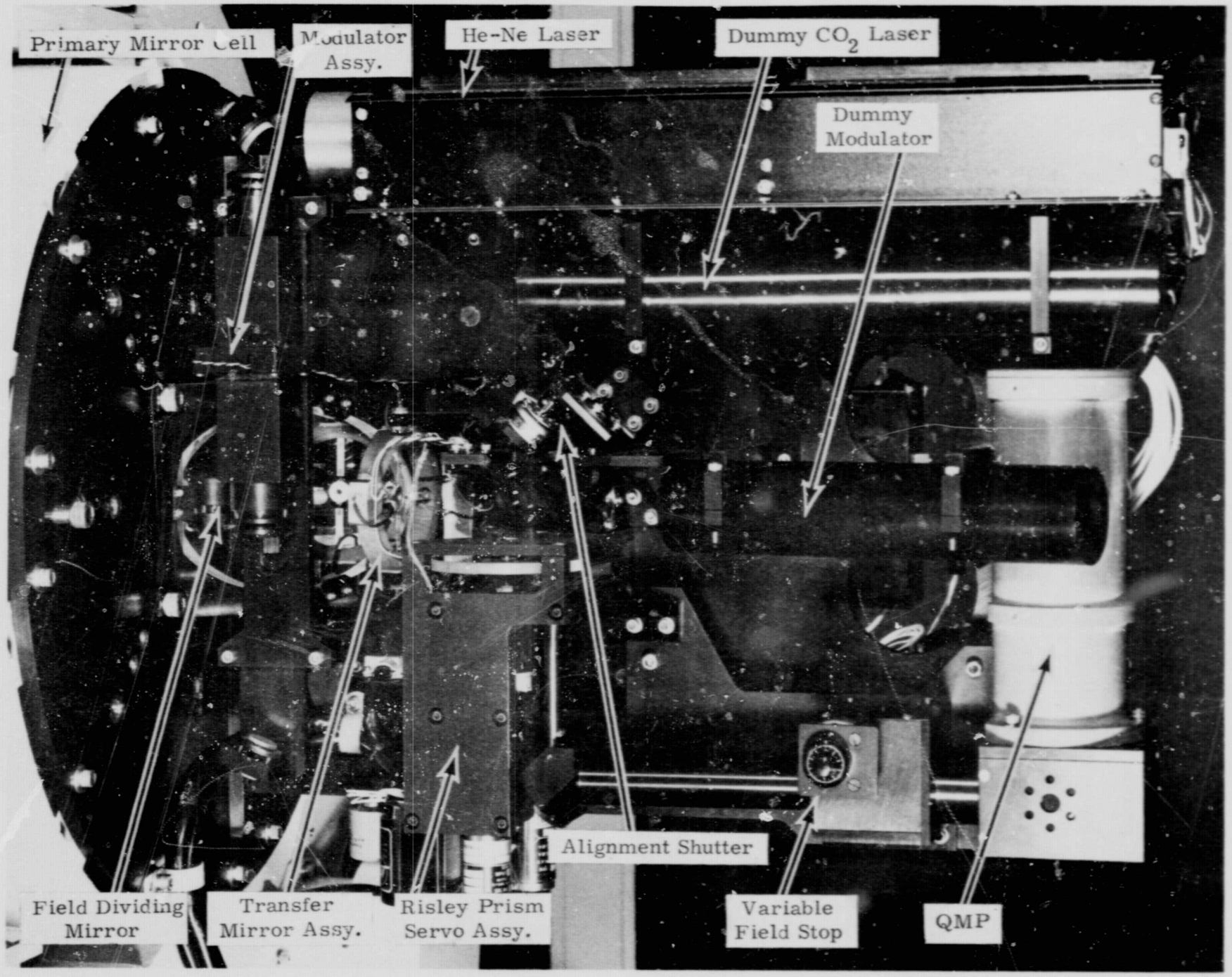

Figure 3-3. Instrument Package, Front View (Transceiver Equipment)

irises, lenses, and pinhole are used to match the diameter of the laser beam to the working aperture of the transceiver optics. The chopper is used to put a 1600-Hz signature on the transmit beam for boresighting functions and to assist in measurements of beam-pointing precision.

3.5 TRANSFER MIRROR MECHANISM

The perforated transfer mirror described previously is attached by thin metal hinges to two pairs of piezoelectric bender elements situated across two perpendicular diameters of a gimbal ring. The elements are Clevite PZT-4 Bender Bimorphs of 0.025-inch thickness poled for the so-called parallel Bimorph connection.[3,4] An earlier version of the transfer mirror assembly used PZT-5 material which was found to have on the order of 15 percent hysteresis. When this material was replaced with PZT-4, the hysteresis was reduced to below 4 percent which, for the current application, was a sufficiently low value.

The elements are 3/16 inch wide and are cantilevered with a free length of 1.25 inches from the gimbal ring. The hinges that attach the elements to the transfer mirror offer a negligibly small restraint. The spring constant is set essentially by the moment of inertia of the transfer mirror and by the spring constant of a pair of piezoelectric elements. The first mechanical resonance occurs at a frequency of 105 Hz for both axes of the present assembly. Hence, the response to an electrical input is essentially flat from D.C. to 100 Hz.

Some important characteristics of the transfer mirror mechanism are as follows:

1. The angular response of the mirror is essentially linear with voltage applied to each pair of drive elements. The range of ±25 arc-minutes requires a voltage swing of approximately 200 volts.
2. The drive elements are pure capacitances (0.015 μF each). Thus, ohmic losses are negligible.

---

[3] Perkin-Elmer Engineering Report No. 7302
[4] Unpublished Clevite Engineering Bulletin

FOLDOUT FRAME /

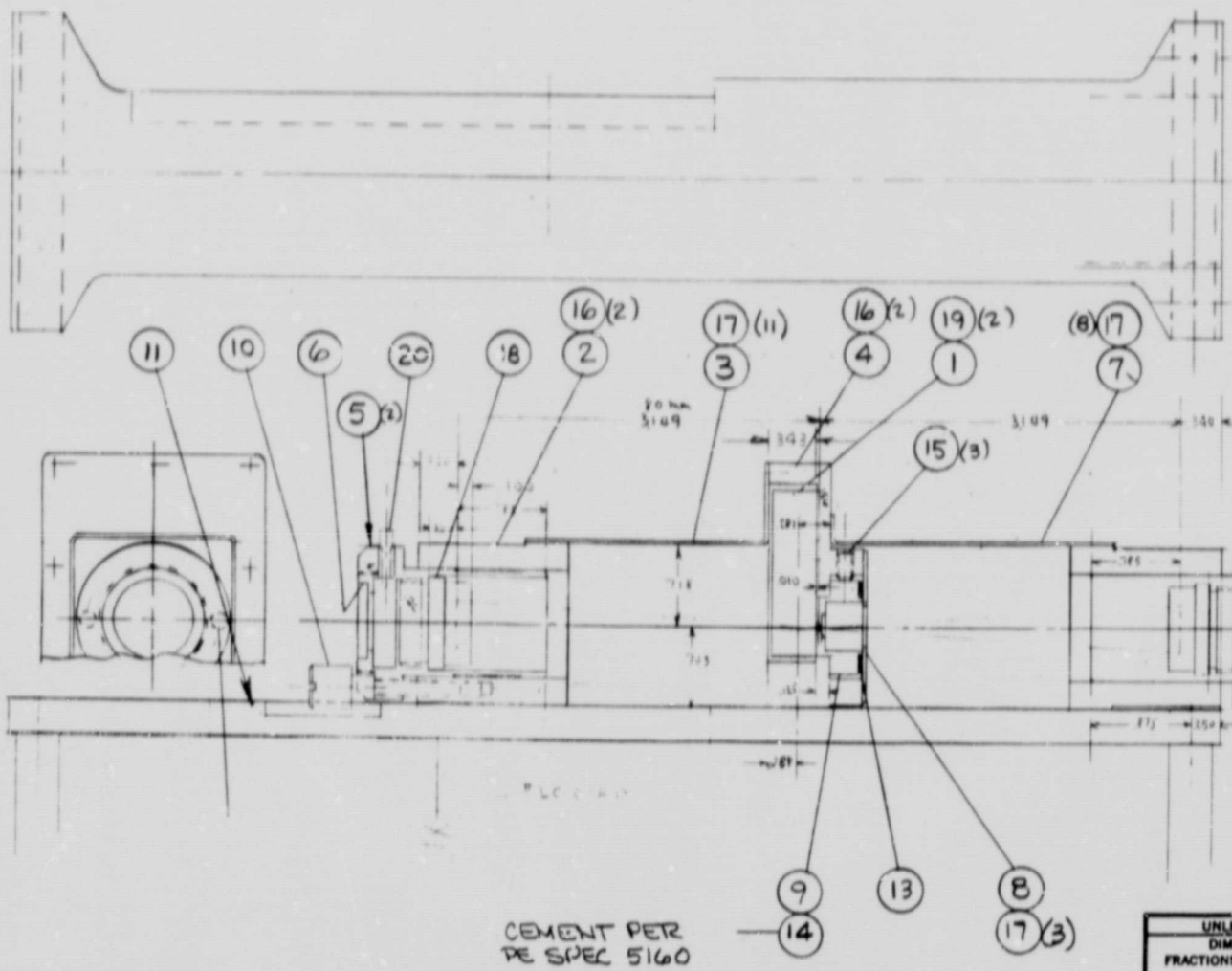

NEXT ASSY	QTY	USED ON	QTY
APPLICATION			

QUANTITY REQ

THE AS

UNLESS OTHERWISE SPECIFIED
DIMENSIONS ARE IN INCHES
FRACTIONS DECIMALS ANGL
± — ± .XX ± .XXX ±

MACH COR—.005 TO .015 R OR CHAM
SH MATL—BREAK EDGES .005 MAX R

ALL ✓ SURFACES TO BE ✓

DIM AND TOL APPLY BEFORE FIN. TREA

MATERIAL

FINISH

Fig

FOLDOUT FRAME 1

REVISIONS			
LTR	DESCRIPTION	DATE	APPROVED

AR	21	PE SPEC 5160	CEMENT	
2	20		IRIS	
2	19		SCREW, FLAT HD #2-56 x 1/2	
1	18		80 mm EFL OBJECTIVE FOR MIDIAT GAERTNER	GAERTNER
22	17		SCREW, PAN HD 4-40 UNC x 3/16	
6	16		SCREW, HEX SOC 8-32 UNC x 3/8	
3	15		SET SCREW, DUAL PT, NYLOCK #6-32	
1	14		PIN-HOLE	
1	13	R5	SPRING, WAVE WASHER	ASSOC. SP
4	12	LC-018A-13	SPRING, COMPRESSION	LEE
1	11	74	MOUNTING PLATE	
2	10	73	SCREW, ADJUSTING	
1	9	72	HOLDER, PIN HOLE	
1	8	71	PLATE, RETAINING	
1	7	70	COVER-ENTRANCE BEAM	
2	6	69	RETAINING RING, IRIS	
2	5	68	CELL, EYEPIECE	
1	4	67	HOUSING, CHOPPER	
1	3	66	COVER, EXIT BEAM	
2	2	510-4365	HOUSING, EYEPIECE	
1	1	1PER-L8C 400 CPS	CHOPPER, BEAM CANE TECH	
		011 ITEM NO.	PART OR IDENTIFYING NUMBER	NOMENCLATURE OR DESCRIPTION / CODE IDENT

QUANTITY REQUIRED

LIST OF PARTS AND MATERIALS

THE ASSEMBLY PART NUMBER IS THE DRAWING NUMBER AND THE DASH NUMBER THAT APPLIES

UNLESS OTHERWISE SPECIFIED DIMENSIONS ARE IN INCHES
DECIMALS .XX ± .XXX ± ANGLES ±
R—.005 TO .015 R OR CHAM BREAK EDGES .005 MAX R
SURFACES TO BE √AA
APPLY BEFORE FIN. TREAT.

ORIG DATE 6 OCT 67
DRAFTSMAN R HUSE
CHECKER M S L
APPROVED [illegible] 10/6/67
APPROVED
CONTRACT NO. SPO 27633
DESIGN ACTIVITY APPROVAL
OTHER APPROVAL

PERKIN-ELMER
ELECTRO-OPTICAL DIVISION NORWALK, CONNECTICUT

MODULATOR ASSY

SIZE C | CODE IDENT NO. 46555 | 510-0830

SCALE | WT | SHEET

Figure 3-4. Mechanical Layout of Modulator Subassembly

3. Additional complicated circuitry to indicate transfer mirror position is not required, since applied voltage relates directly to angular position.

4. The entire transfer mirror mechanism and its support structure weigh only 6 ounces.

The transfer mirror mechanism can be seen in Figure 3-3 and also in Figure 3-5 (the latter shows a close-up view of the 6328 Å beam paths in the instrument package).

3.6 FIELD STOP MECHANISM

The layout of the mechanism for the variable field stop of the fine guidance system (mentioned previously in Section II) is included in Figure 3-1 and a photograph of this mechanism is shown in Figure 3-6. As mentioned in paragraph 2.6 the vanes are guided between the crossed image splitting elements and are driven toward or away from each other by means of a precision lead screw.

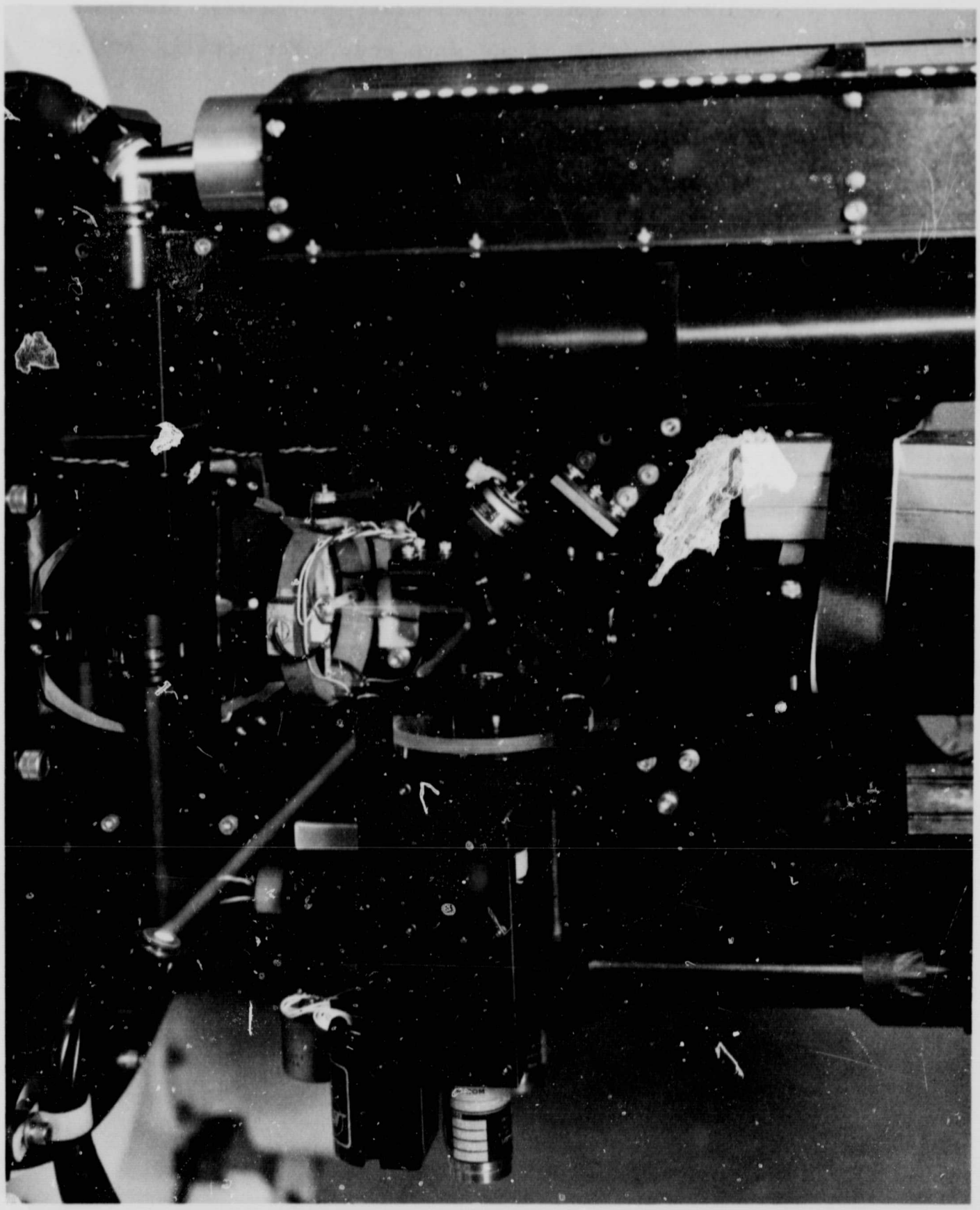

Figure 3-5. Close-up View of 3628Å Transmit Beam Paths in Transceiver Portion of Laser Telescope

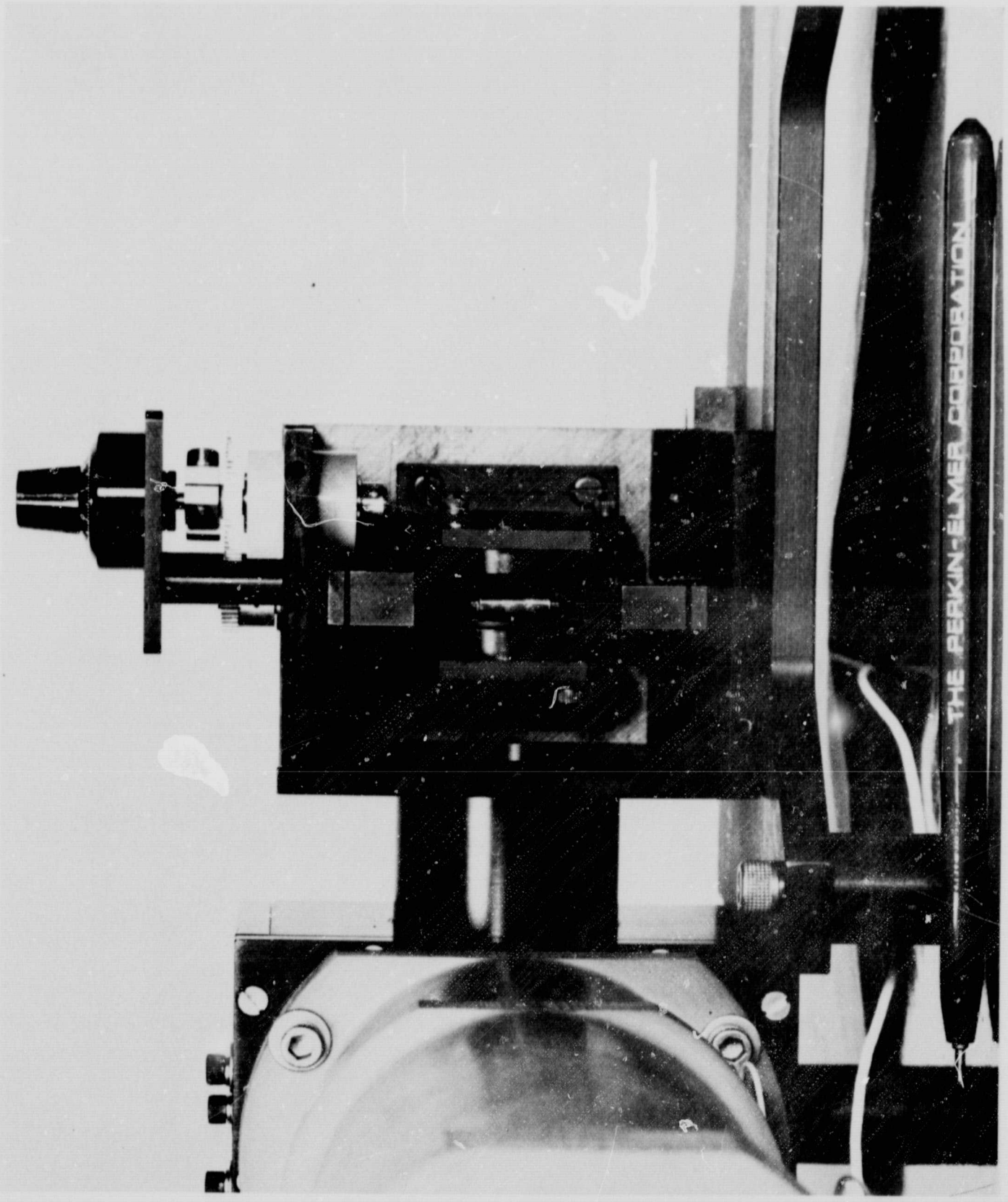

Figure 3-6. Top View of Variable Field Stop Mechanism and Image Splitters

SECTION IV

FOUR-AXIS MOUNT

4.1 INTRODUCTION

In order to test the laser telescope under conditions that realistically and effectively simulate operation in space, it was necessary to develop a multiple-axis mount that had two major functions, namely:

1. To support the laser telescope by a pair of nearly frictionless gimbals.
2. To support the gimballed laser telescope by one or more additional axes to simulate spacecraft motion.

The first function represents the means by which the laser telescope would be attached to a spacecraft having its own rather coarse attitude reference system. The second represents a means by which mechanical motion of the spacecraft can be simulated in the laboratory to test the effectiveness of the gimbals together with the coarse-acquisition and fine-guidance system of the laser telescope.

4.2 MOUNT CONFIGURATION

The configuration of the multiple-axis mount was established as depicted in Figure 4-1. The laser telescope is held by two gimbals (yaw and pitch axes) having flexure pivots and brushless torquers and synchros. The outer gimbal (pitch axis) is constructed as a yoke that is supported by rollers riding on tracks on a large cradle. This provides for roll motion with reference to the axis of the laser telescope when the gimbals are centered. The roll-motion cradle, in turn, is part of an azimuth axis turntable assembly. This turntable functions as an additional yaw axis to simulate spacecraft motion about a second axis in addition to roll. In total then the multiple-axis mount operates in four axes, the azimuth axis being an addition to the original concept of a three-axis mount.

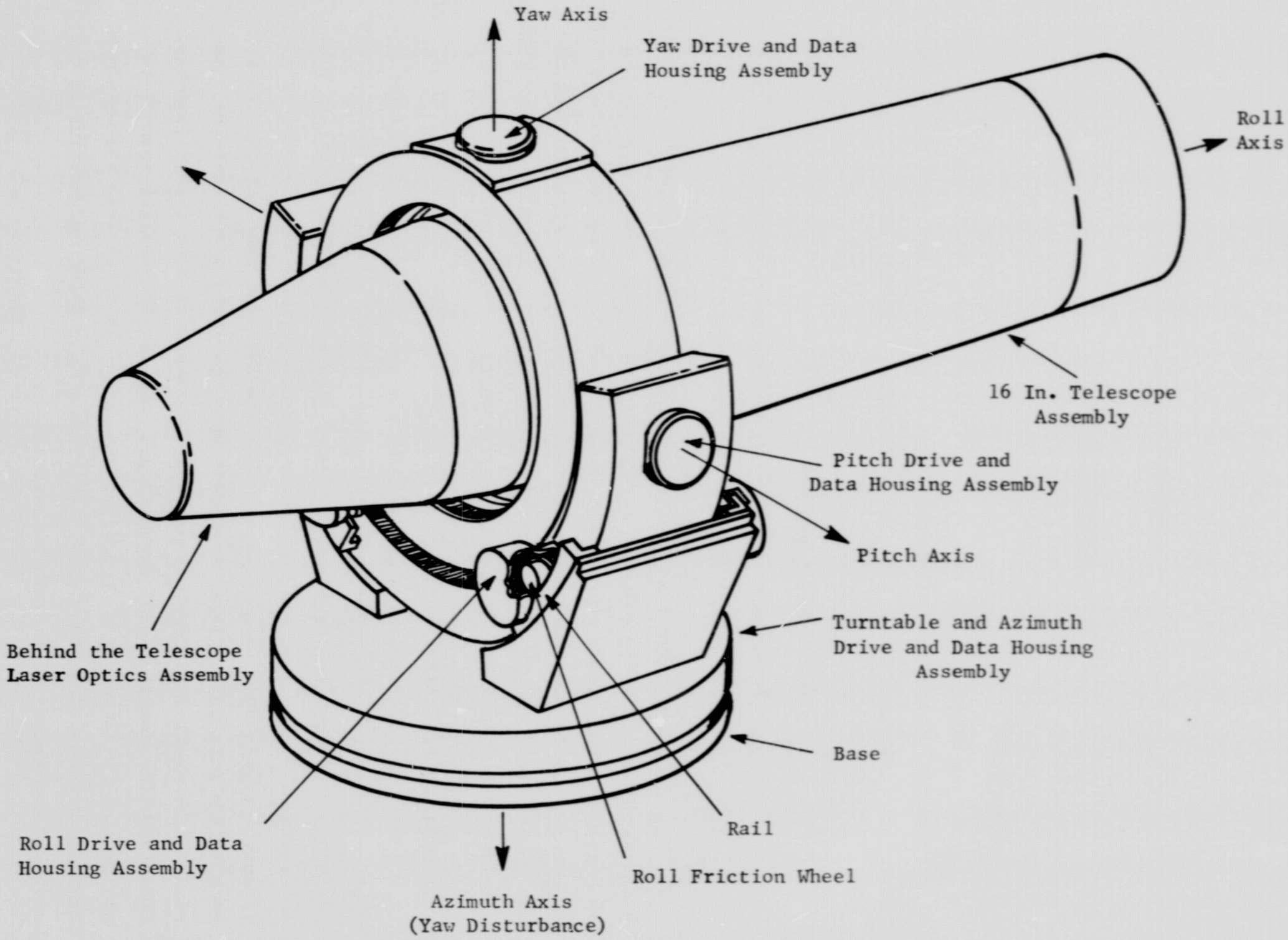

Figure 4-1. Four-Axis Laser Telescope Mount

Servo-drive, data devices, and mechanical parameters of the four-axis laser telescope mount are as follows:

A. Yaw Assembly - Includes the telescope (16-inch) and "behind-the-mirror" equipment package. This is the innermost axis.

1. Servo motors: Direct drive DC torquers, Inland, size T-3203, modified to be brushless. Two motors per axis.
2. Data Pickoff: Single-speed synchro 6-arc-minute accuracy, Clifton Precision, size ST-17-A-1. One per axis.
3. Maximum Angular Velocity: 0.0174 rad/sec.
4. Maximum Angular Acceleration: Limited by motors.
5. Unbalanced Load: Balanced statically. Balanced dynamically to within ±5.0 in.-lb (1-g acceleration).
6. Moment of Inertia (about the Yaw Axis): 225 in.-lb -sec^2 (±10%).
7. Locked Rotor Torsional Stiffness: >20 cycles/sec.
8. Yaw Bearings: Size 6032-800 Bendix flexure pivots.
9. Yaw Motion: ±7° which includes ±5° operating and ±2° for mechanical shock absorbers and limit switches.
10. Absolute Positional Accuracy: 10 arc-minutes.
11. Torque Due to Flexure Bearing Elasticity: 0 to ±1.3 in.-lb.
12. Weight on Yaw Axis: 290 lb (±5%).
13. Locking Pin: For zero reference and locking during transportation. Hand actuated.

B. Pitch Assembly - Includes the yaw assembly and gimbal.

1. Servo Motors: Direct drive DC torquers, Inland, size T-3203, modified to be brushless. Two motors per axis.
2. Data Pickoff: Single-speed synchro, 6-arc-minute accuracy, Clifton Precision, size ST-17-A-1. One per axis.

3. Maximum Angular Velocity: 0.0174 rad/sec.

4. Maximum Angular Acceleration: Limited by motors.

5. Unbalanced Load: Balanced statically within ±1.0 in.-lb. Unbalanced dynamically (3 lb. located 17 inches above the pitch axis and coinciding with the yaw axis).

6. Moment of Inertia (about the pitch axis): 275 in.-lb -sec^2 (±10%).

7. Locked Rotor Torsional Stiffness: >20 cycles/sec.

8. Pitch Bearings: Size 6032-600 Bendix flexure pivots. The torque due to bearing elasticity will be gravity compensated with ±1.0 in.-lb.

9. Pitch Motion: ±7° which includes ±5° operating and ±2° for mechanical shock absorbers and limit switches.

10. Absolute Positional Accuracy: 10 arc-minutes.

11. (a) Torque Due to Bearing Elasticity: 0 to ±1.0 in.-lb.
    (b) Torque Due to Unbalanced Load: 0 to ±1.0 in.-lb.

12. Weight on Pitch Axis: 385 lb. (±5%).

13. Locking Pin: For zero reference and locking during transportation. Hand actuated.

C. Roll Assembly - Includes the pitch assembly and yoke.

1. Friction Wheel Drive: Four rollers riding on tracks. Friction drive ratio 16/1. DC torquer coupled to each of two rollers-size T-4036 Inland torquer. A size TG-2123 Inland tachometer is used for rate reference and velocity damping.

2. Roll Motion: ±7° which includes ±5° operating and ±2° for mechanical shock absorbers and limit switches. Roll motion is to be nominally simple harmonic with variable amplitude 0 to ±5° and period 30 seconds minimum (at maximum amplitude).

3. Moment of Inertia (about the roll axis): 300 in.-lb-sec^2 (±10%).

4. Locked Rotor Torsional Stiffness: >20 cycles/sec.

5. (a) Torque Due to Unbalanced Load: 0 to ±125 in.-lb.
   (b) Torque Due to Friction: 70 in.-lb (±25%).
   (c) Weight on Roll Axis: 510 lb. (±5%).

6. Data Pickoff:
   (a) Single-speed synchro, Kearfott part No. 7RS941-1.
   (b) Sixteen-speed potentiometer, Spectrol part number Model 100, Servo, 10K, single section.

7. Absolute Positional Accuracy: 10 arc-minutes.

8. Locking Pins: For zero reference and locking during transportation Hand-actuated. Four pins are provided.

D. Azimuth Assembly - Includes the roll assembly and turntable.

1. Servo Motor: Direct drive DC torquer - Inland size T-7205. A size TG-2123 Inland tachometer is used for rate reference and velocity damping.

2. Azimuth Motion: ±7° which includes ±5° operating and ±2° for mechanical shock absorbers and limit switches. Azimuth motion is to be nominally simple harmonic, with variable amplitude 0 to ±5° and period 30 seconds minimum (at maximum amplitude).

3. Moment of Inertia (About the Azimuth Axis): 375 in.-lb -sec^2 (±10%).

4. Locked Rotor Torsional Stiffness: 20 cycles/sec.

5. Torque Due to Bearing Friction: 60 in.-lb (±25%).

6. Data Pickoff: Sixteen-speed potentiometer, Spectrol part No. Model 100, servo, 10K, single section.

7. Weight on Azimuth Bearing: 750 lb (±5%).

8. Locking Pin: For zero reference and locking during transportation. Hand actuated.

Some of the construction details of the four-axis mount are shown in Figures 4-2 through 4-5. The yaw gimbal and pitch yoke assemblies are both of dip-brazed construction. The roll axis rollers and tracks are hardened and ground steel. The azimuth axis turntable assembly is, for the most part, hogged out of large plates of aluminum tooling stock.

The flexure pivot assemblies for the pitch and yaw gimbals are illustrated in Figures 4-6 through 4-8. The roll-axis drive and data assemblies are illustrated in Figure 4-9. The completed azimuth-axis data assembly is shown in Figure 4-10. The azimuth axis turntable assembly, on which is mounted the cradle and hardened tracks for the roll-axis rollers, is shown in Figure 4-11. The roll-axis yoke assembly fitted to the azimuth axis turntable assembly is shown in Figure 4-12. The complete four-axis mount with the laser telescope attached was shown earlier in Figure 1-1.

FOLDOUT FRAME 1

NOTES:

1. THE DIP BRAZED ASS'Y SHALL MEET THE REQUIREMENTS OF MILITARY SPECIFICATION MIL-B-7883A. EXCEPTION PARAGRAPH 4.4.2, RADIOGRAPHIC EXAMINATION.
2. AFTER COMPLETION OF THE DIP BRAZING OPERATION, THE GIMBAL SHALL BE AIR QUENCHED AND HEAT TREATED FOR 16-20 HOURS AT 320°F OR 6-10 HOURS AT 350°F.
3. ALL DIMENSIONS APPLY AFTER HEAT TREATMENT PER NOTE 2. AND A 72°F ±5°F AMBIENT TEMPERATURE.

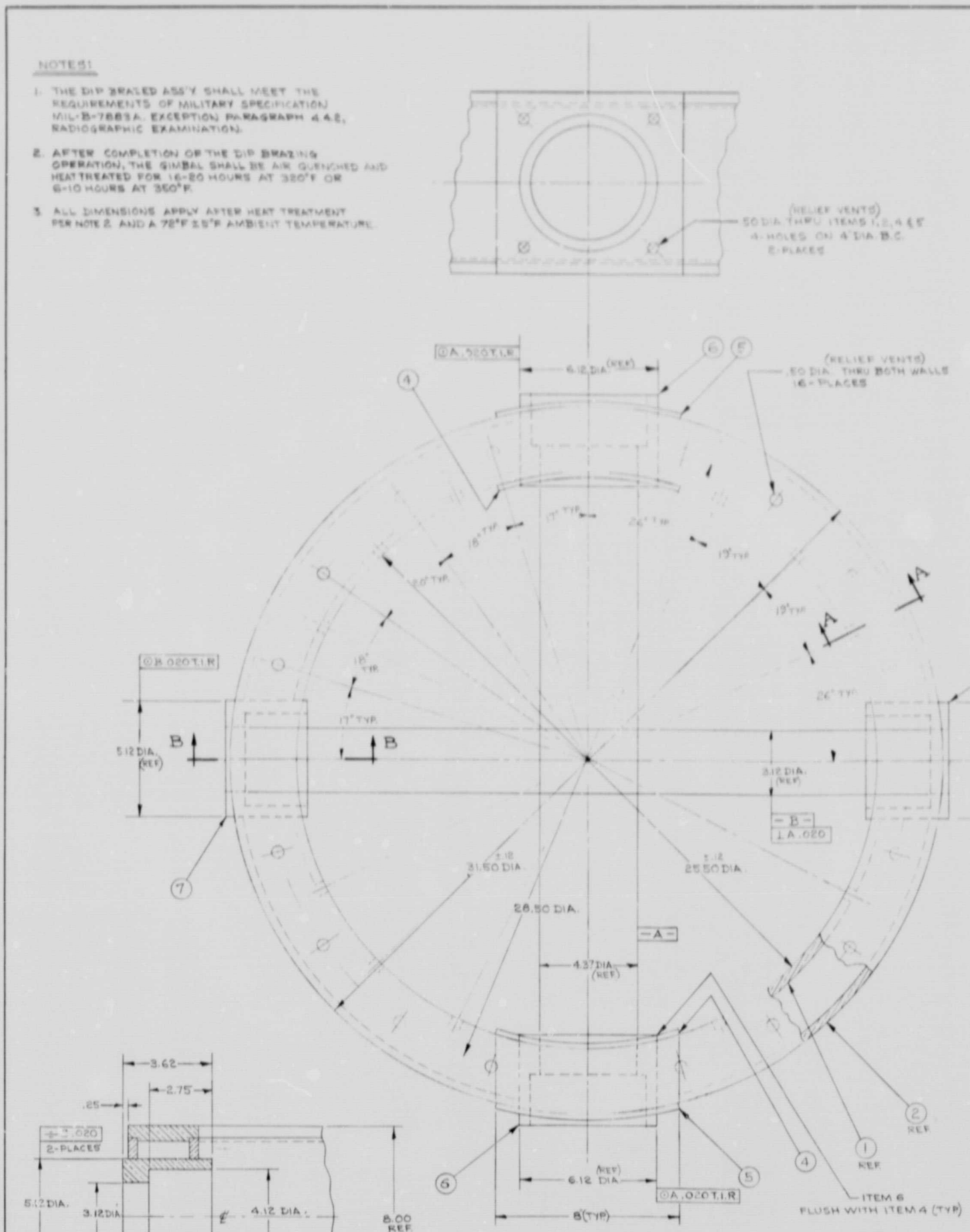

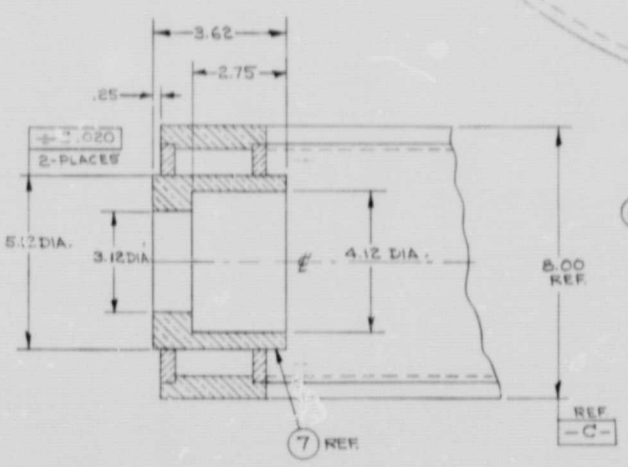

SECTION "B-B"

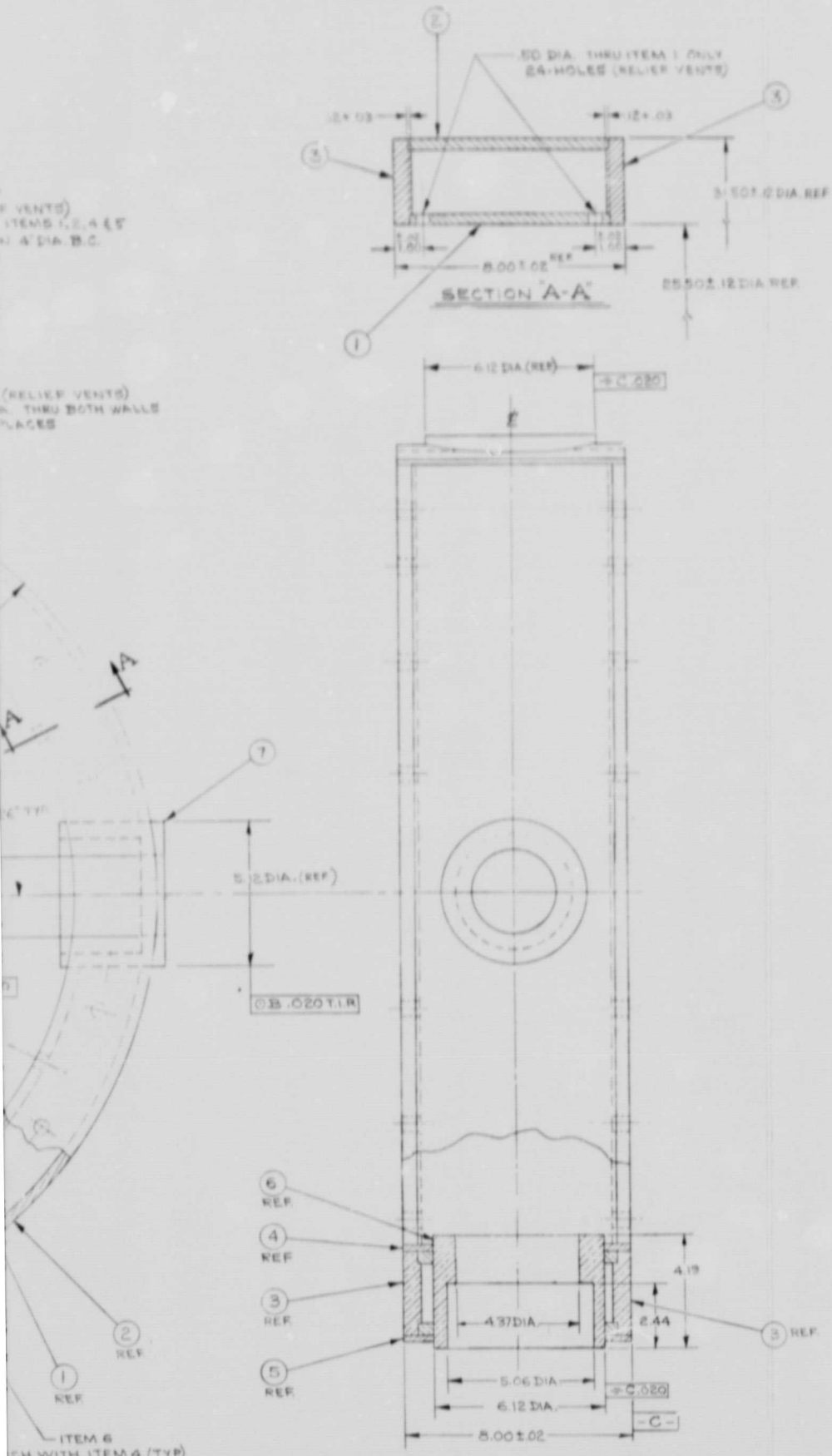

QTY REQD	ITEM NO.	PART NUMBER	DESCRIPTION	MATL/SPEC	CODE IDENT
2	7		HOUSING, PIVOT, PITCH	6061-T6	
2	6		HOUSING, PIVOT, YAW	6061-T6	
2	5		STIFFENER, OUTER	6061-T651 (.250 THK PLATE)	
2	4		STIFFENER, INNER	6061-T651 (.250 THK PLATE)	
2	3		COVER PLATE	6061-T651 (.625 THK PLATE)	
1	2		RING, OUTER	6061-T651 (.375 THK PLATE)	
1	1		RING, INNER	6061-T651 (.375 THK PLATE)	

LIST OF MATERIALS

UNLESS OTHERWISE SPECIFIED DIMENSIONS ARE IN INCHES. FRACTIONS ± 1/16, DECIMALS .XX ± .01, .XXX ± .005, ANGLES ± 2°	DRG DATE 5-19-67	PERKIN-ELMER ELECTRO-OPTICAL DIVISION NORWALK CONNECTICUT	
BREAK EDGES TO .025 R OR CHAMFER BY MATL—BREAK EDGES FOR MACH'G	DRAFTSMAN [illegible]	GIMBAL, YAW (DIP BRAZED ASS'Y.)	
ALL ✓ SURFACES TO BE ✓ 64	CHECKER		
DIM AND TOL APPLY BEFORE PAINT, TREAT	APPROVED [illegible]		
MATERIAL ALUM. AL. SEE MAT'L. SPEC.	APPROVED		
FINISH	CONTRACT NO.		
	DESIGN ACTIVITY APPROVAL	SIZE E; CODE IDENT NO. 46555; CX510-0767	
	OTHER APPROVAL	SCALE 1:2; WT; SHEET	

NEXT ASSY	QTY	USED ON	QTY
APPLICATION			

Figure 4-2. Yaw Gimbal Assembly

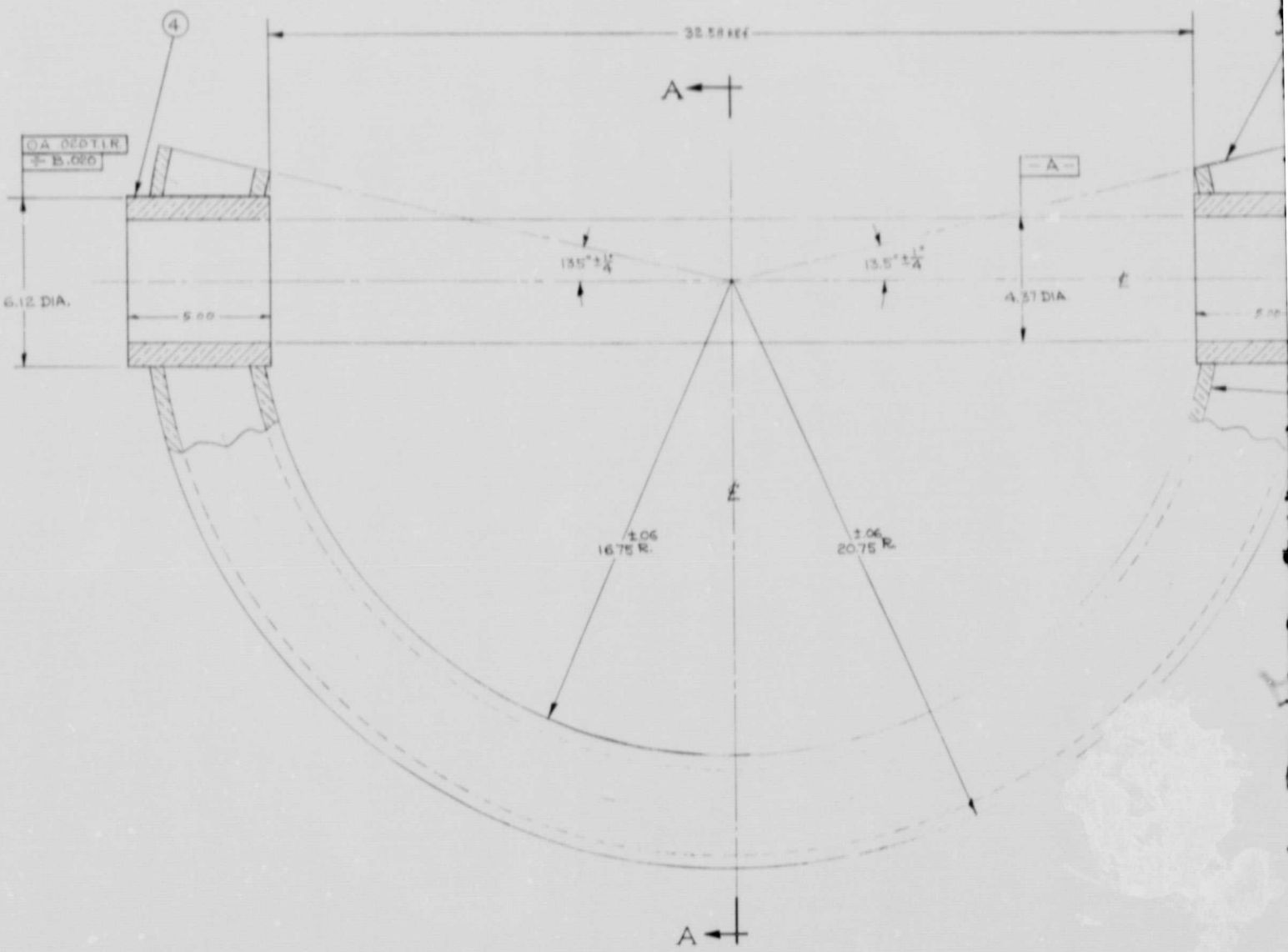

3. ALL DIMENSIONS APPLY AFTER HEAT TREATMENT PER NOTE 2 AND A 72°F ±5°F AMBIENT TEMPERATURE.

2. AFTER COMPLETION OF THE DIP BRAZING OPERATION, THE YOKE SHALL BE AIR QUENCHED AND HEAT TREATED FOR 16-20 HOURS AT 320°F OR 6-10 HOURS AT 350°F.

1. THE DIP BRAZED ASSY. SHALL MEET THE REQUIREMENTS OF MILITARY SPECIFICATION MIL-B-7883A. EXCEPTION, PARAGRAPH 4.4.2, RADIOGRAPHIC EXAMINATION.

 Figure 4-3 Pitch Yoke Assembly

FOLDOUT FRAME 2

REVISIONS				
ZONE	LTR	DESCRIPTION	DATE	APPROVED
	A	REVISED	1-5-67	

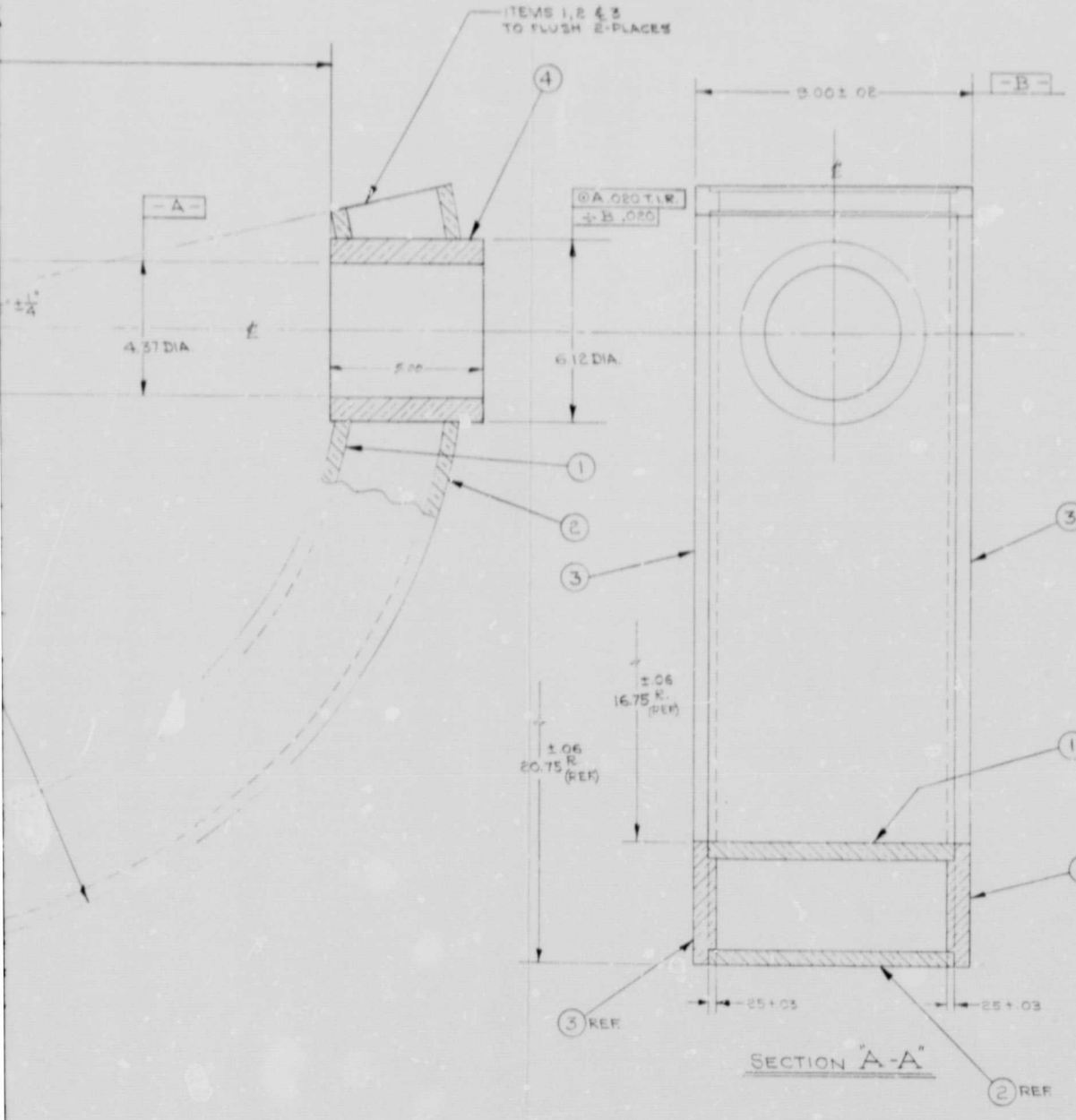

SECTION "A-A"

QTY REQD	ITEM NO.	PART NUMBER	DESCRIPTION	MATL/SPEC	CODE IDENT
2	4		HOUSING, PIVOT PITCH	6061-T6	
2	3		COVER PLATE	6061-T651 (.750 THK PLATE)	
1	2		RING, OUTER	6061-T651 (.500 THK PLATE)	
1	1		RING, INNER	6061-T651 (.500 THK PLATE)	

LIST OF MATERIALS

UNLESS OTHERWISE SPECIFIED
DIMENSIONS ARE IN INCHES
FRACTIONS ± 1/64 | DECIMALS XX ± .01, XXX ± .005 | ANGLES ±
MACH COR—.005 TO .015 R OR CHAM
SH MATL—BREAK EDGES .063 MAX R
ALL √ SURFACES TO BE √ 64
DIM AND TOL APPLY BEF. PLTG. OR A. TREAT.
MATERIAL ALUM. ALL
SEE MATL. SPEC
FINISH

ORIG DATE 5-25-67
DRAFTSMAN
CHECKED
APPROVED
APPROVED
CONTRACT NO.
DESIGN ACTIVITY APPROVAL
OTHER APPROVAL

PERKIN ELMER
OPTICAL DIVISION NORWALK CONNECTICUT

YOKE, PITCH
(DIP BRAZED ASS'Y)

SIZE E | CODE IDENT NO. 46555 | CX510-0768
SCALE 1:2 | WT | SHEET

NEXT ASSY	QTY	USED ON	QTY
APPLICATION			

FOLDOUT FRAME 1

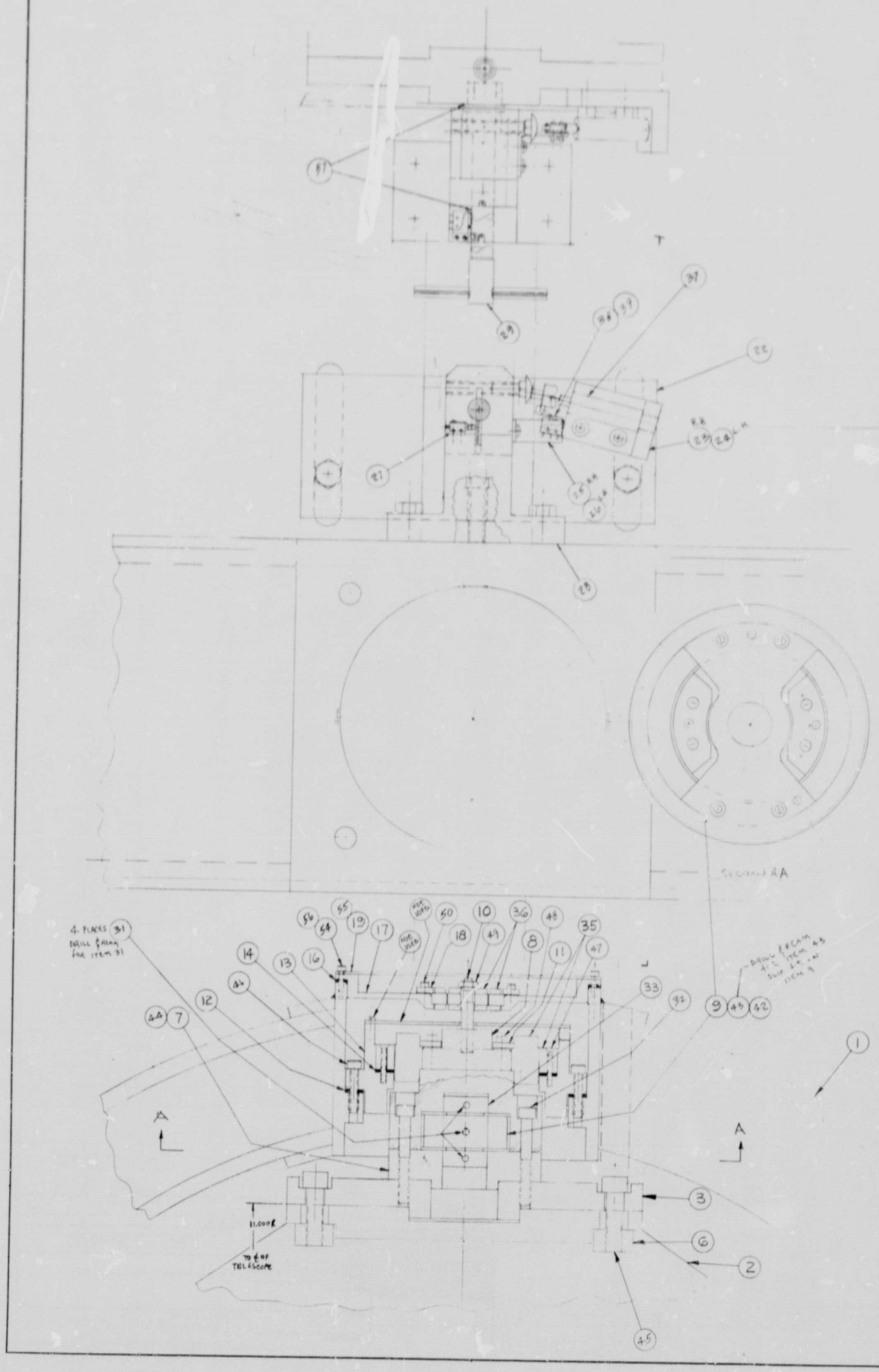

FOLD-OUT FRAME 2

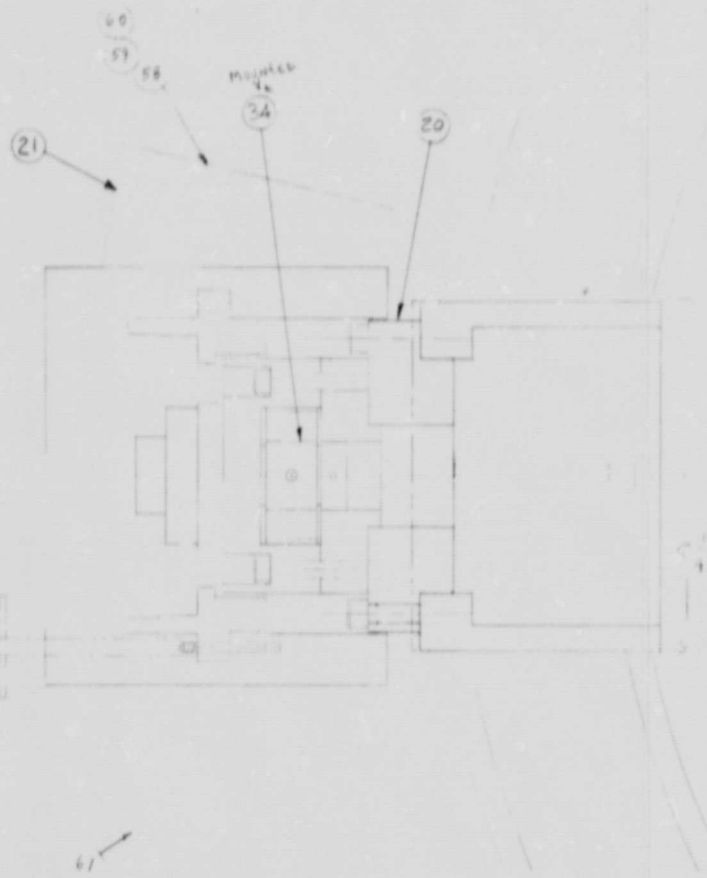

REVISIONS				
ZONE	LTR	DESCRIPTION	DATE	APPROVED

QTY REQD	ITEM NO.	PART NUMBER	DESCRIPTION	MATL/SPEC	CODE IDENT
2	61	SKAF 6207	BALLRET, SHIELD		
1	60	SKAF 9167-2	PLATE, COVER		
1	59	SKAF 9167-1	PLATE, COVER		
1	58	X510-4017-2	BRACKET - "ZERO ALIGNMENT"		
4	57		BUSHING, CORE LOCK CLR = .11000		
8	56		SCREW SOCKET HD CAP 8-32 X .50 LG (18-8 STAINLESS)		
2	55	SKAF 6767	COVER		
1	54		SCREW SOCKET HD CAP 0-80 X .50 LG (18-8 STAINLESS)		
4	53		WASHER #8 .375 OD .032 THK (18-8 STAINLESS)		
4	52		SCREW SOCKET HD CAP 1/4-28 X .75 LG (18-8 STAINLESS)		
2	51		SCREW HEX HD CAP 3/8-24 X 1.50 LG (18-8 STAINLESS)		
8	50		SCREW SOCKET HD CAP 8-32 X .375 LG (18-8 STAINLESS)		
2	49		NUT, 10-32 HEX (18-8 STAINLESS)		
16	48		SCREW SOCKET HD CAP 0-80 X .375 LG (18-8 STAINLESS)		
16	47		SCREW 82° FLAT HEAD 4-40 X .750 LG (18-8 STAINLESS)		
32	46		SCREW SOCKET HD CAP 10-32 X 1.000 LG (18-8 STAINLESS)		
4	45		SCREW SOCKET HD CAP 5/16-24 X 1.375 LG (416 STAINLESS)		
8	44		SCREW SOCKET HD CAP 6-32 X .375 LG (18-8 STAINLESS)		
2	43		DOWEL PIN, .1875 - .1879 DIA X 1.000 LG (416 STAINLESS)		
24	42		SCREW SOCKET HD CAP 10-32 X 1.125 LG (18-8 STAINLESS)		
2	41	X510-4005-2	SHAFT, MOTOR STATOR		
2	40	X510-4007-2	RING, STATOR MOUNTING		
6	39	42-51	AUXILIARY ACTUATOR MICRO-SWITCH		
6	38	15X1-T	SPDT MICRO SWITCH		
4	37	SA 8.4	SHOCK ABSORBER, INTEGRATED DYNAMICS		
2	36	ST-17-A-1	CONTROL TRANSFORMER - CPPC		
4	35	T-5203	INLAND TORQUE MOTOR		
2	34	6052-600	BENDIX FREE-FLEX PIVOT		
2	33	6052-800	BENDIX FREE-FLEX PIVOT		
12	32		BOLT, 1/4-28 X .750 LG SOCKET HD (18-8 STAINLESS)		
12	31		DOWEL PIN, .1251-.1254 DIA X .375 LG (416 SS)		
1	30	SKAF 6667	ADAPTER, SHOCK		
1	29	X510-4018	JIG PIN - MODIFICATION		
1	28	X510-4017	BRACKET - "ZERO ALIGNMENT"		
1	27	X510-4014	MOUNTING PLATE - STOP SWITCH		
1	26	X510-4013	BRACKET - LIMIT SWITCH, LEFT HAND		
1	25	X510-4012	BRACKET - LIMIT SWITCH, RIGHT HAND		
1	24	X510-4011	BRACKET - STOP, LEFT HAND		
1	23	X510-4010	BRACKET - STOP, RIGHT HAND		
1	22	X510-4005	HOUSING - JACK SCREW		
X	21		YOKE - PITCH, MACHINED	SEE X510-0768 BRACE ASSY	
2	20	X510-4021	TRANSITION PIECE		
2	19	X510-3998	DUST COVER		
2	18	X510-4002	RETAINER - SYNCHRO STATOR		
2	17	X510-4005	RING - SYNCHRO MTG		
2	16	X510-3996	SHIM - SYNCHRO MTG RING		
	15	X510-4008	SHIELD - MAGNETIC		
4	14	X510-3995	SHIM - STATOR, MOTOR		
2	13	X510-4007-1	RING - STATOR MOUNTING		
4	12	X510-4022	SHIM - PIVOT SPACING		
4	11	X510-3999	RETAINER - MOTOR ROTOR		
2	10	X510-3997	SHAFT - SYNCHRO		
4	9	X510-4006	WEB, GIMBAL - PIVOT		
2	8	X510-4008-1	SHAFT - MOTOR ROTOR		
4	7	X510-4000	CAP - BEARING		
4	6	X510-4001	PLATE - NUT		
1	5	X510-4020	ADAPTER - TELESCOPE TO SLIDE PLATE		
1	4	X510-4019	PLATE, SLIDE, LOWER		
1	3	X510-4004	SLIDE (UPPER YAW BRG)		
X	2		SCOPE TELESCOPE ASSY		
X	1		SLIDE PLATE, MACHINED	SEE X510-0767 BRACE ASSY	

LIST OF MATERIALS

UNLESS OTHERWISE SPECIFIED DIMENSIONS ARE IN INCHES
FRACTIONAL ± DECIMAL ± ANGULAR ±
MACH ☐ FIN ☐ ALL OVER
BREAK EDGES
ALL ✓ SURFACES TO BE ✓
DIM AND TOL APPLY BEFORE FIN TREAT
MATERIAL
FINISH
DRAWN CH
CHECKED
APPROVED
CONTRACT NO.
DESIGN ACTIVITY APPROVAL
OTHER APPROVAL

PERKIN-ELMER
ELECTRO OPTICAL DIVISION NORWALK, CONNECTICUT

PIVOT ASSYS - YAW & PITCH

SIZE E | CODE IDENT NO. 46555 | X510-0770

SCALE FULL | WT | SHEET

NEXT ASSY	QTY	USED ON	QTY
APPLICATION			

Figure 4-4. Yaw and Pitch Pivot Assemblies

FOLDOUT FRAME 1

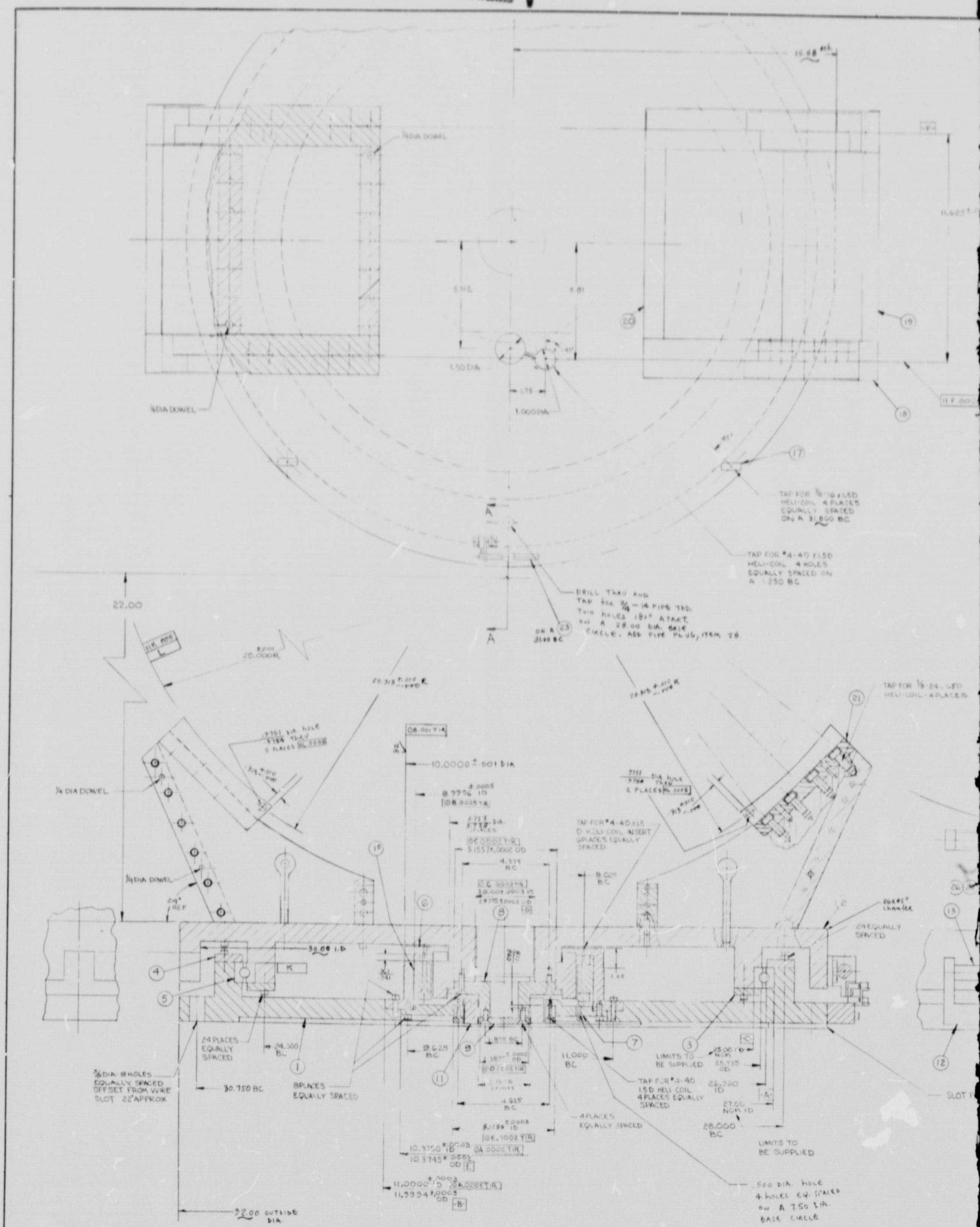

4-10 Figure 4-5. Azimuth Axis Turntable Assembly

FOLDOUT FRAME 2

REVISIONS				
ZONE	LTR	DESCRIPTION	DATE	APPROVED
	A	REVISED	5-1-67	R Fredette
	B	ADDED Ø2.00 O.D. BORE 7A ADDED Ø1.00 I.D. BORE 7B CHANGED 15.18 TO 15.65 BORE 5B CHANGED Ø1.50 BC BORE 8B TO Ø1.56 BC	6-9-67	R Fredette

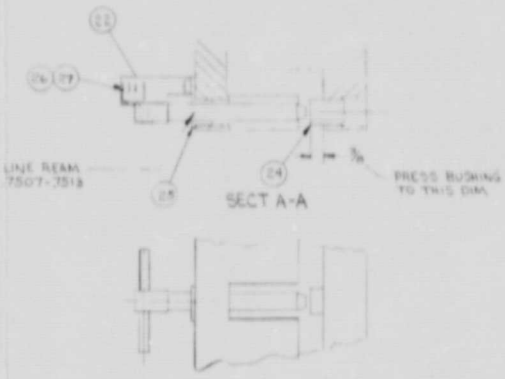

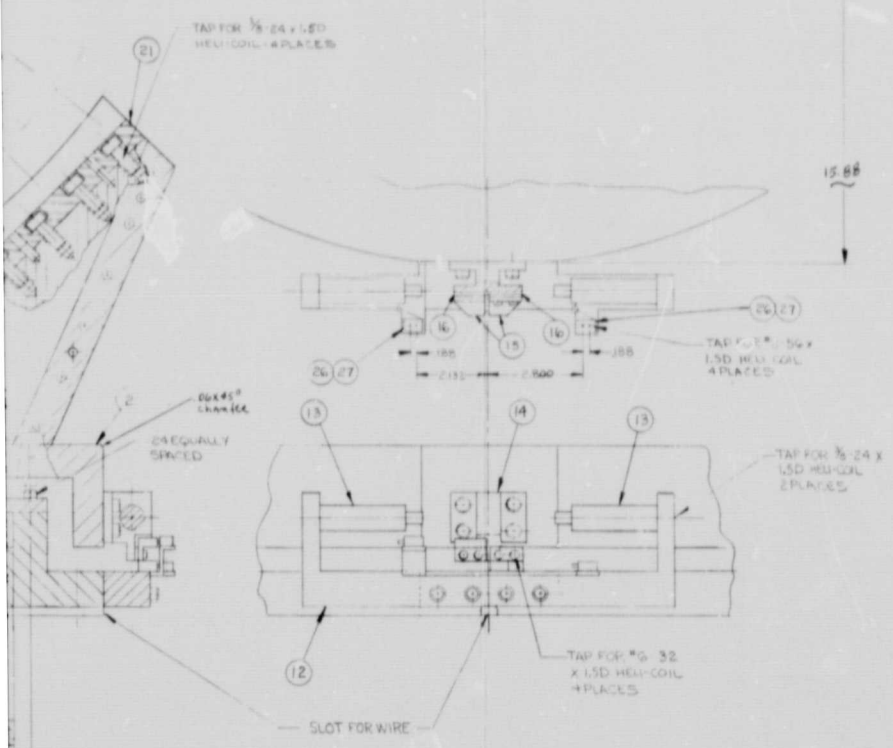

QTY REQD	ITEM NO.	PART NUMBER	DESCRIPTION	MATL/SPEC	CODE IDENT
2	28		PIPE PLUG	3/4-14 NPTF, 18-8 ST. STL.	
3	27		ACTUATOR SWITCH	W CRD-SWITCH* JX-51	
3	26		SWITCH-MICRO	MICRO-SWITCH* 1SX1-T	
1	25		BUSHING-HEADED	CARR LANE* CLB 11000	
1	24		BUSHING-PLAIN	CARR LANE* L 1/2 ID x 1 LG	
1	23		INDEX PIN	CARR LANE CL-50-UP	
1	22		BRACKET SWITCH MOUNT	ALUM 6061-T6	
4	21		RAIL	AISI 440F CRES RC55-60	
2	20		SUPPORT	ALUM TOOLING PLATE 1 THK	
2	13		SUPPORT	ALUM TOOLING PLATE 1 THK	
4	18		PLATE SIDE	ALUM TOOLING PLATE 2 THK	
4	17		EYE BOLT	CARR LANE* CL-37-EB	
2	16		SHIM-LAMINATED .10 THK	BRASS .002 THK LAMINATIONS	
2	15		CAM-SWITCH ACTUATOR	ALUM 6061-T6	
1	14		BRACKET-STOP & CAM MOUNT	ALUM 6061-T6	
4	18		SHOCK ABSORBER INTEGRATED DYNAMICS INC	SA12.8	
1	12		BRACKET SHOCK	ALUM 6061-T6	
1	11		TACH INLAND MOTOR CORP	T8401A	
1	10		TORQUE MOTOR INLAND MOTOR CORP	T7205	
1	9		RETAINER TACH	ALUM 6061-T6	
1	8		JOURNAL-TACH	ALUM 6061-T6	
1	7		ADAPTER-TACH MOUNT	ALUM TOOLING PLATE 3/4 THK	
1	6		ADAPTER-MOTOR MOUNTING	ALUM 6061-T6	
1	5		BRG	KAYDON* KG050XP	
1	4		RING BRG RETAINING-OUTER	ALUM TOOLING PLATE 3/8 THK	
1	3		RING BRG RETAINING-INNER	ALUM TOOLING PLATE 3/8 THK	
1	2		TURN TABLE	ALUM TOOLING PLATE 3 THK	
1	1		BASE PLATE	ALUM TOOLING PLATE 3 THK	

LIST OF MATERIALS

TAP FOR #6-32 x 1.5D HELI-COIL 4 PLACES

#4-40 x 1.5D HELI-COIL 4 HOLES EQUALLY SPACED ON 50 BC

DIA. HOLE
HOLES EQUALLY SPACED
A 7.50 DIA.
SE CIRCLE

4. EXACT BEARING BORE & O.D. DIMENSIONS WILL BE SUPPLIED BY ENG.
3. BEARING SHAFT & HOUSING DIA'S TO BE ⊥ TO SHAFT AND HOUSING SHOULDERS WITHIN .0005.
2. SCALE ALL UNSPECIFIED DIMS.
1. UNLESS OTHERWISE SPEC: TAP ALL TAPPED HOLES FOR 1/4-28 x 1.5D HELI-COIL, DIA'S ON A COMMON AXIS CONC .010 TIR
NOTES

NEXT ASSY	QTY	USED ON	QTY

APPLICATION

UNLESS OTHERWISE SPECIFIED DIMENSIONS ARE IN INCHES	
FRACTIONS ± 1/64	DECIMALS XX ± .01 XXX ± .005
ANGLES ± 2°	
MACH COR—.005 TO .015 R OR CHAM	
SH MATL—BREAK EDGES .005 MAX R	
ALL ✓ SURFACES TO BE 125 AA	
DIM. AND TOL. APPLY BEFORE FIN. TREAT.	
MATERIAL	
FINISH	

ORIG DATE	5-25-67
DRAFTSMAN	J. O'Connor
CHECKER	
APPROVED	R. Fredette
APPROVED	
CONTRACT NO.	
DESIGN ACTIVITY APPROVAL	
OTHER APPROVAL	

PERKIN-ELMER
ELECTRO-OPTICAL DIVISION NORWALK, CONNECTICUT

LAYOUT-TURNTABLE ASSY

SIZE	CODE IDENT NO.	
E	46555	CX510-10111

SCALE 1/2 WT SHEET

FORM NO. 7067

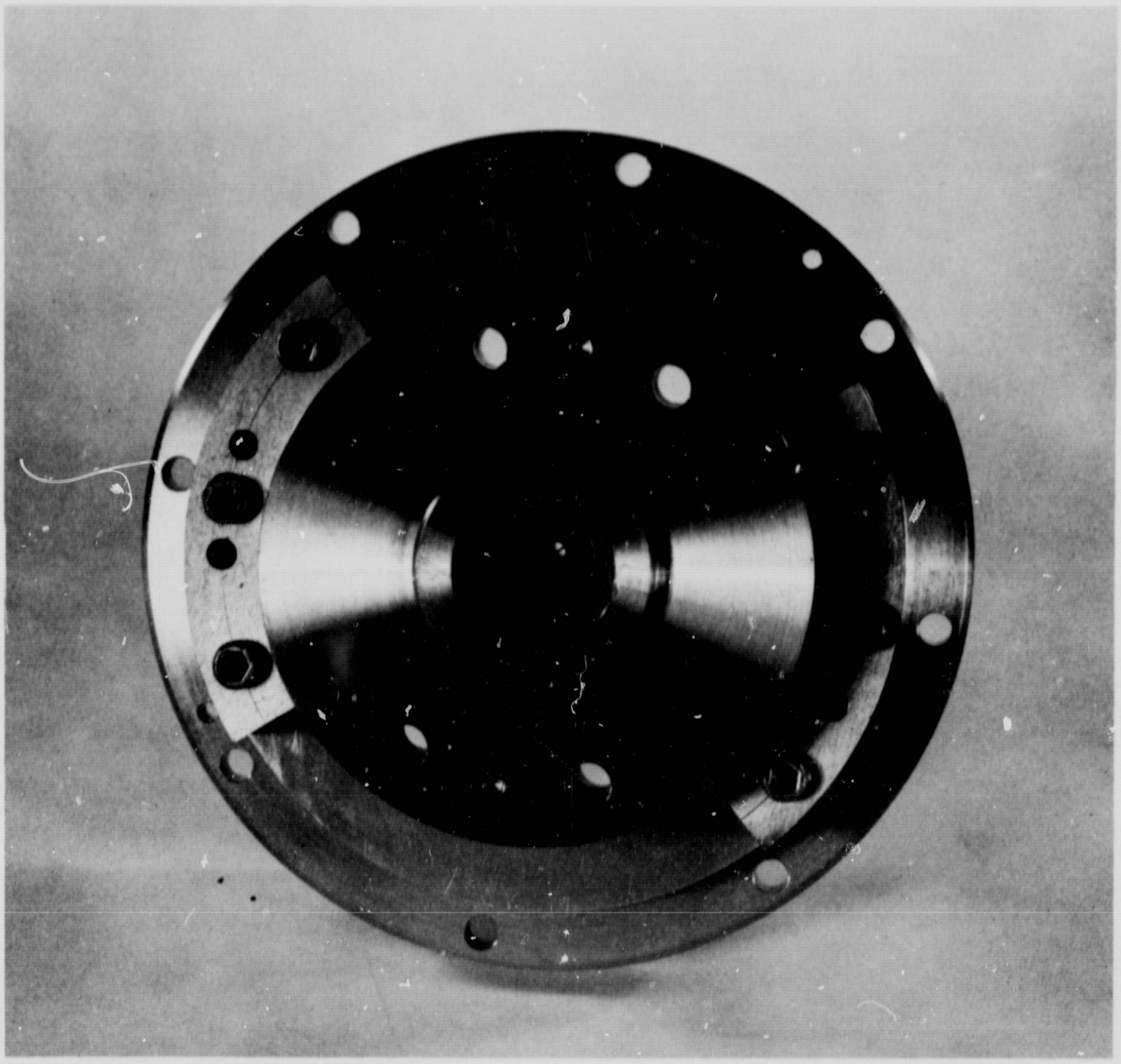

Figure 4-6. Full Scale View of Yaw Axis Pivot Assembly Showing Flexure Bearing

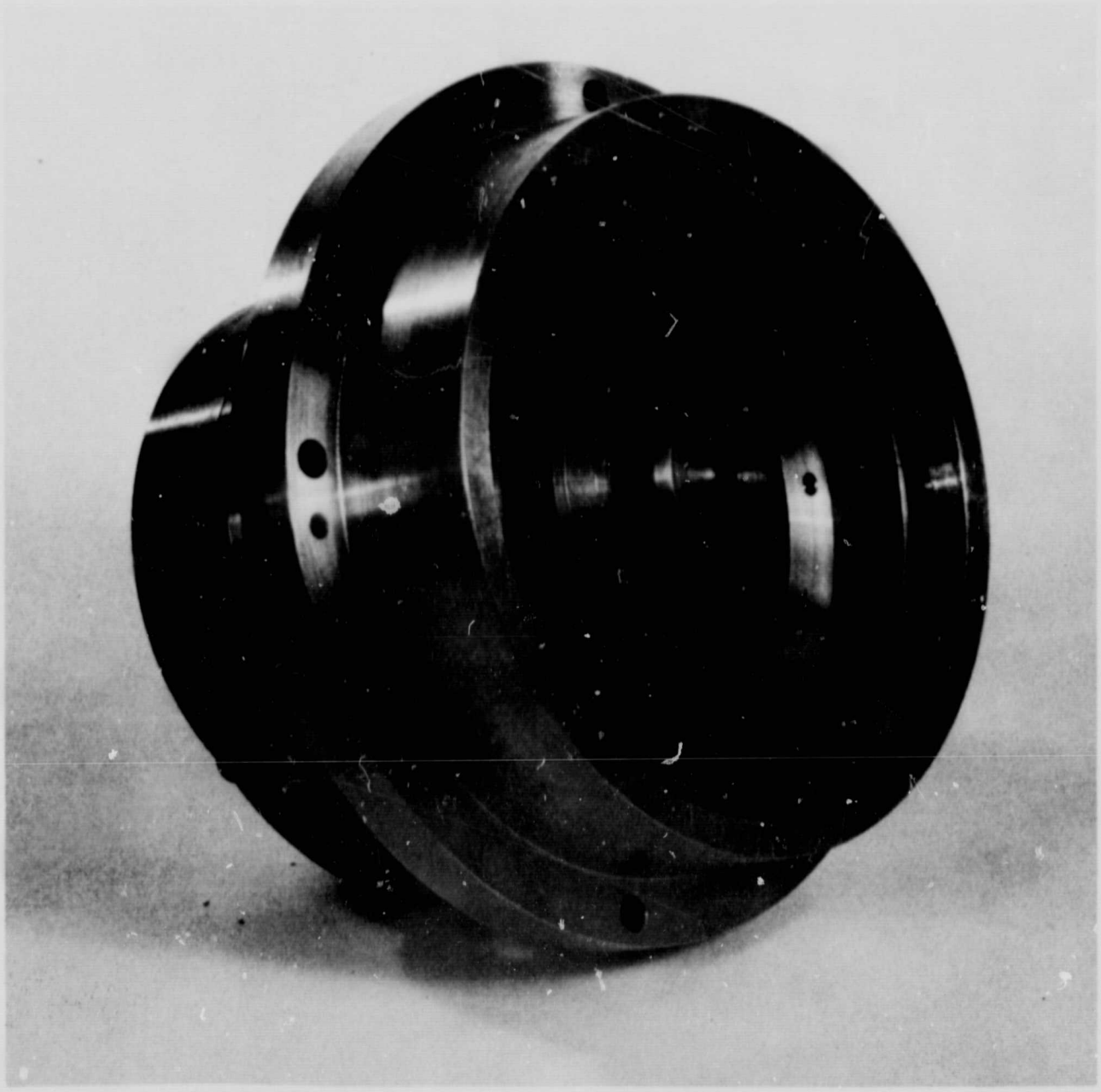

Figure 4-7. Rear View of Yaw Axis Pivot Assembly.

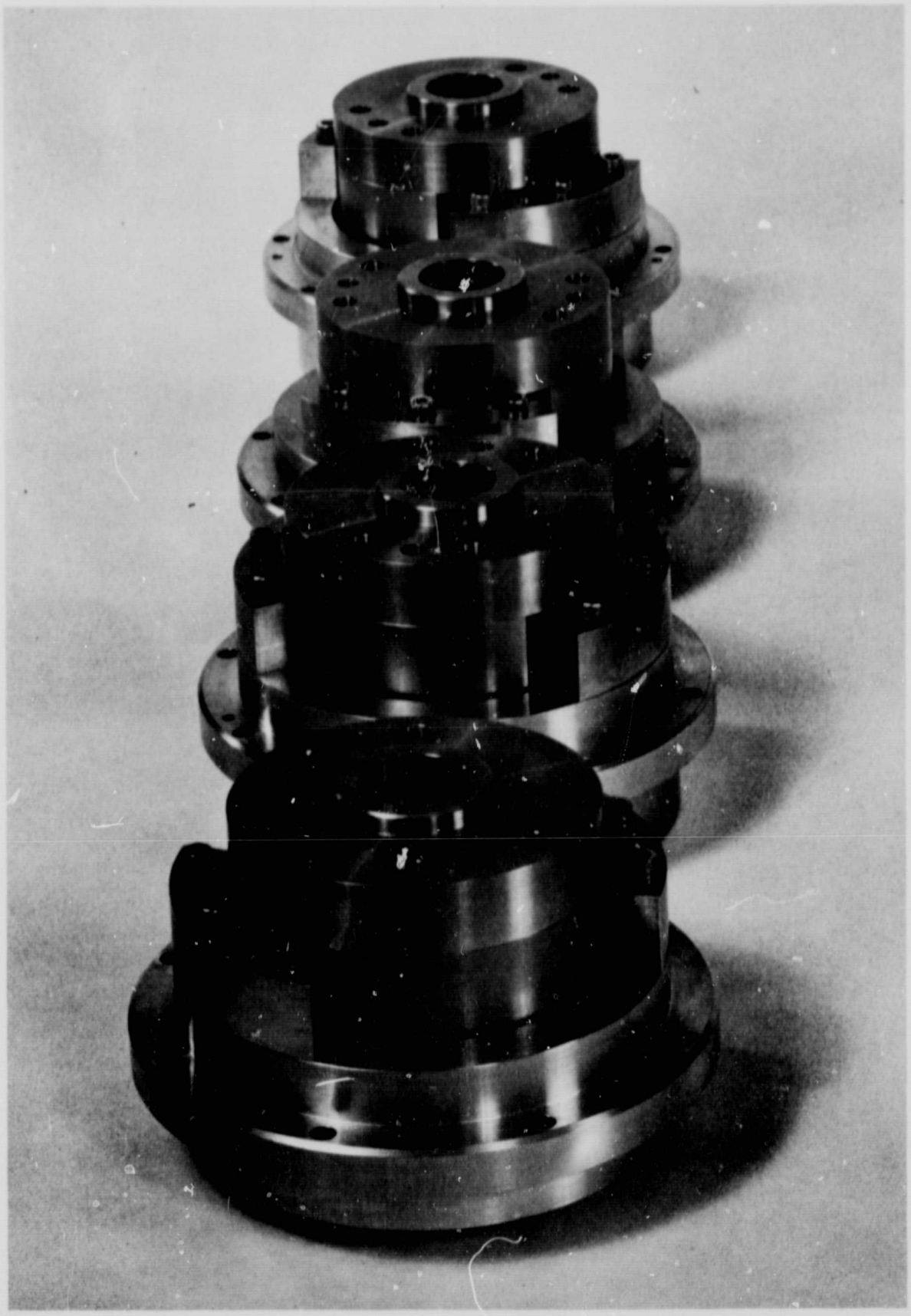

Figure 4-8. Flexure Pivot Assemblies for Pitch and Yaw Axes

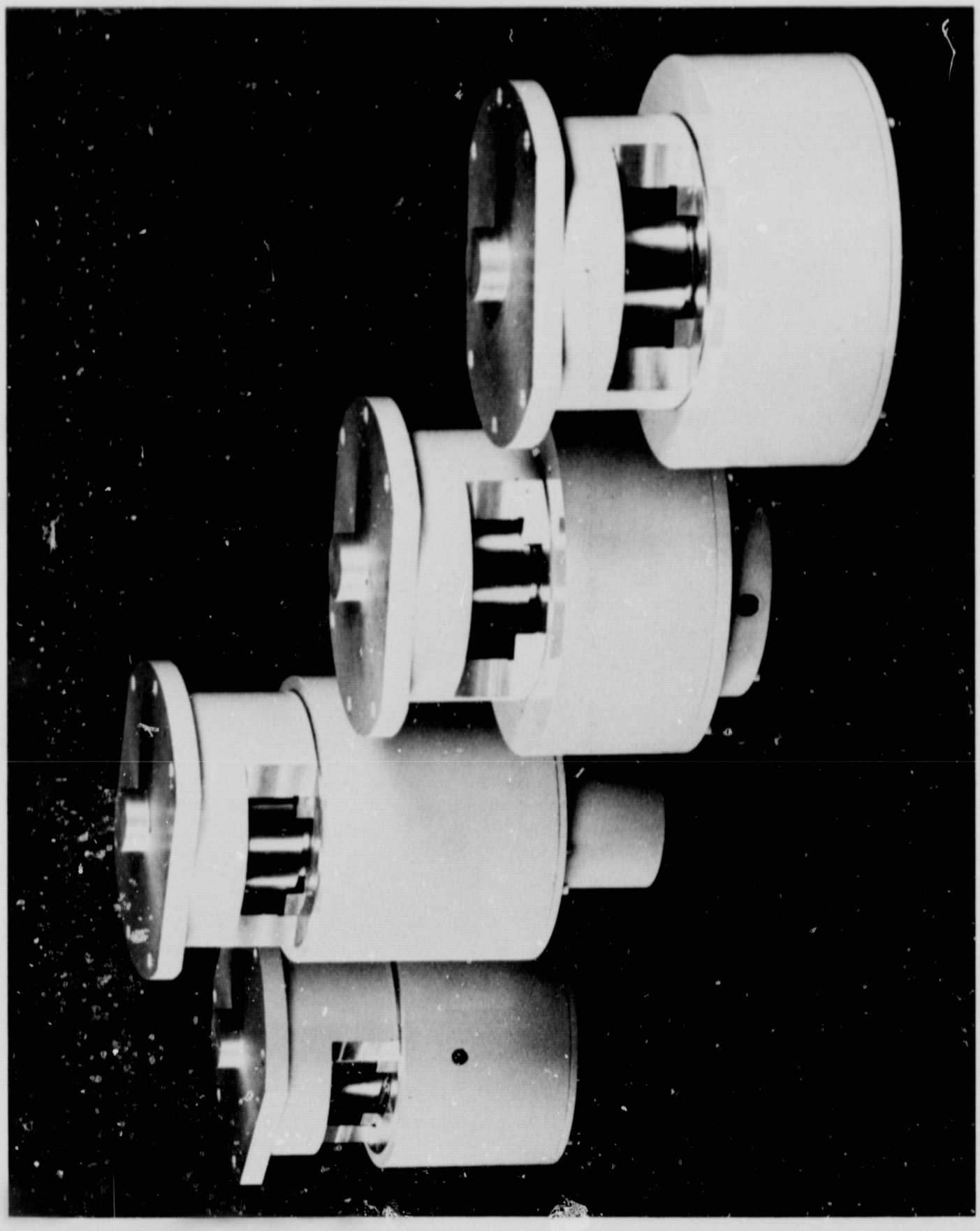

Figure 4-9. Roll-Axis Drive and Data Assemblies. The View Shows How the Housings are Cut Away Where the Rollers Ride on the Roll-Axis Tracks.

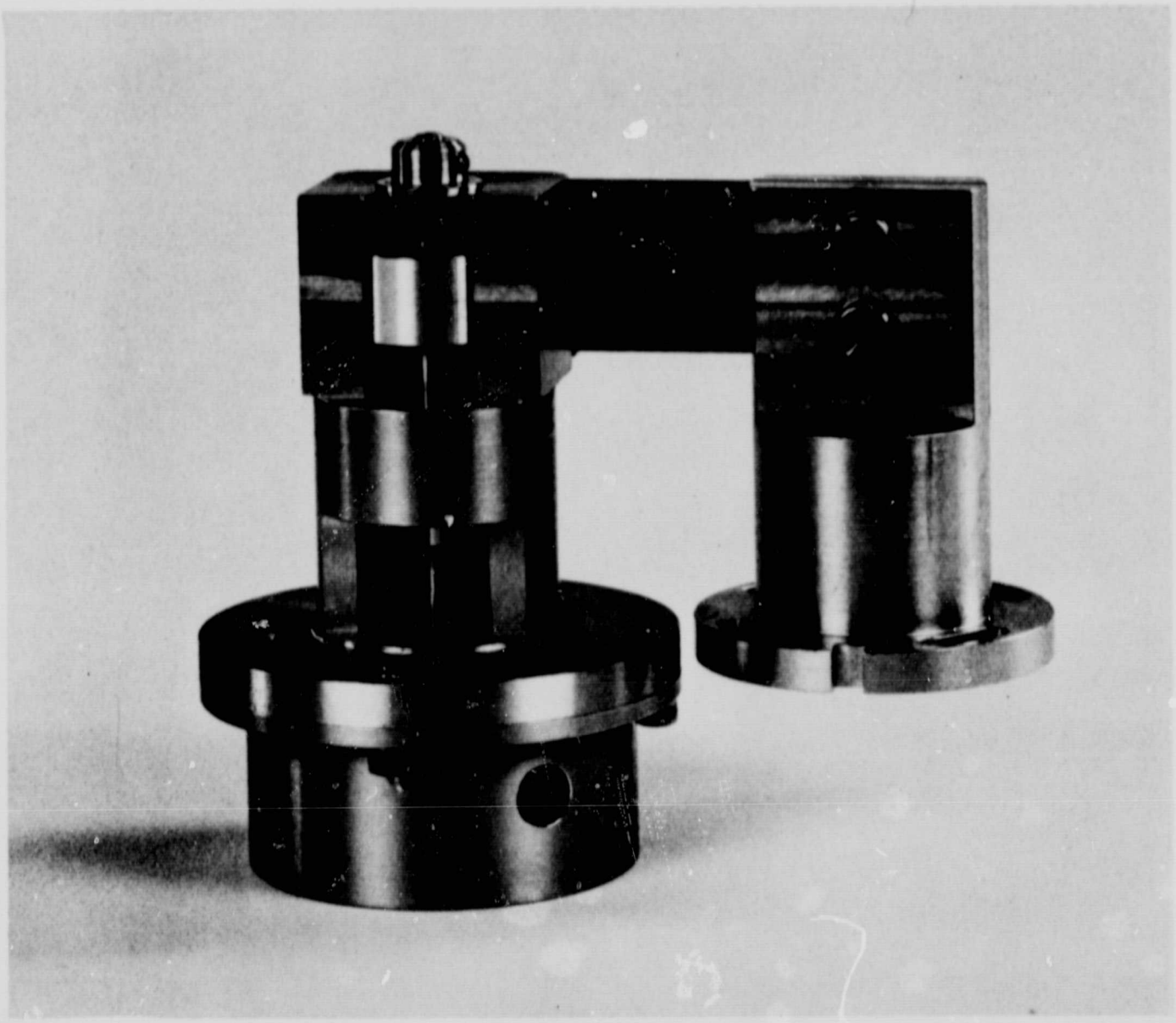

Figure 4-10. Full Scale View of the Data-Pickoff Assembly for the Azimuth Axis Turntable

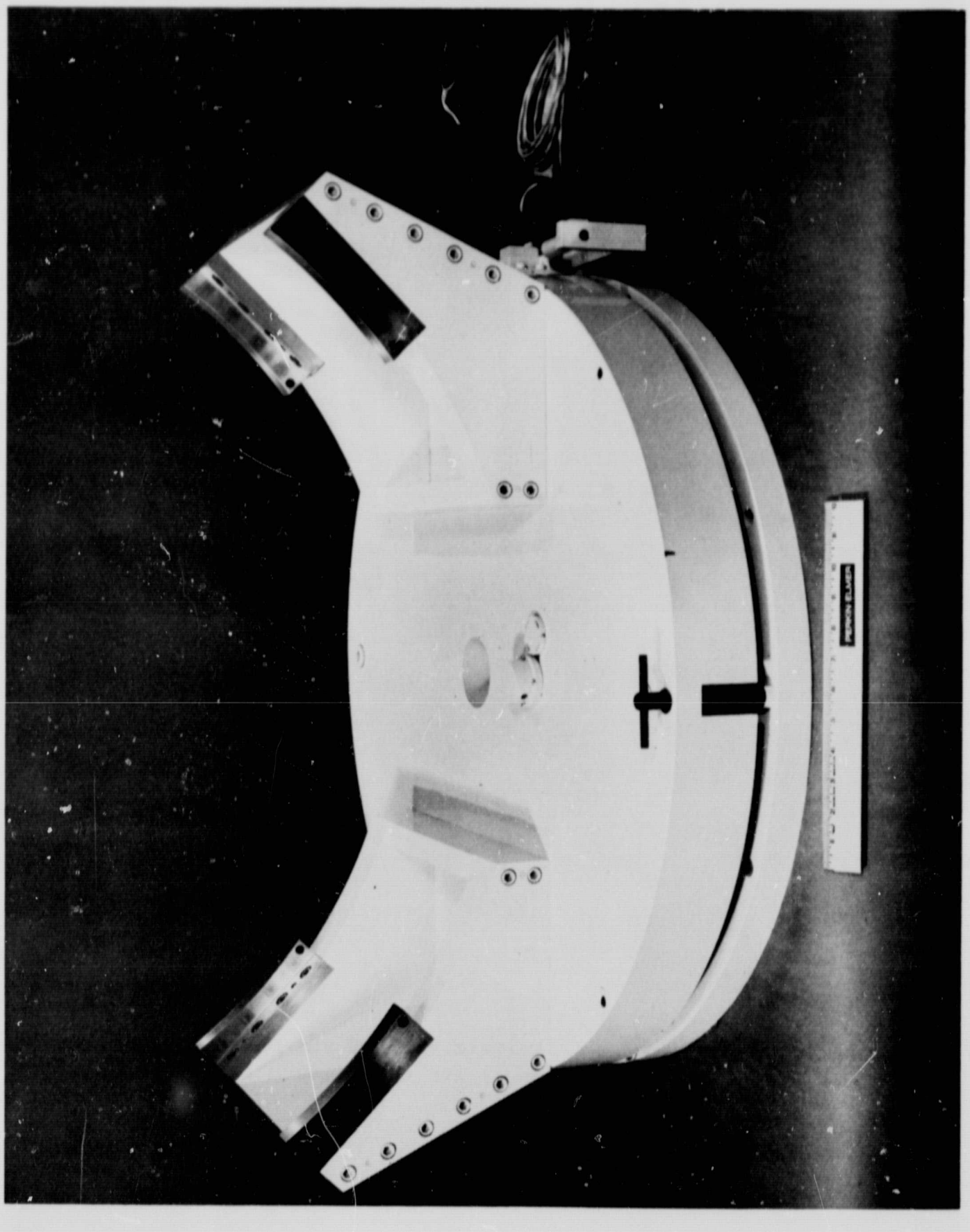

Figure 4-11. Azimuth-Axis Turntable Assembly.

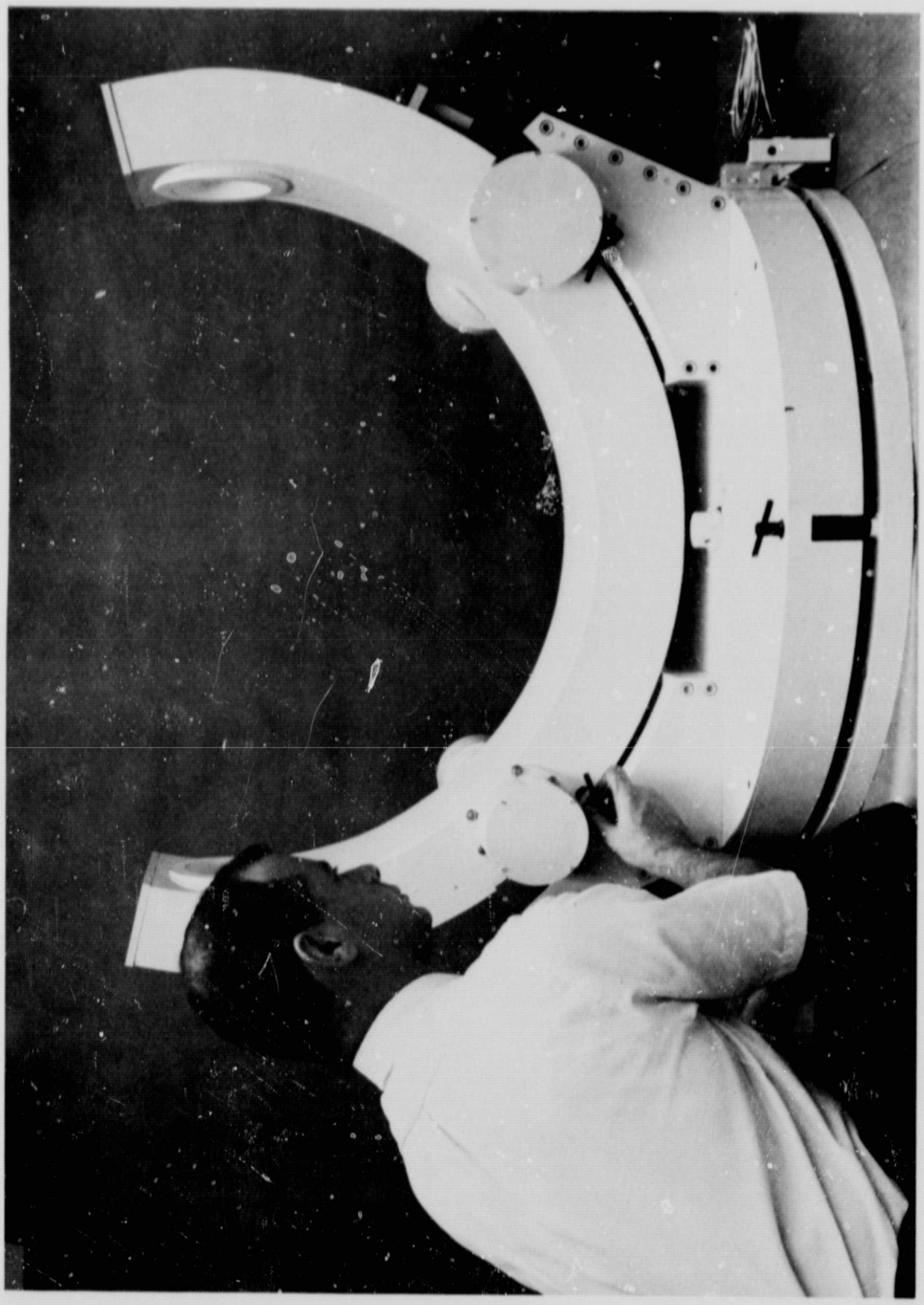

Figure 4-12. Roll-Axis Yoke Assembly Fitted tc Azimuth-Axis Turntable Assembly

SECTION V

SIMULATION EQUIPMENT

5.1 INTRODUCTION

Given a laser telescope and its associated four-axis mount, one is confronted with the problem of how to test the equipment in the laboratory under conditions that realistically simulate operation in space. More particularly, first, a platform must be provided to minimize large, random pointing disturbances resulting from floor vibrations; second, a simulated beacon source must be provided in an array that directs a plane wavefront toward the laser telescope as if, for example, the source were 100 million miles away; and third, means must be provided for observing the far field pattern of light transmitted back toward the beacon source by the laser telescope.

5.2 EQUIPMENT ARRANGEMENT

The laser telescope and an f/7 collimator are mounted at opposite ends of a vibration-isolated optical bench, a Newtonian diagonal mirror being used to fold the focal plane of the collimator across the optical bench near its midpoint. The optical bench consists of a heavily reinforced concrete slab in the form of a large triangular plate supported by three 12-inch Barry Serva Levl pneumatic mounts. The resonant frequency of the optical bench is approximately 1.6Hz, and floor vibrations above about 2 Hz are accordingly attenuated. Construction details are shown in Figure 5-1.

The clear aperture of the collimator is 19 inches which ensures by over-illumination that the 16-inch aperture of the laser telescope is fully illuminated by beacon light. The collimator is on loan to the project. It is typical of Perkin-Elmer's optical laboratory test equipment and has been shown by scatterplate interferometry to have a surface precision of better than $\lambda/10$ peak error over the unobstructed clear aperture

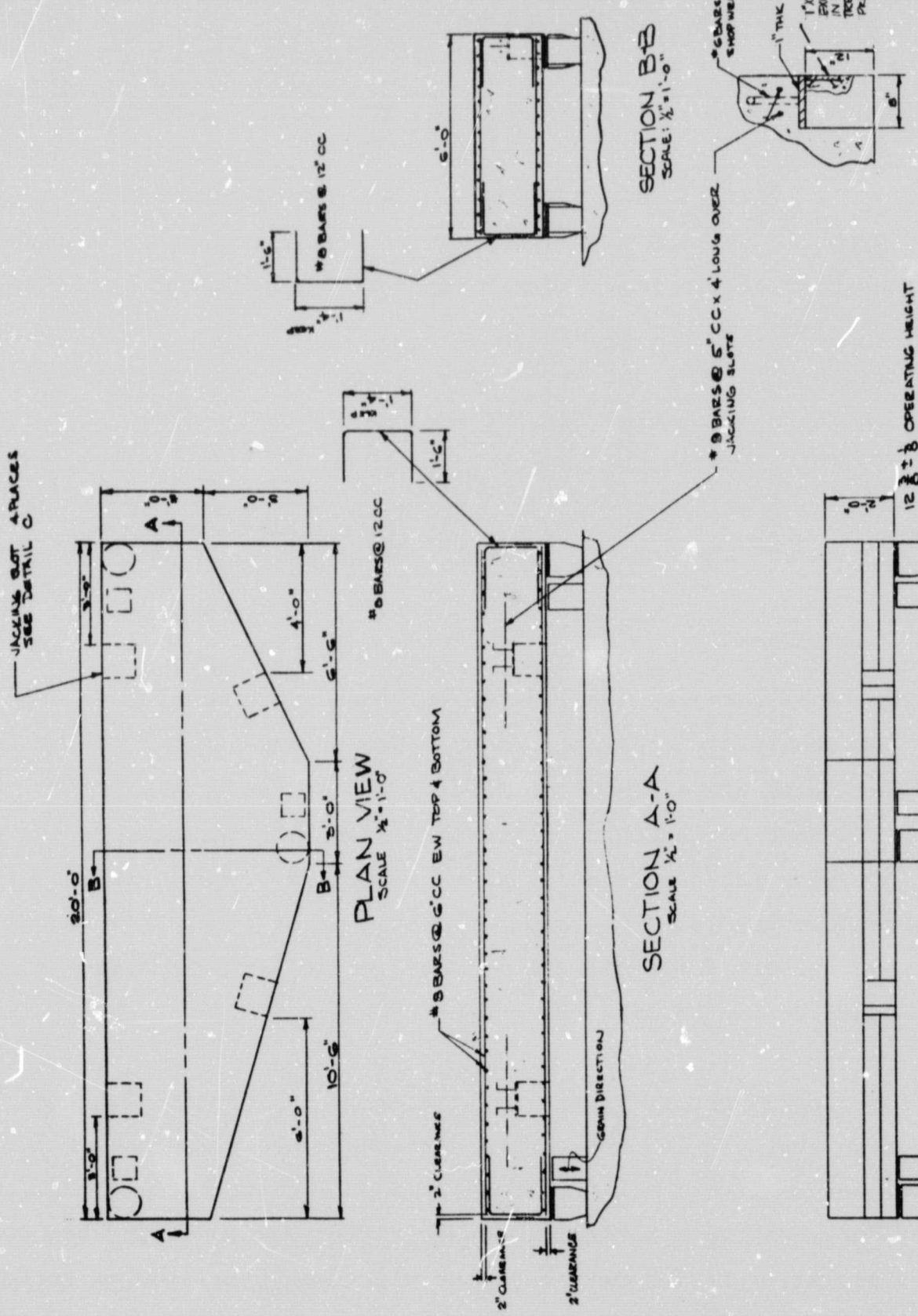

Figure 5-1. Layout of Vibration-Isolated Optical Bench

The collimator is surrounded by an aluminum housing to which is attached a tubular aluminum shroud that flares out and surrounds the end of the laser telescope. The telescope tube is sealed to this shroud by means of a compliant diaphram. The diaphragm does not appreciably impede motion of the telescope in any of its four axes. The outer surface of the collimator housing and shroud structures are insulated with a 2-inch thick layer of polyurethan foam. The telescope is hermetically sealed to the collimator in this way, and the air between the telescope and collimator is as still and isothermal as can readily be achieved in the laboratory.

The focal plane of the collimator is brought out through a hole in the side of the tubular shroud into which is sealed a Barlow lens. This lens also serves to convert the f/7 cone of the collimator to f/15 for the convenience of the additional beacon simulator optics.

The shroud structure is supported independently with respect to the collimator and diagonal mirror mounts. Thus optical alignment is unaffected by thermal expansion of the long tube between the telescope and collimator.

5.3 OPTICAL LAYOUT OF SIMULATION AND TEST OPTICS

Additional optics are shown in the layout of the beacon simulator equipment depicted in Figure 5-2. Their purpose is to provide a beacon source and to enable verification of the capability of the laser telescope under simulated space conditions. The major disturbances likely to be encountered in space operation include fading of the beacon signal, earthshine, background noise, and torquing (resulting in mispointing) of the laser telescope, due to mechanical disturbances from the spacecraft. The results of the simulation experiments are intended to provide data for predicting the performance of the laser telescope-spacecraft combination. The results can also aid in optimizing the design of the transfer lens servo for a particular launch configuration.

At the outset of the design of the beacon simulator, an investigation was carried out to determine the most appropriate equipment approach for these measurements. It was originally expected that the equipment would be designed around a flying spot scanner (cathode-ray tube) used as the beacon

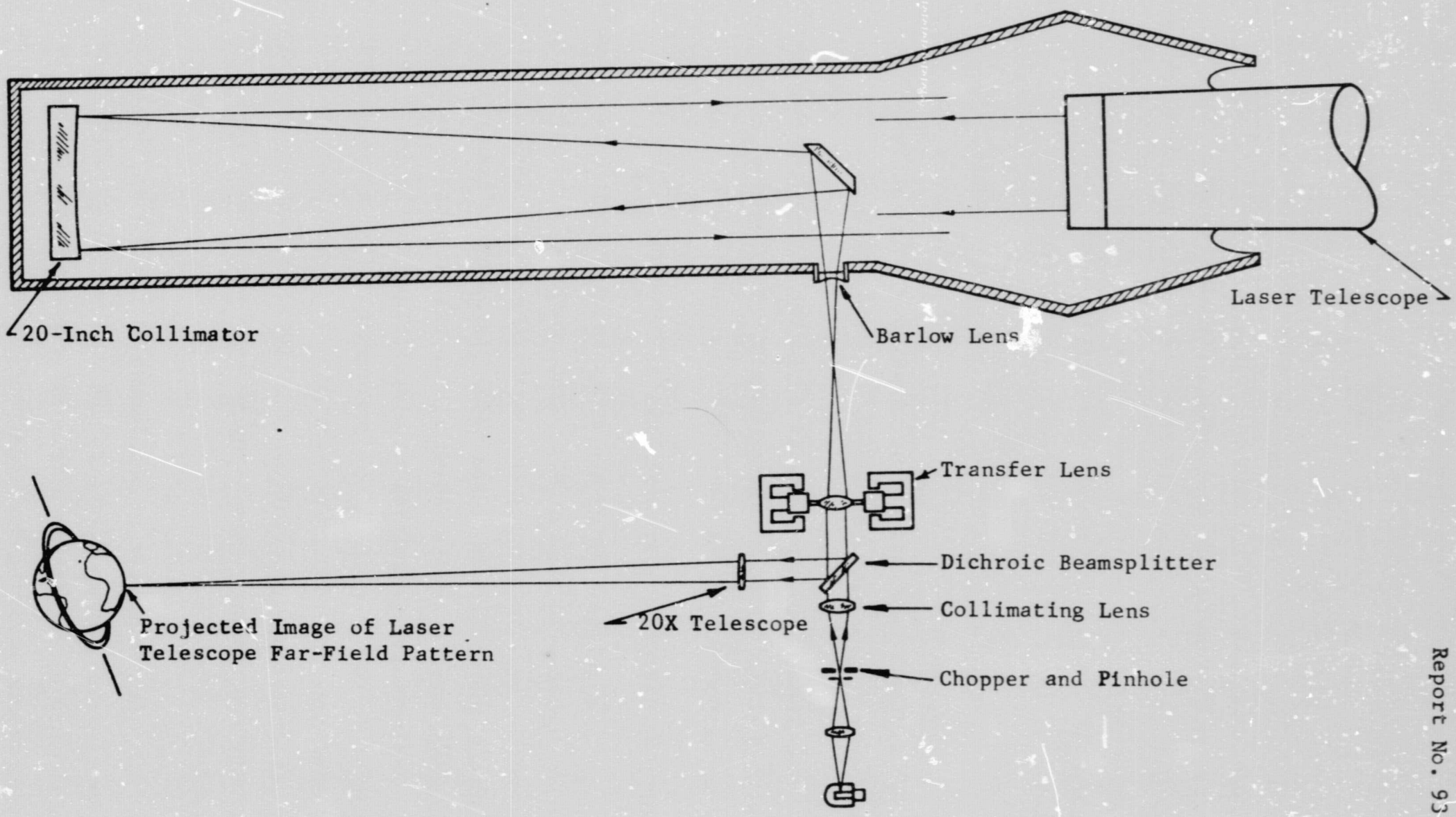

Figure 5-2. Optical Arrangement of Beacon Simulator and Test Setup

source; however, this approach has a serious shortcoming. Measurement of relative fluctuations between the beacon source and the image of the transmitted He-Ne beam is extremely difficult when the source itself is moving. A preferable approach is shown in Figure 5-3, and is based on the use of a transfer lens to move an image of a simulated beacon source. As the result of this arrangement, the error sensor serves to measure only relative fluctuations between the beacon and the beam transmitted by the laser telescope (i.e., tracking error).

The existing refractive transfer lens assembly of the Laser/Optics Techniques breadboard is ideal for this application, and was therefore integrated into the beacon simulator as shown in Figure 5-2.

The light source consists of a ribbon filament lamp imaged onto a pinhole. This source is chopped at 1600 Hz by a tuning fork (as required by the tracking system of the laser telescope) and is powered by a well regulated, programmable power supply. Circuitry was also built to program the supply to simulate atmospheric scintillation (fading). Experiments were carried out to ensure that the beacon source could be modulated with an adequate depth to beyond the response of the transfer mirror servos (i.e., 100% at D.C. to greater than 25% at 50 Hz).

Provision was made to align the telescope optics in place on the four-axis mount with the aid of an autocollimating flat installed temporarily on the vibration-isolated optical bench. A close-up view of this arrangement is shown in Figure 5-4. The flat was then removed, the shrouds were installed, and the complete experimental setup was then as shown in Figure 5-5.

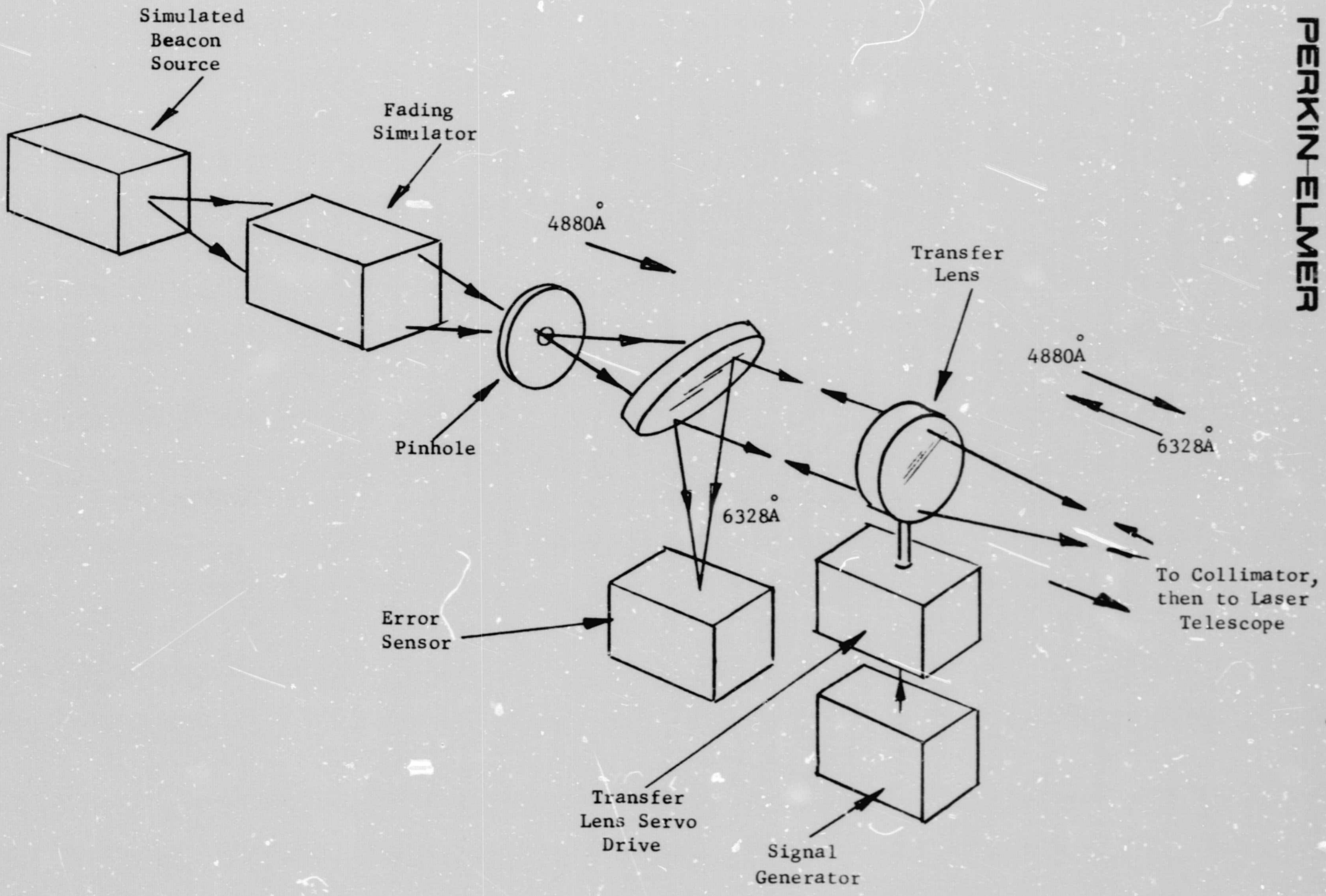

Figure 5-3. Beacon Simulator Equipment Configuration

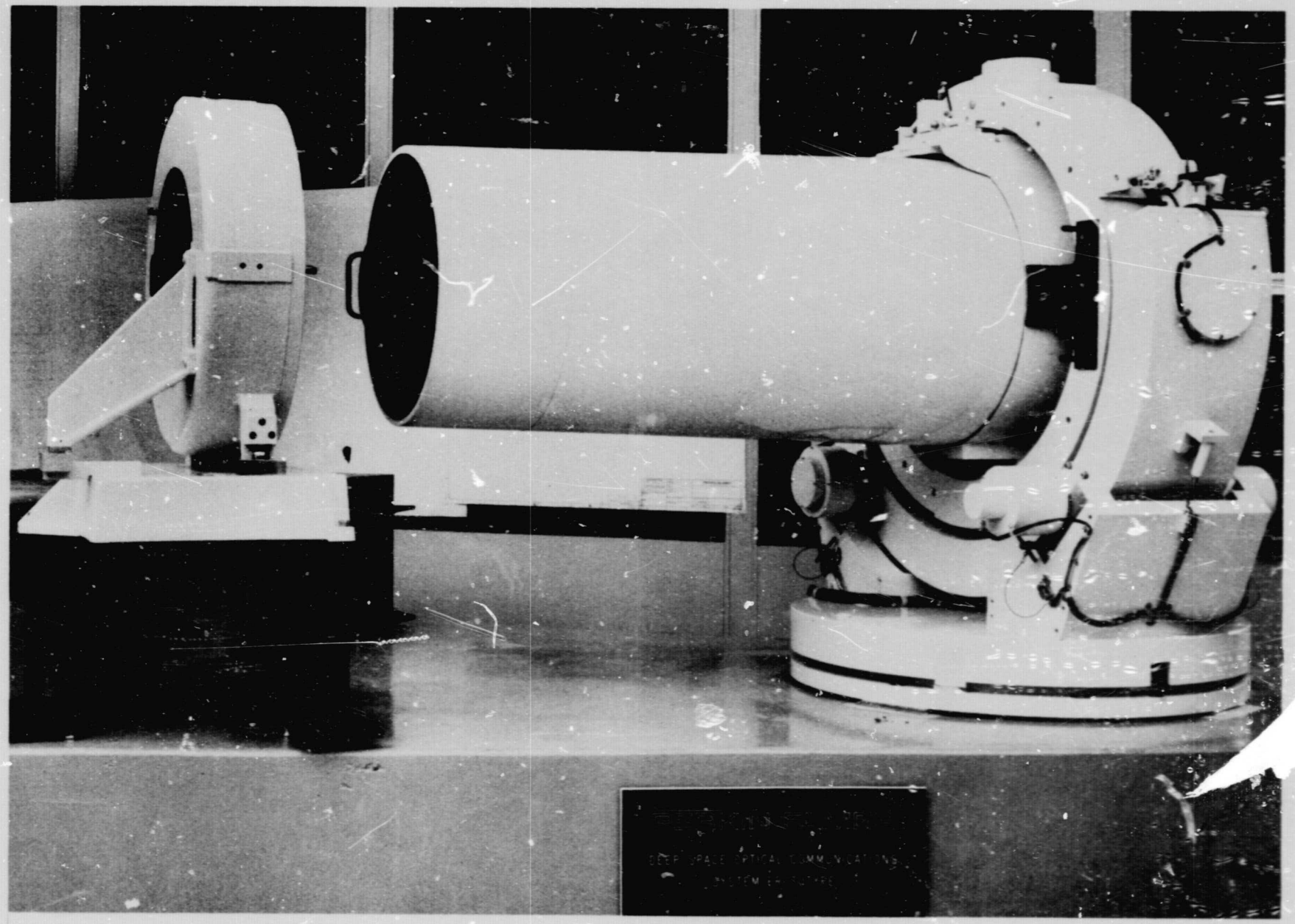

Figure 5-4. Close-up View of Laser Telescope Swung Over to Face 20-Inch-Diameter Autocollimating Flat.

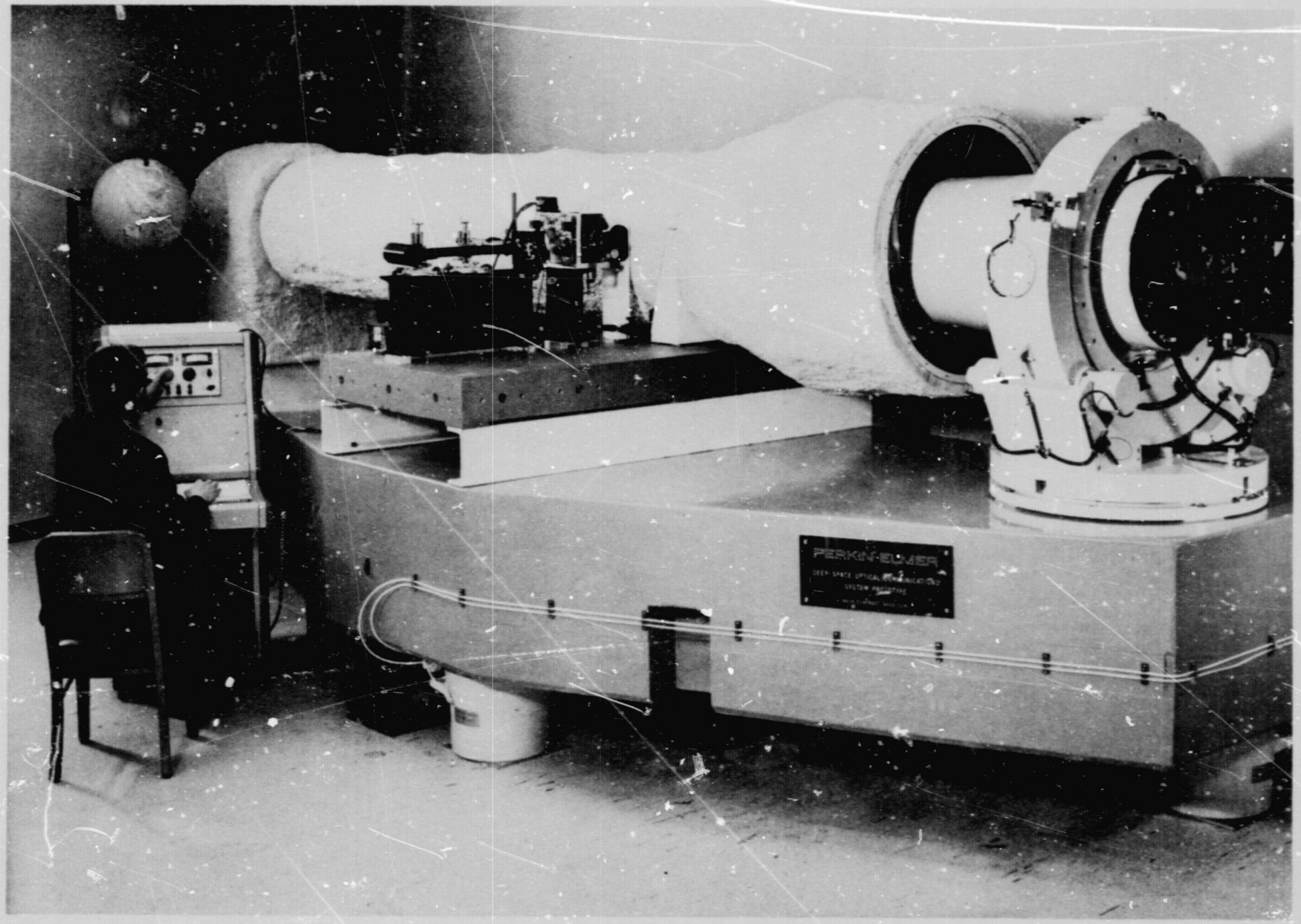

Figure 5-5. Laboratory Test Setup for Development Testing of the Prototype Deep-Space Optical Communications System

SECTION VI

ELECTRONIC DESIGN

6.1 INTRODUCTION

The electronic design of the laser telescope and its associated four-axis mount is described in detail in this section. The overall functional block diagram of the system is given for reference in Figure 6-1, and its planned operational modes have been discussed in earlier reports.[1,2]

The system is essentially a multiple-loop, null-balanced servo system with an optical image splitter and a quadrant multiplier phototube (QMP) as the fine error sensor.[3] In the main operational sequence, the gimbals are first commanded to slew toward the beacon line of sight. Once the beacon image is picked up by the 1-degree field of the coarse-acquisition system, signals are developed that provide take-over control of the gimbals such as to move the telescope until the beacon image enters the central 2-arc-minute fine-guidance field. Then the gimbal servos and the transfer mirror servos operate to drive the image to zero error. In this condition the laser telescope is tracking the beacon line of sight and pointing a transmit beam with respect to the beacon line of sight to a design-goal accuracy of less than 1/10-arc-second error.

6.2 COARSE-ACQUISITION AND FINE-GUIDANCE BLOCK DIAGRAM DESCRIPTION

The individual electronic block diagrams of the coarse-acquisition and fine-guidance systems are shown in Figures 6-2 and 6-3. The coarse-acquisition system operates merely as an on-off controlled servo, while the fine-guidance system seeks null balance in a comparatively small linear range.

---

[1] Perkin-Elmer Engineering Report No. 8500

[2] Perkin-Elmer Engineering Report Nos. 8387 and 8631

[3] R.C. Liu, M.S. Lipsett, and A.M. Ledger, Fine Error Sensor for Null-Tracking Diffraction Images, J. Opt.Soc.Am., 58, 718 (1968)

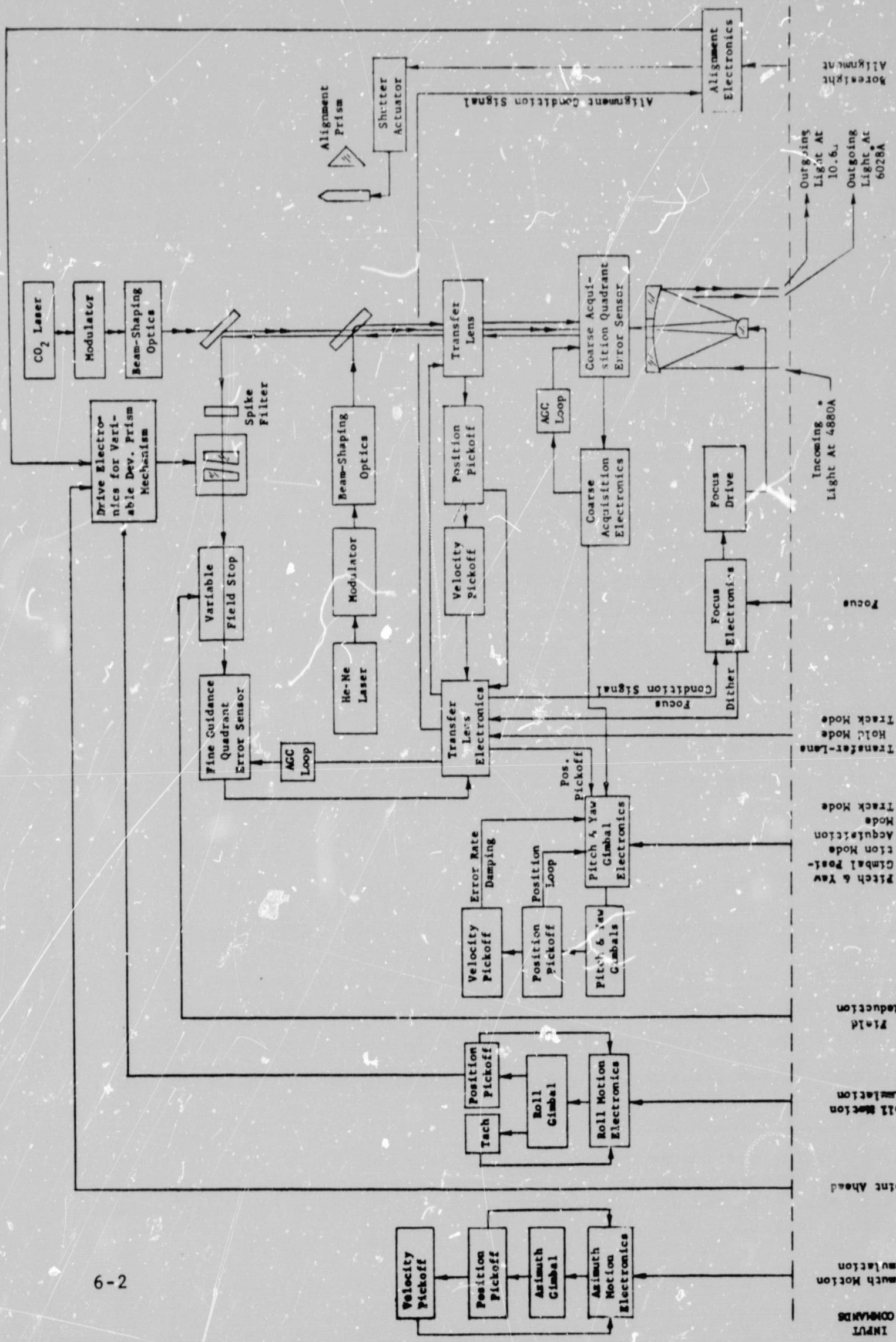

Figure 6-1. Functional Block Diagram of Laser Telescope and Mount

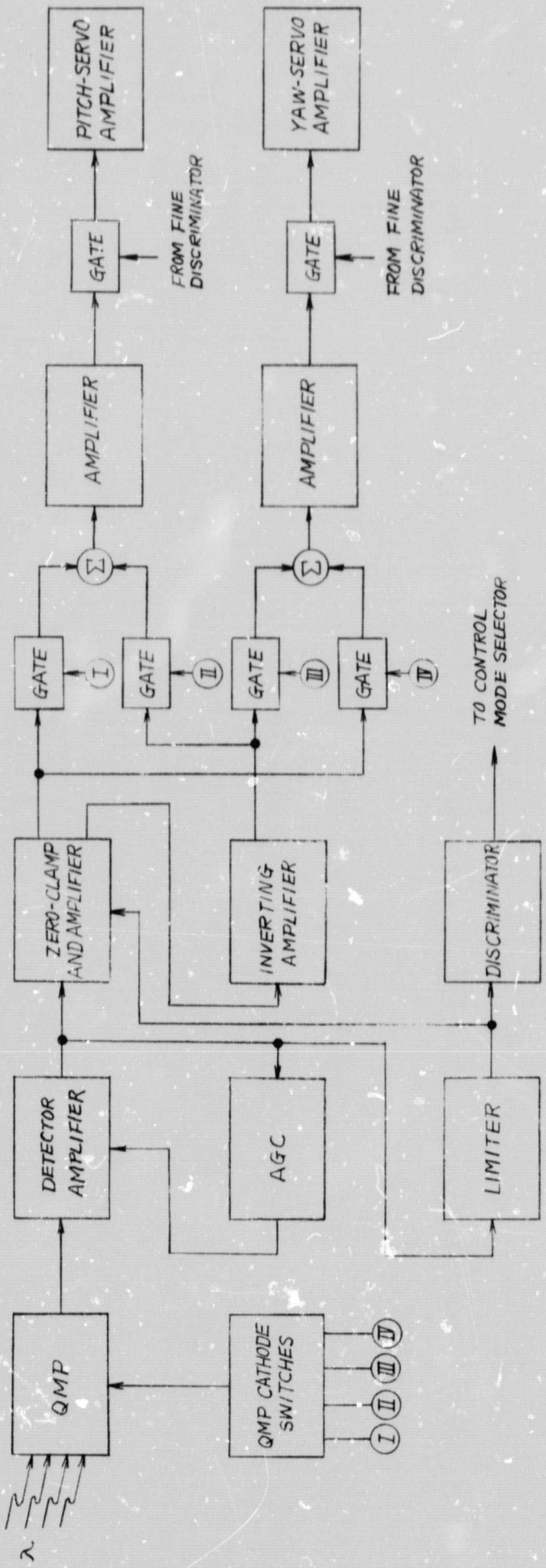

Figure 6-2. Block Diagram of Coarse-Acquisition Electronic Subsystem

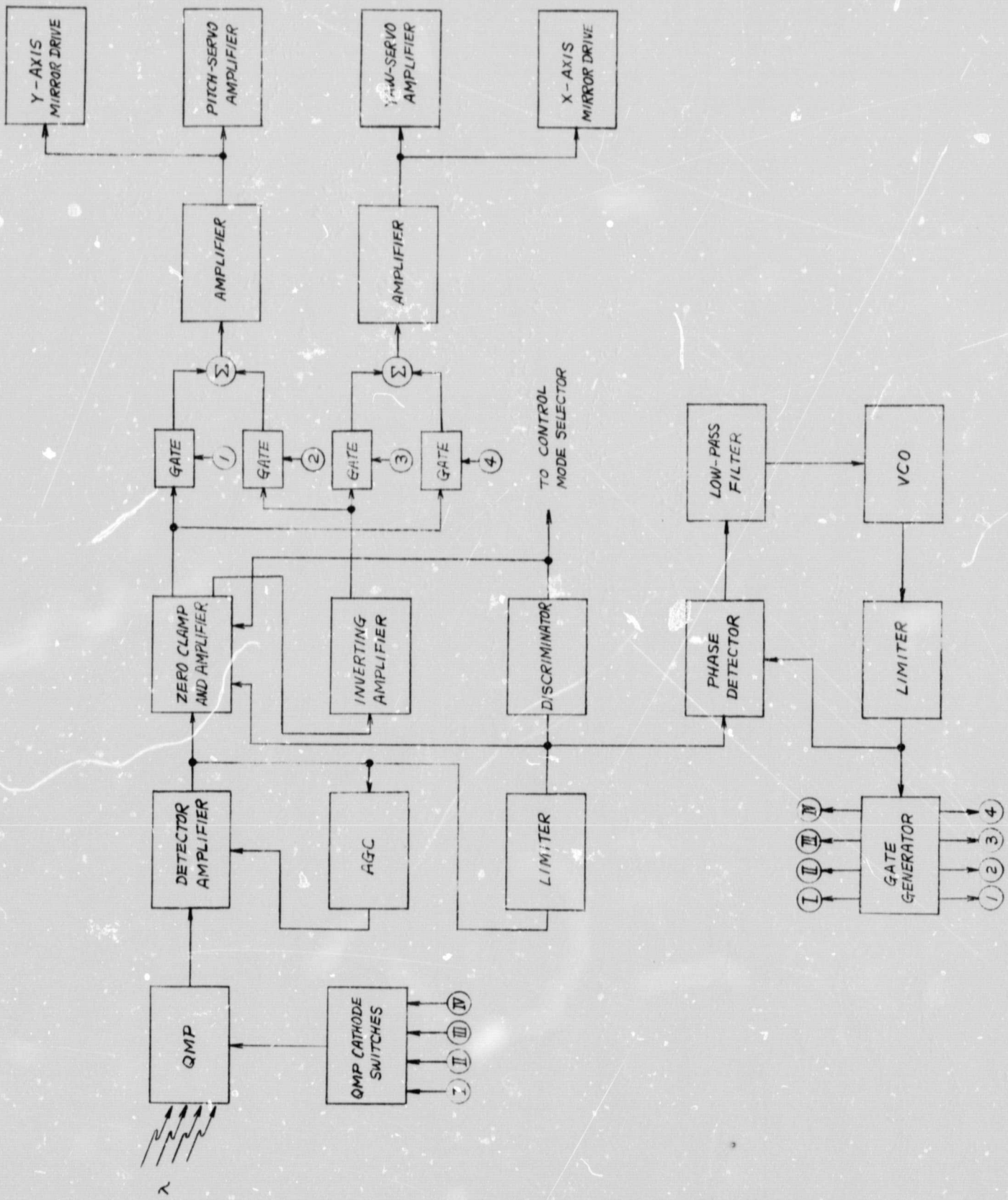

Figure 6-3. Block Diagram of Fine-Guidance Electronic Subsystem.

Beacon light entering the coarse field is routed to the coarse sensor through the field divider prism described previously.[4] The up, down, left, or right sense of the angular error is then determined from the waveform appearing in the QMP output.

Beacon light entering the fine field is relayed by the transfer mirror to the image divider prism, where it is divided into four parts and then fed into the fine sensor QMP. If the image is located precisely at the apex, the four output signals are of equal amplitude. If not, the QMP produces signals of unequal amplitude. The coarse-acquisition signals are amplified, decommutated, and then sent into the gimbal servo amplifiers. The fine sensor error signals are similarly decommutated but are routed to the transfer mirror servo drives. Signals are also developed in the fine-guidance mode to drive the gimbals so as to maintain the transfer mirror in the nominal center of its range.

6.3 SIGNAL PROCESSING CIRCUITRY

The circuit details of the signal processing as well as the operating principle are described in this section. Since the signal processing circuits in the fine-guidance and coarse-acquisition systems are essentially identical except for the decommutating logic gates, only the circuits in the fine-acquisition system will be discussed. In principle, common fine and coarse tracking signal processing circuitry is possible except for the signal channels following the sensor detectors. However, this approach was not attempted because the QMP image locations in the fine and coarse sensors with respect to the gimbal axes were not designed to be identical.

6.3.1 QMP Sensors

EMR type 573-E quadrant multiplier phototubes are used in both the coarse-acquisition and fine-guidance systems. Quadrant switching is accomplished by employing four field effect transistors in series with each cathode as shown in Figure 6-4. The "on" condition in a given quadrant is achieved by

---

[4] Perkin-Elmer Engineering Report No. 8631

lowering the drain resistance of the FET when a control signal to the gate is received through a capacitor-coupled circuit so that the cathode potential becomes about the same as the bias electrode potential. Likewise, the "off" condition is obtained by placing a high resistance in the cathode circuit so that the bias electrode becomes sufficiently negative with respect to the cathodes. While the switch networks are operated nominally at -2800 volts, the transistors are well protected by zener clamps between each gate and source. Sufficiently fast cathode switching is achieved by lowering the drain resistor value with a shunt voltage bleeder so that the drain currents are not restricted by the dynode voltage divider resistor value.

The gate drive waveforms for each quadrant are also shown in Figure 6-4. A cathode switching rate of 400 Hz was selected as required by the 1.6-KHz chopping frequency selected for the beacon source. The relationship between cathode switching rate and beacon modulation prevents ambiguity in the QMP output signals.

6.3.2 Detector Amplifier

As the output of the QMP has a relatively high impedance, it is necessary to provide impedance matching for further amplification. Each detector amplifier, which is mounted close to its respective QMP, consists of a wideband FET operational amplifier with a light-controlled photoresistor (Raysistor) as the feedback element. This circuit is shown in Figure 6-5. The output level is maintained constant to make the system relatively independent of beacon light intensity. Although this could have been done by controlling the anode supply voltage of the phototube, a simpler automatic gain control circuit was devised. It utilizes the effect of large change in photoresistance from a small change in lamp current of the Raysistor, and the same result is accomplished. Another feature of the Raysistor AGC circuit is its ability to de-emphasize high frequency response by automatically increasing the time constant of the amplifier whenever the signal level becomes low.

The output signals of the detector amplifier contain the image position information in the form of pulses. Hence, short rise-time, small

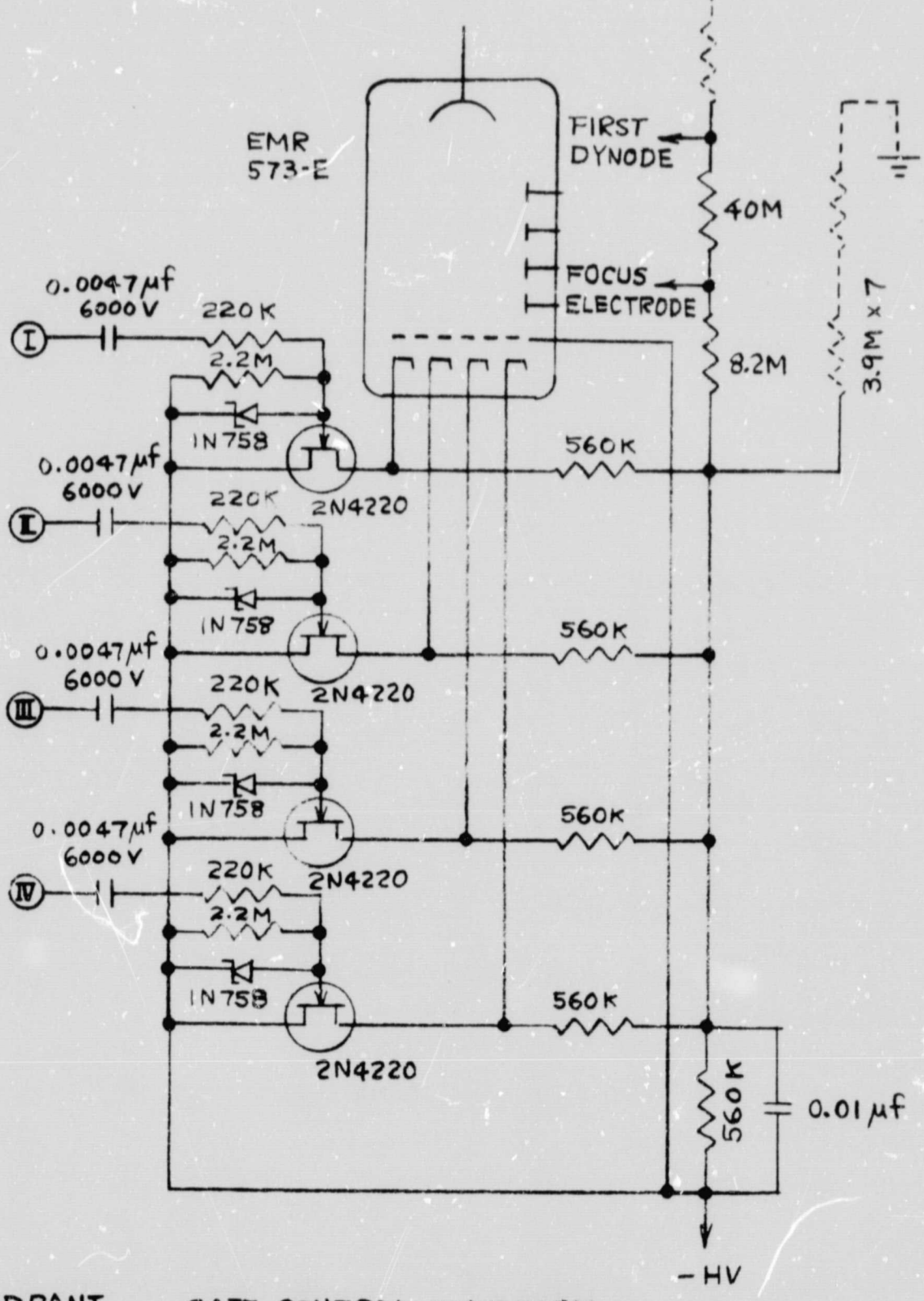

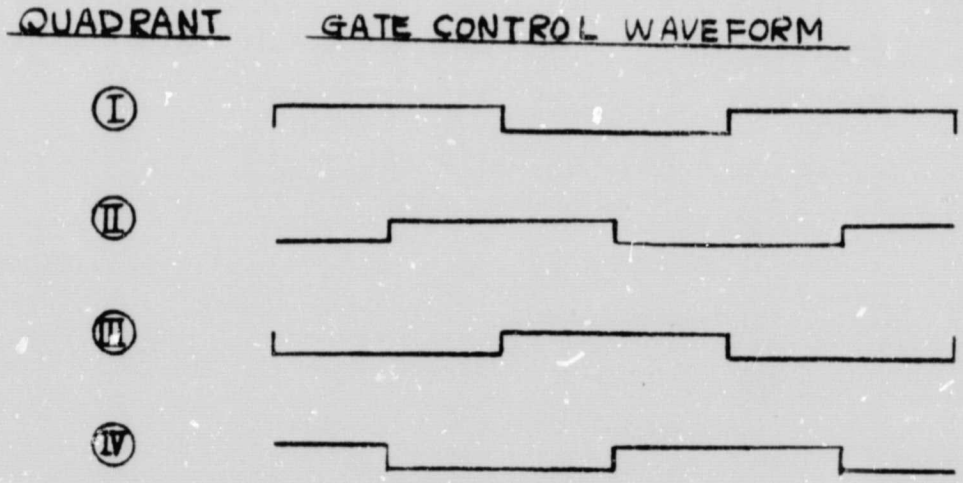

Figure 6-4. Cathode Switching Circuit of QMP and Gate Control Waveforms.

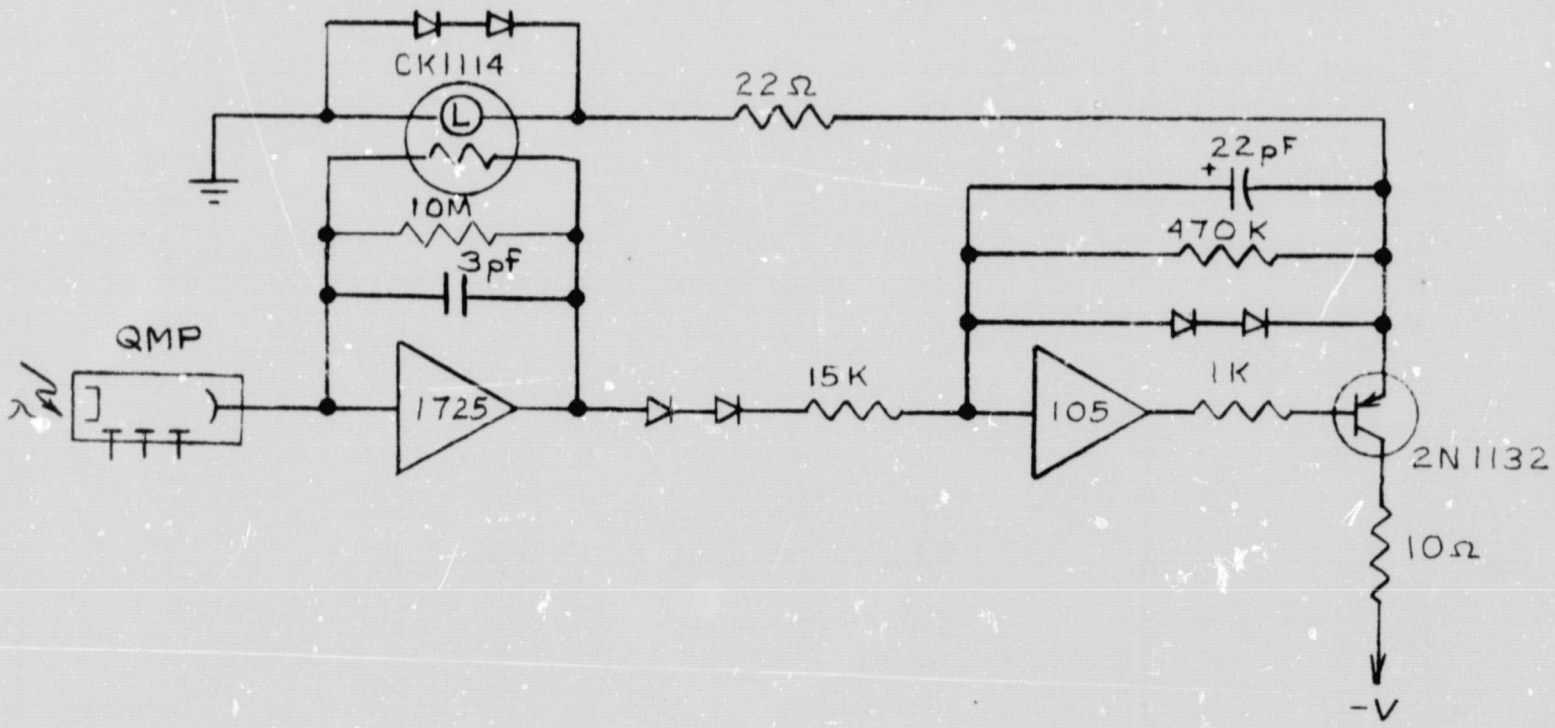

Figure 6-5. Detector Amplifier with Light Controlled Photoresistor to Provide Automatic Gain Control

overshoot and wide response characteristics of the preamplifier circuitry are necessary, although some high-frequency de-emphasis must be provided to reduce photon noise. Accordingly, a 3 pF capacitor is added across the feedback element. As described later, in order to avoid additional lag from the detector amplifier when the beacon signal intensity is low and the feedback resistance value is extremely high (affecting the stability of the position loop), a 10 -megohm resistor is added across the input and output points of the amplifier.

A series clipper with two diodes is connected between the detector amplifier and the AGC amplifier. Any voltage greater than two energy gaps is thus amplified to alter the illumination incident on the photoresistor and thereby change its resistance. This AGC circuit has a control range of approximately three decades of equivalent resistance, and is limited mainly by the effect of the shunt resistor. It is therefore able to compensate for a signal variation of 1000 to 1.

The top waveform of Figure 6-6 is a typical waveform of the fine-guidance detector amplifier when the image is located very close to the apex of the splitting elements. The bottom four waveforms are of the quadrant switch control gates. It should be noted that the signal waveforms on the top are produced by quadrants IV and I, I and II, II and III, III and IV, and IV and I from left to right.

The transfer ratio of the combined image splitter, QMP, and detector amplifier was measured as 1/6 volt per arc-second of telescope orientation.

6.3.3 Limiter

The output signals of both detector amplifiers are clipped in order to operate a synchronous clamp to generate the quandrant switching and signal processing control logic gates, and to discriminate between coarse and fine control modes. A very effective limiter circuit was devised that uses an operational amplifier with a bridged reference diode as shown in Figure 6-7. The reference diode provides a semifloating stable voltage which is established from the plus and minus power supplies with two series resistors.

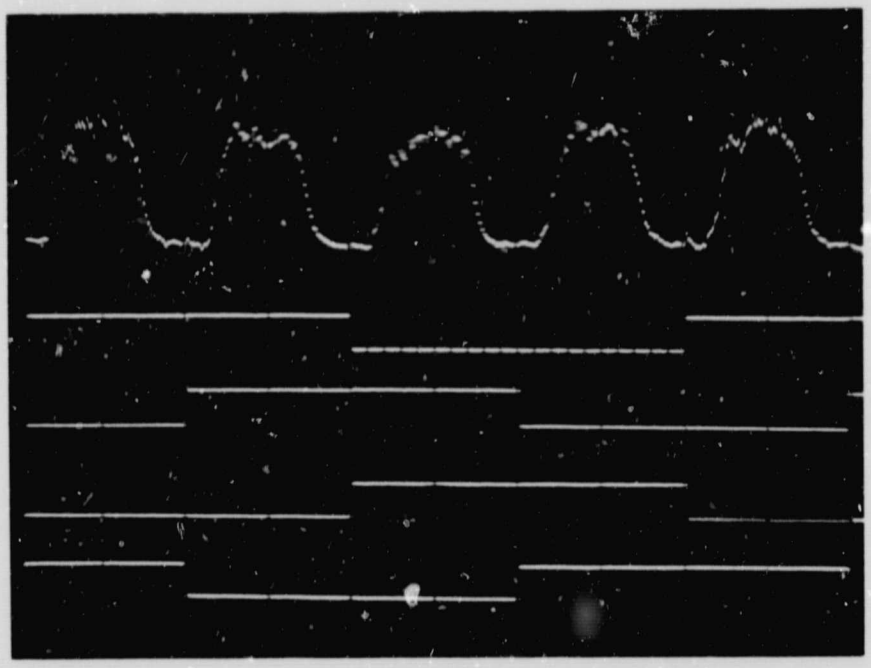

Figure 6-6. Typical Fine-Guidance Detector Amplifier Output Waveform (Top) and Quadrant Switch Control Waveforms

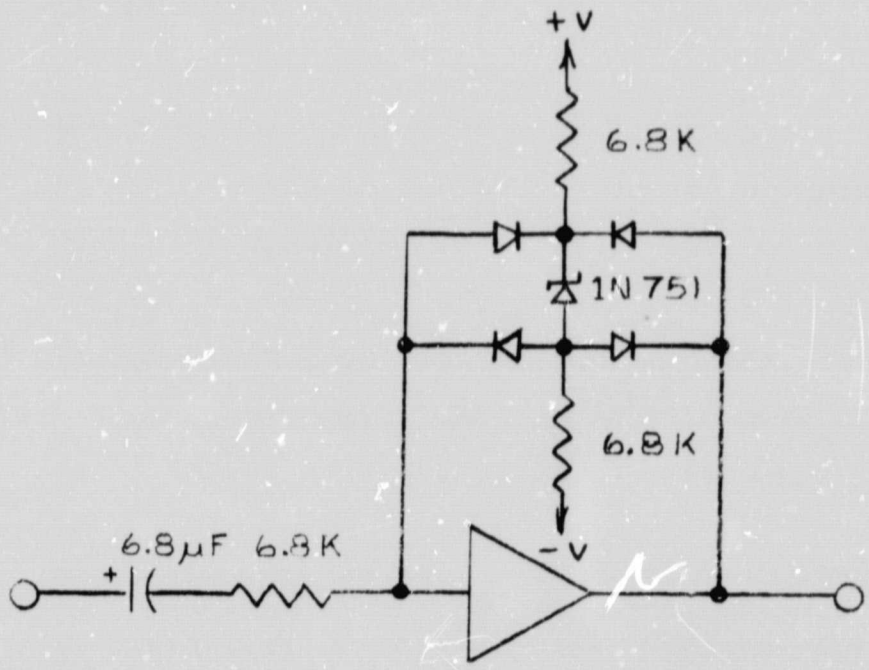

Figure 6-7. Bridged Reference Diode Limiter Amplifier to Provide Sharp Zero-Crossing Transition with Symmetrical Amplitude Clipping

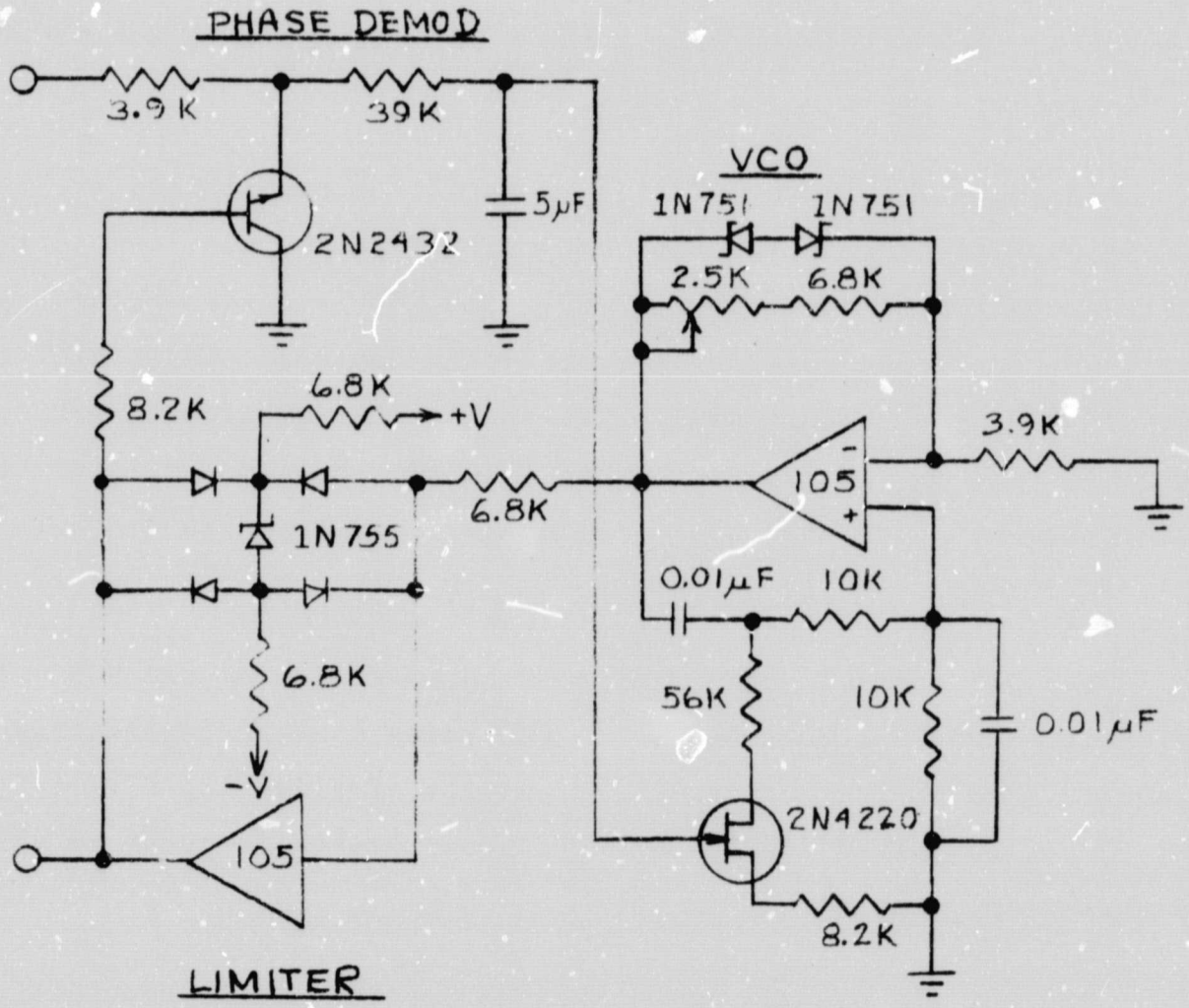

Figure 6-8. Phaselock Loop for Generation of 90-degree Phase-Shifted Squarewave

When clipping occurs, the top and bottom terminals of the reference diode are connected to the summing point and the output of the operational amplifier, the polarity depending on the polarity of the input voltage. Since a stable voltage is always established across the reference diode and the high forward path gain of the amplifier is not reduced by a shunt between its output to input during the transitional period, symmetrical, hard-amplitude clipping is obtained with sharp zero-crossing transitions.

6.3.4 Control Gate Generator

Since the system employs time-division multiplexing, various control gates are necessary for signal processing as well as for quadrant cathode switching. In order to minimize possible crosstalk arising in the multiplexing system, the control gates are synchronized to the input signal so that pulse signals are always limited in their assigned time slots. The control gates are generated by using a phase lock oscillator, a binary divider chain, and a logic diode matrix.

As shown in Figure 6-8, the signals from the limiter are fed into a phase-sensitive demodulator to compare the phase relationship with a local voltage-controlled oscillator (VCO). The VCO is a Wien-bridge network with a voltage-controlled resistor for frequency control. The oscillator output is clipped by a circuit similar to the limiter previously mentioned. The control voltage is applied to the VCO from the phase demodulator to change the frequency such that the output signal generated is a square wave phase-shifted 90 degrees with respect to the input.

The QMP control gates are produced by following the VCO output by the circuit shown in Figure 6-9 which generates four 90-degree phase-shifted square waves. The complementary outputs of flip-flop FF-1 trigger a pair of flip-flops, FF-2 and FF-3, and a proper reset is provided in order to avoid phase ambiguity.

The way the signals are processed for the coarse-acquisition and fine-guidance systems is illustrated in Figures 6-10 and 6-11. The illumination of the QMP photocathodes is illustrated to the left, and the relationships

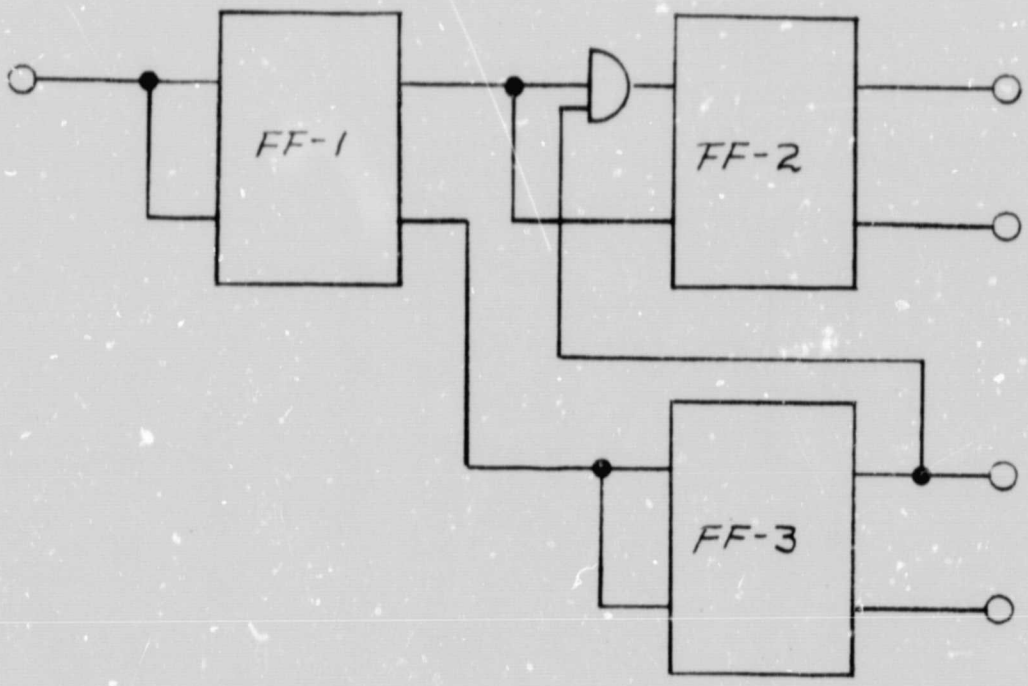

Figure 6-9. Binary Divider Chain for Generation of Four 90-degree Phase-shifted Square Waves.

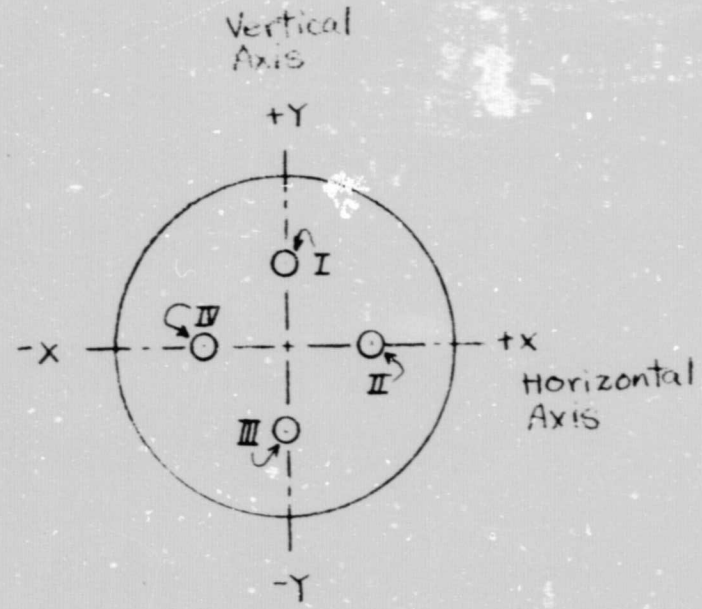

QMP Image Location

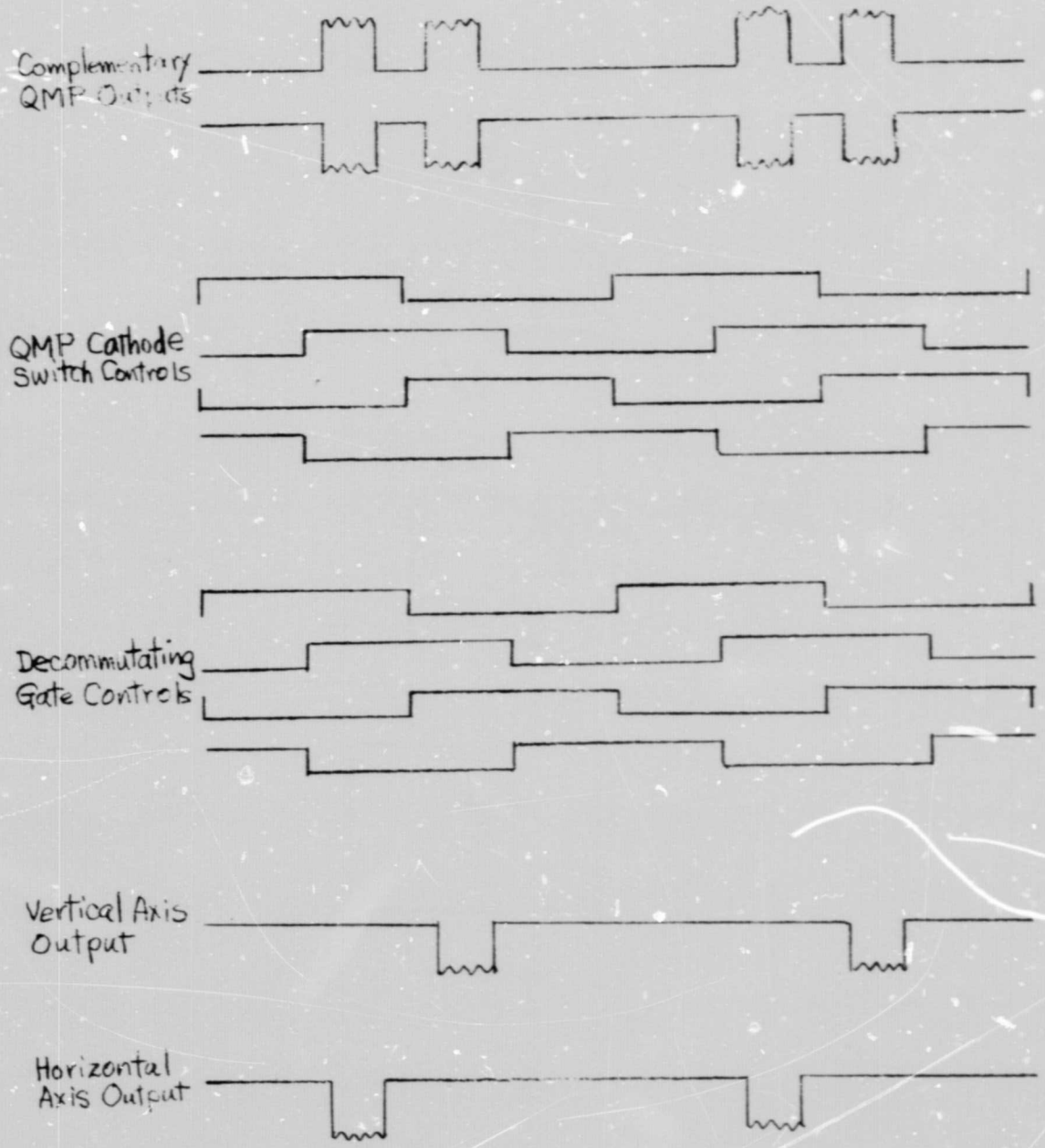

Figure 6-10. Electronic Signal Processing in Coarse-Acquisition System

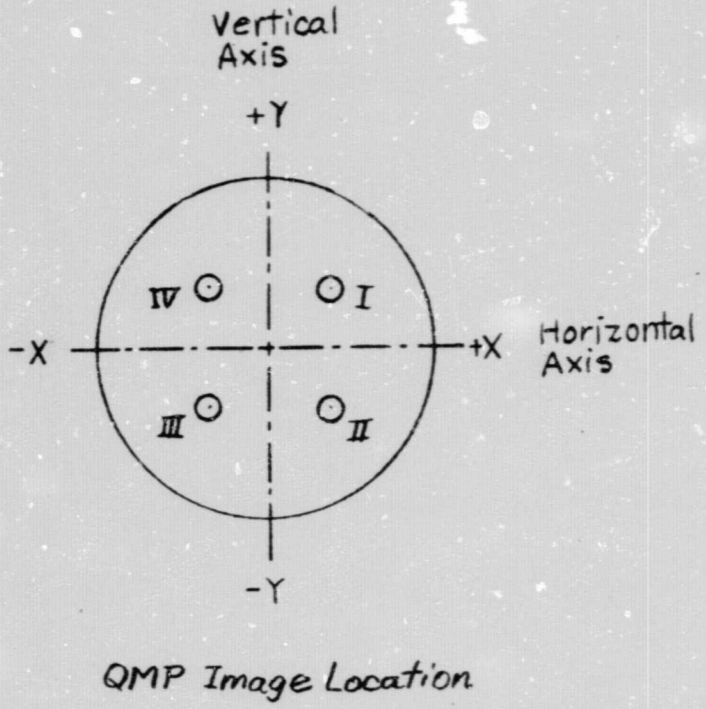

QMP Image Location

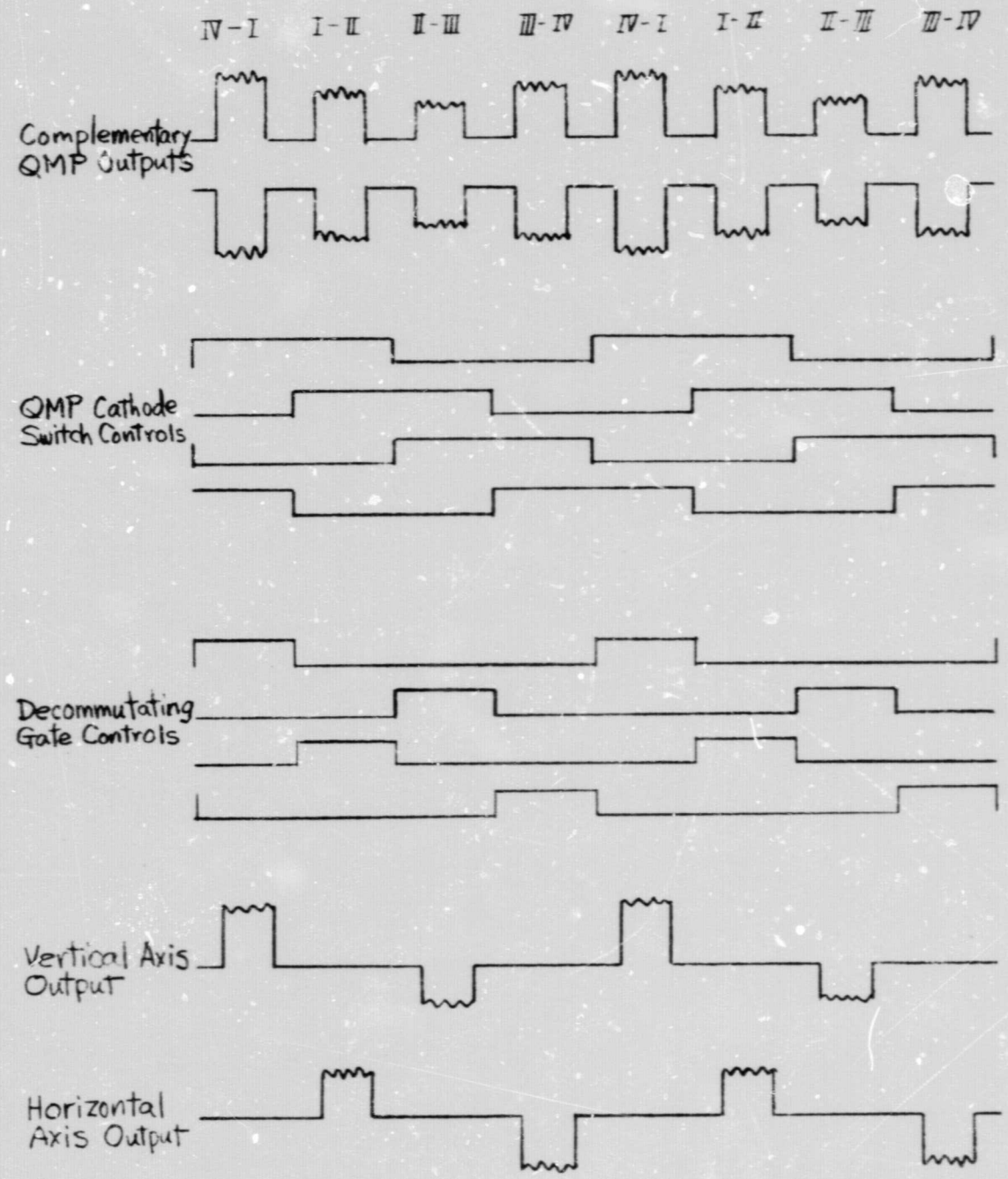

Figure 6-11. Electronic Signal Processing in Fine-Guidance System

between the quadrant switching gates and the bridge amplifier outputs are illustrated to the right. The decommutator control logic gates and the gated waveforms are also shown in the figures. Inspection of these figures shows how the decommutating gates are related to the quadrant switching gates. For instance, in the case of the fine-guidance system, we see that the vertical angular error is obtained by combining the quadrant signals in the form (IV plus I) minus (II plus III). Likewise the horizontal angular error is obtained by taking quadrant signals (I plus II) and subtracting (III plus IV). For the coarse-acquisition system, the image geometry with respect to the gimbal axes allows the quadrant switch control waveforms to be also used for decommutation. For the fine-guidance system, the decommutator gate control signals are generated by using a diode logic matrix as shown in Figure 6-12.

The frequency-determining network of a modified Wien-bridge oscillator is shown in Figure 6-13. The transfer function of the modified Wien-bridge can be expressed as

$$\frac{E_o}{E_i}(s) = \frac{sRC\,\dfrac{R_T}{2R+R_T}}{R^2C^2\,\dfrac{R_T}{2R+R_T}\,s^2 + RC\,\dfrac{R+3R_T}{2R+R_T}\,s+1}.$$

If it is assumed that for oscillation the amplifier gain is A, one obtains

$$R^2C^2\,\frac{R_T}{2R+R_T}\,s^2 + RC\,\frac{R+R_T(3-A)}{2R+R_T} + 1 = 0.$$

Thus, when $A = \dfrac{R+3R_T}{R_T}$

$$s^2 = -\frac{1}{R^2C^2\,\dfrac{R_T}{2R+R_T}}$$

Therefore, when the gain is adjusted to $\dfrac{R+3R_T}{R_T}$,

the system will oscillate at a frequency of $\dfrac{1}{2\pi RC\sqrt{\dfrac{R_T}{2R+R_T}}}$ Hz.

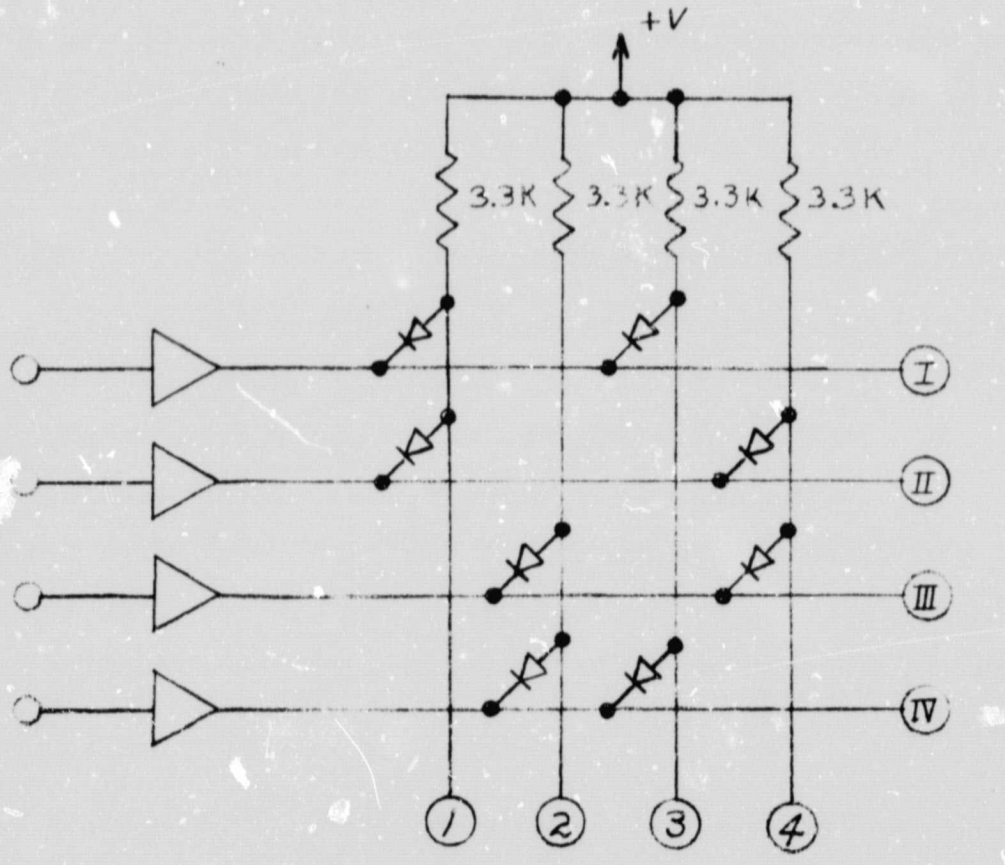

Figure 6-12. Diode Logic Matrix for Generation of Signal Processing Gates.

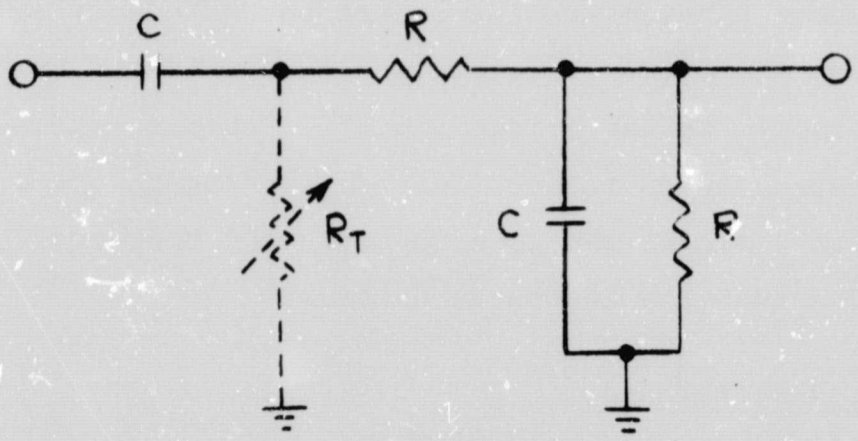

Figure 6-13. Frequency Determining Network of Modified Wien-Bridge Oscillator.

Four waveforms related to the phase-lock circuit are shown in Figure 6-14. They are, from top to bottom, the detector amplifier output, the limiter output, the VCO output, and the phase-lock circuit output.

6.3.5 Synchronous Clamp and Bridge Amplifier

The null-balance servo-system employed is inherently insensitive to dc offset of the detector amplifier. To further minimize background illumination noise, the synchronous clamp shown in Figure 6-15 is employed to restore zero level from the capacitor-coupled, detector-generated waveform. A shunt FET switch, which is synchronously "on" and "off" with respect to the beacon signal, is driven by the limiter circuit. The high input impedance amplifier and an extremely high "off" resistance of the FET switch result in undistorted waveforms.

A pair of complemental signal waveforms are needed to route the fine and coarse error signals through the signal processing logic with correct polarity to the proper torquers. These are obtained by a cascaded operational inverter having a frequency response compatible with the main amplifier. A typical detector output waveform together with the synchronously clamped bridge-amplifier outputs is shown in Figure 6-16.

6.3.6 Decommutator Amplifier

The amplitude, sense, and axis of the angular error signals have to be extracted before the signals are routed to the gimbal and transfer mirror servo amplifiers. As shown in Figure 6-17, this is accomplished by connecting the decommutator gate inputs to the bridge amplifier outputs while summing the signals by an operational amplifier. In order to smooth out dc error signals from the sampled error signal and to compensate the Bode characteristics, a capacitor is added across the feedback resistor.

6.3.7 Coarse-Fine Discriminator

A discriminator is provided in the system to accomplish handover between the coarse and fine error sensors to select the proper control mode for the servos.

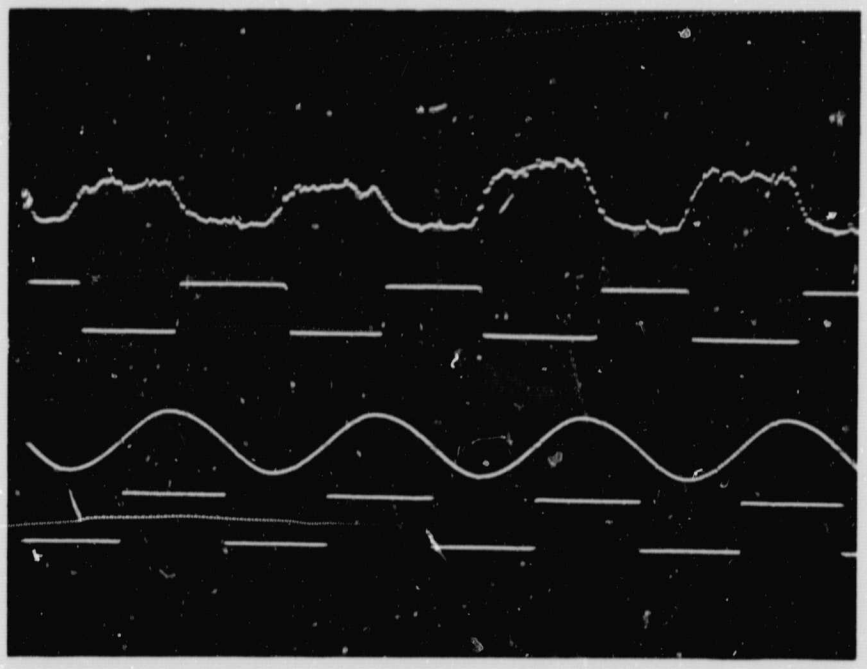

Figure 6-14. Waveforms Related to Phaselock Circuitry: Detector Amplifier Output, Limiter Output, VCO Output, and Phase-lock Circuit Output, from top to bottom.

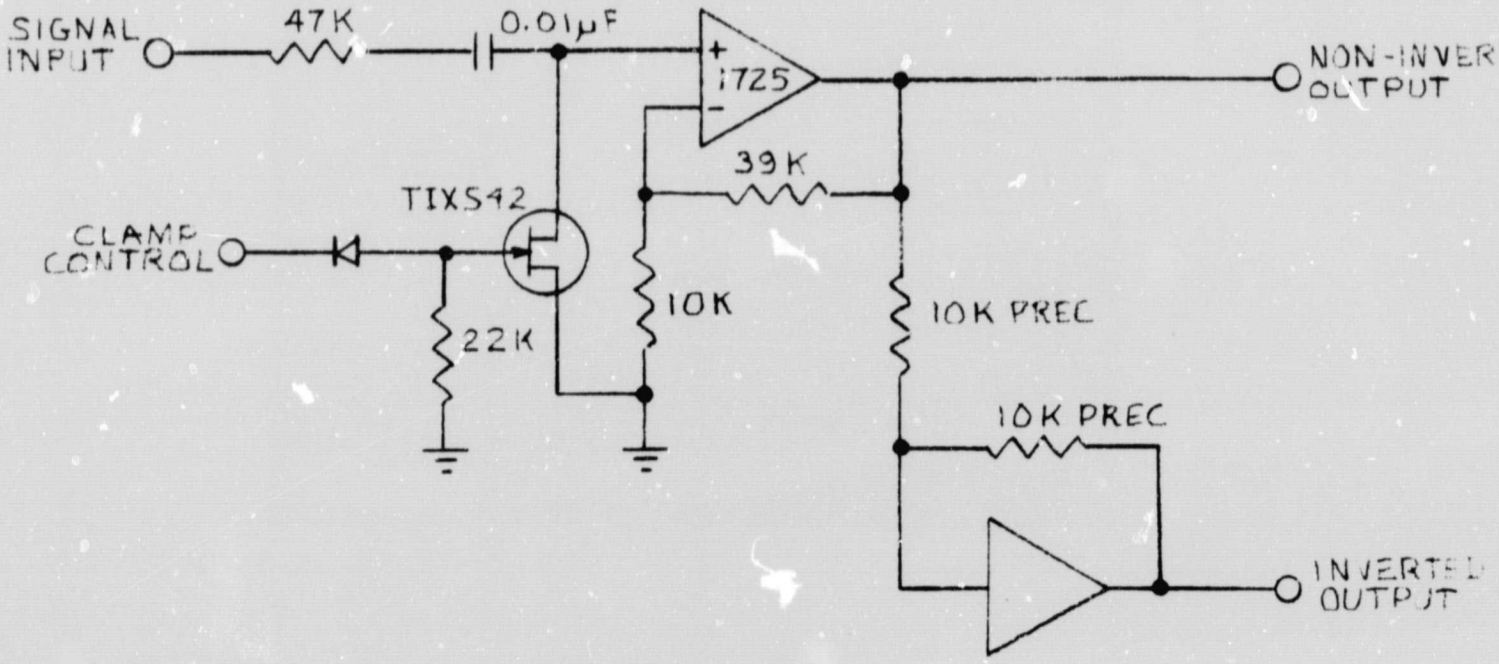

Figure 6-15. Circuit of Synchronous Clamp and Bridge Amplifier

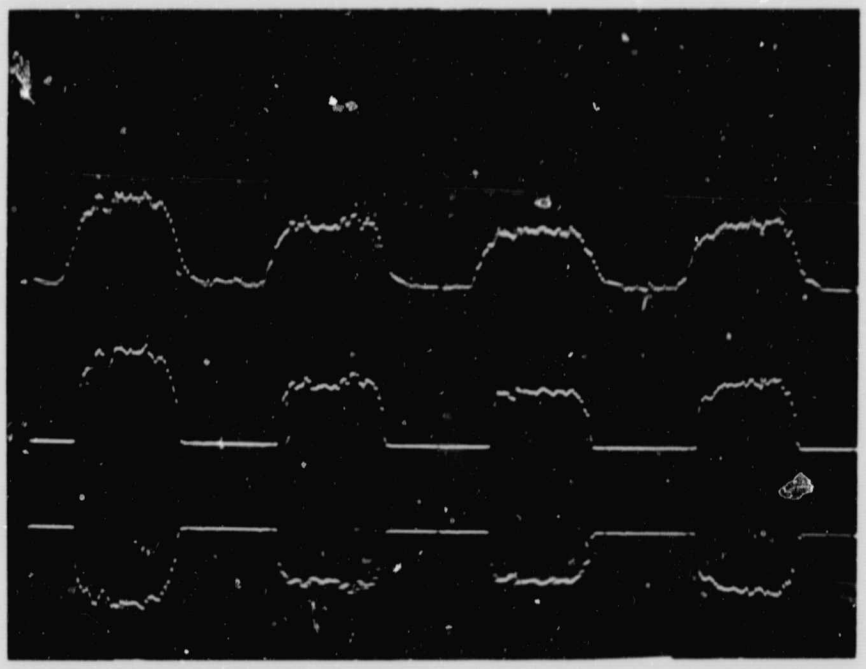

Figure 6-16. Typical Detector Waveforms: From Top to Bottom, Detector Amplifier Output, Complemental Bridge Amplifier Outputs with Zero Clamp.

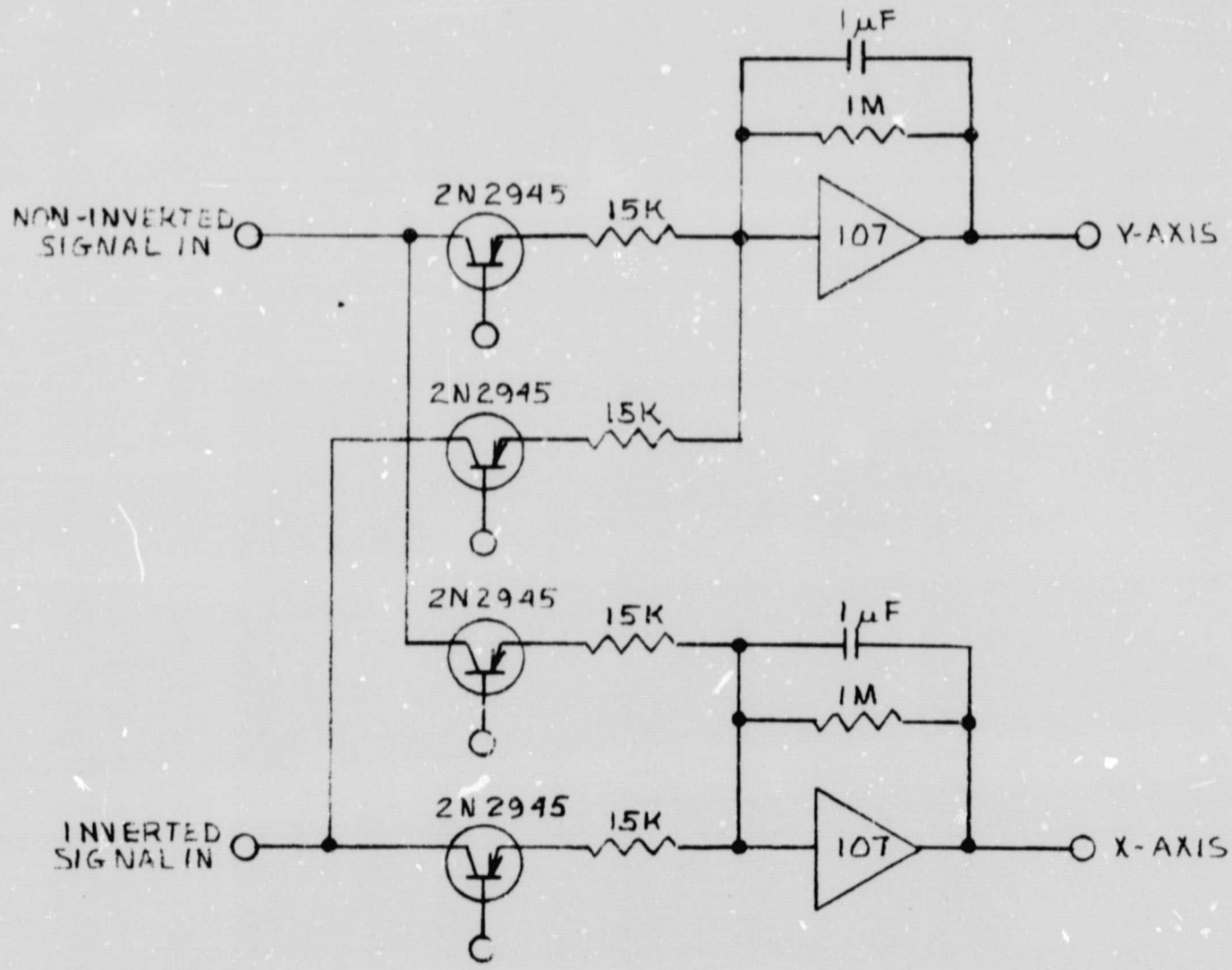

Figure 6-17. Decommutator Amplifier to Extract Error Amplitude, Sense, and Axis Information for Servo Control

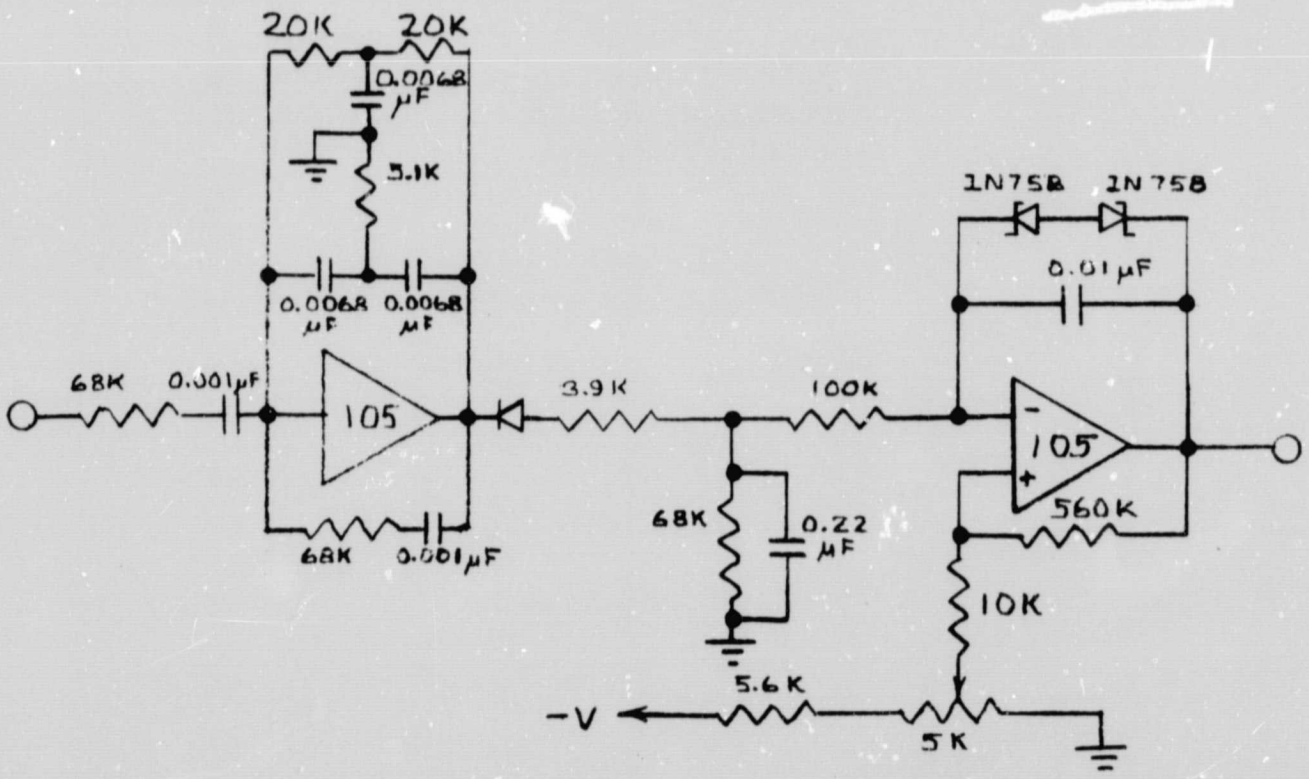

Figure 6-18. Narrow Bandpass Filter and Threshold Detector

This discriminator is shown in Figure 6-18 and consists of a narrow bandpass filter, a rectifier, and a level detector. When either the fine or coarse error sensor is functioning, the output signal from the limiter will con in a strong spectral component at 1.6 KHz. This component is identified by an operational amplifier bandpass filter with a twin-T in the feedback loop having a center frequency of 1.6 KHz and a normalized bandwidth of 0.2. The filtered signals are rectified, and applied to the operational amplifier level detector. The detector flips from one state to another only when the rectified signal exceeds a predetermined level. (The threshold level was experimentally determined so that a smooth handover is achieved among the functional modes.) The output is then fed into a logic network to generate appropriate gates for functional control of the system.

6.4 GIMBAL AND TRANSFER MIRROR SERVO SYSTEMS

The servo system of the laser telescope was designed to operate according to three different control modes. These are:

a. Manual control mode - commanded by an external synchro input.

b. Coarse-acquisition control mode - operates with gimbal rate damping.

c. Fine-guidance control mode - operates by tracking an inertial target (the beacon).

Switching among these control modes is accomplished automatically by transistor switches which are controlled by the output states of the coarse-fine discriminator described in the preceding section.

During tracking, first the manual control brings the telescope within the coarse field range. Once the image falls inside of ±1/2° field, the servo drives the telescope into the fine-guidance field. When the image lies within ± 1 arc-minute field, it allows the fine-guidance loop to capture and stabilize the telescope to keep the net position of the transfer optics at zero.

6.4.1 Manual Control Mode Servo Operation

The manual control system consists of a synchro servo, a control transmitter (CX) and a control transformer (CT). The CX is excited by 400 Hz and its secondary winding energizes the CT primary. The servo output is directly connected to the CT shaft at one of the flexure pivots of the pitch or yaw gimbal. Thus the output of the CT is proportional to the angular difference between the CX and CT. The error signal is sensed by a phase-sensitive demodulator with a low pass filter. Any differences are amplified and applied to control the servo output and drive the pitch or yaw gimbal in such a way as to reduce the difference to zero.

The analytic block diagram for manual control is shown in Figure 6-19 and is essentially identical for the pitch and yaw axes. For simplicity we ignore the effect of the load viscous damping, and the compensated open-loop transfer function is obtained by cascading the block functions, viz.,

$$G_o(s) = \frac{K_{pa} K_{ma} K_m K_s K_{fa}}{Js^2}$$

where

$K_{pa} = \frac{1+0.75s}{0.75s}$ = servo preamplifier transfer function

$K_{ma} = 20 \frac{\text{volts}}{\text{volt}}$ = servo main amplifier transfer ratio

$K_m = 0.08 \frac{\text{ft-lb}}{\text{volt}}$ = motor constant

$J = 23$ ft-lb-sec^2 = pitch axis moment of inertia ($\sim$ 19 ft-lb-sec^2 for yaw axis)

$K_s = 86 \frac{\text{volts}}{\text{rad}}$ = synchro system transfer ratio

$K_{fa} = 4 \frac{1+0.3s}{1+0.03s}$ = feedback amplifier transfer function

Therefore,

$$G_o(s) = \frac{32(1+0.75s)(1+0.3s)}{s^3(1+0.03s)}$$

The open-loop Bode asymptotic diagram is shown in Figure 6-20, which has a slope of 6 dB/oct at the crossover in the neighborhood of 1 Hz.

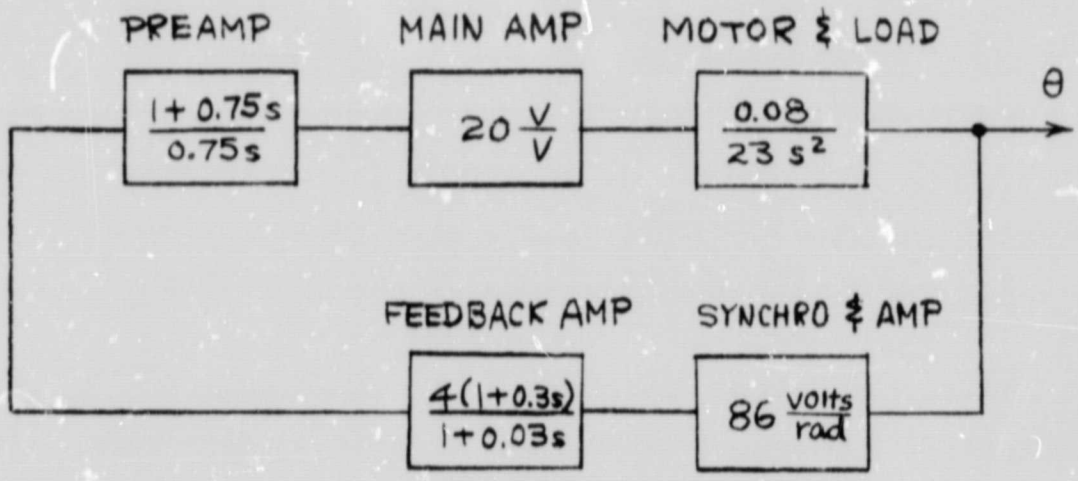

Figure 6-19. Analytic Block Diagram of Manual Control Loop

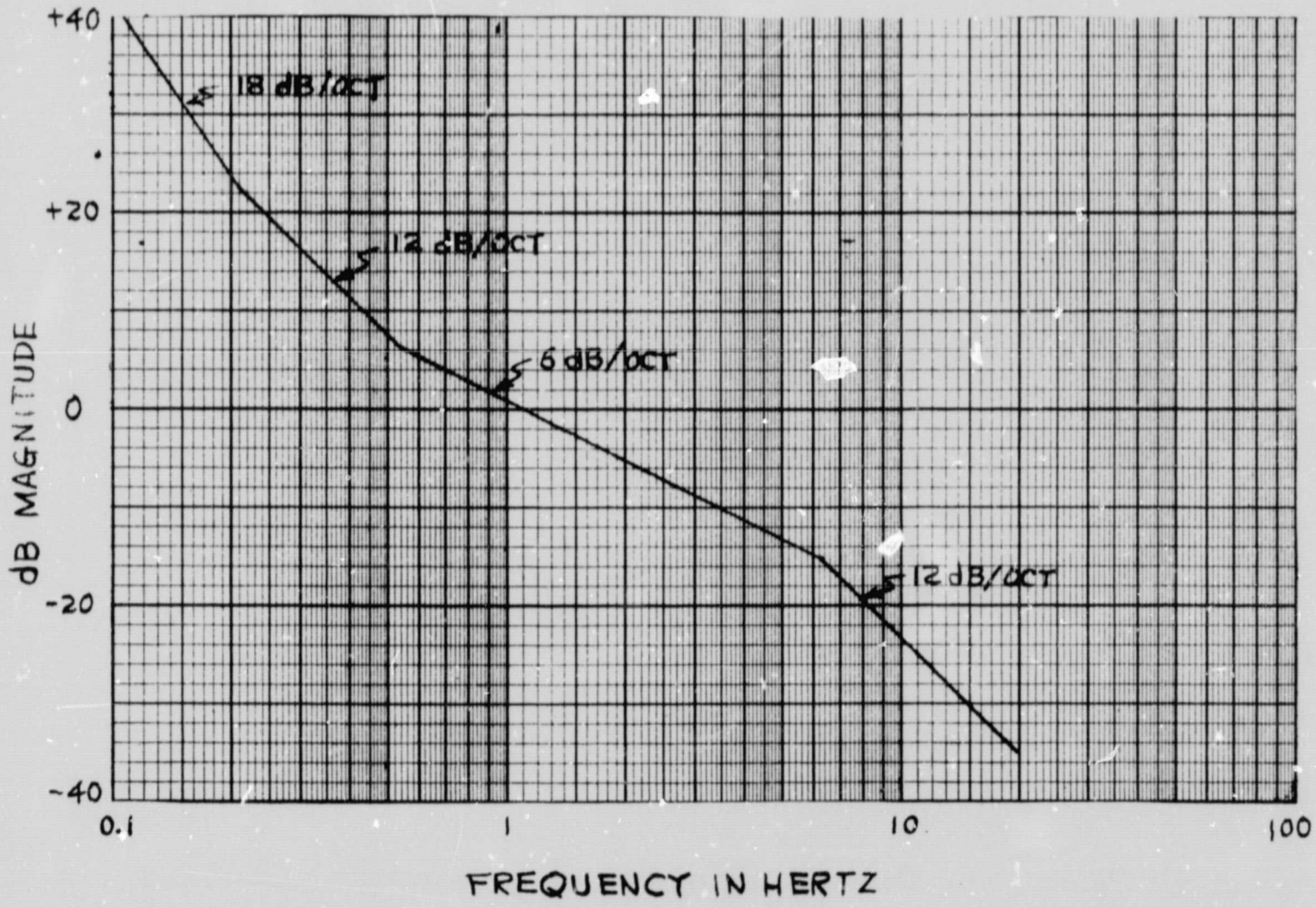

Figure 6-20. Bode Asymptotic Diagram for Compensated Open-Loop Transfer Function of Manual Control Loop

6.4.2 Coarse-Acquisition Control Mode Servo Operation

The servo must be well damped and have low angular rates during the coarse-acquisition control mode to permit subsequent capture into the limited range of the fine-guidance mode. This is accomplished by connecting a derivative network in the feedback loop of the pitch and yaw servo loops.

Figure 6-21 shows the analytic block diagram of the coarse-acquisition control system. A practical operational amplifier differentiator is featured to avoid introducing instability and noise. The desired maximum rate in the coarse-acquisition control mode is on the order of 1/15 degree per second. Assuming that the open-loop gain is sufficiently higher than unity, the closed loop expression of the coarse-acquisition control can be approximated as follows:

$$\frac{C}{R}(s) \simeq \frac{1}{K_g K_s}$$

where,

$K_g = 6.8s$ = derivative feedback loop transfer function

and

$K_s = 86 \frac{\text{volts}}{\text{rad}} = 1.5 \frac{\text{volts}}{\text{deg}}$ = synchro transfer constant.

The coarse-acquisition error signal is clipped to ±0.6 volt. The transient rate will thus be:

$$\frac{0.6(v)}{6.8(\text{sec}) \times 1.5 \left(\frac{v}{\text{deg}}\right)} \simeq \frac{1}{15} \left(\frac{\text{deg}}{\text{sec}}\right)$$

The compensated open-loop transfer function of the coarse-acquisition control loop is obtained from:

$$G_o(s) = \frac{1+0.75s}{5s} \times 20 \times \frac{0.08}{23s^2} \left(\frac{\text{ft-lb}}{v}/\text{ft-lb-sec}^2\right) \times 86 \left(\frac{v}{\text{rad}}\right) \times \frac{6.8s}{(1+0.02s)^2}$$

which yields

$$G_o(s) = \frac{8.1(1+0.75s)}{s^2(1+0.02s)^2} \simeq \frac{8.1(1+0.75s)}{s^2}$$

The bode asymptotic plot of the compensated system is shown in Figure 6-22.

6.4.3 Fine-Guidance Control Mode Servo

The pitch and yaw axes move to keep the average position of the transfer mirror servo drive at the center (or zero) of its range. In the fine guidance control mode, the input to these loops comes from the position of the transfer mirror with respect to the principal axis of the telescope.

To determine the required amplifier gain, we may carry out the computation for the static condition. Since the nominal crossover frequency of the system is given by

$$\omega_n = \sqrt{\frac{K}{J_\ell}}$$

where

K = gain constant

$J_\ell = 23$ ft-lb-sec^2 = axis moment of inertia

$\omega_n = 12 \frac{\text{rad}}{\text{sec}}$ = nominal crossover frequency

we obtain

$$K = 3310 \frac{\text{ft-lb}}{\text{rad}}$$

If the error needs to produce 3310 ft-lb/rad with 3.3 volts per arc-minute (which is the error sensor scale factor in the signal processing network), one obtains the required preamplifier gain from the block diagram of Figure 6-23 by the expression:

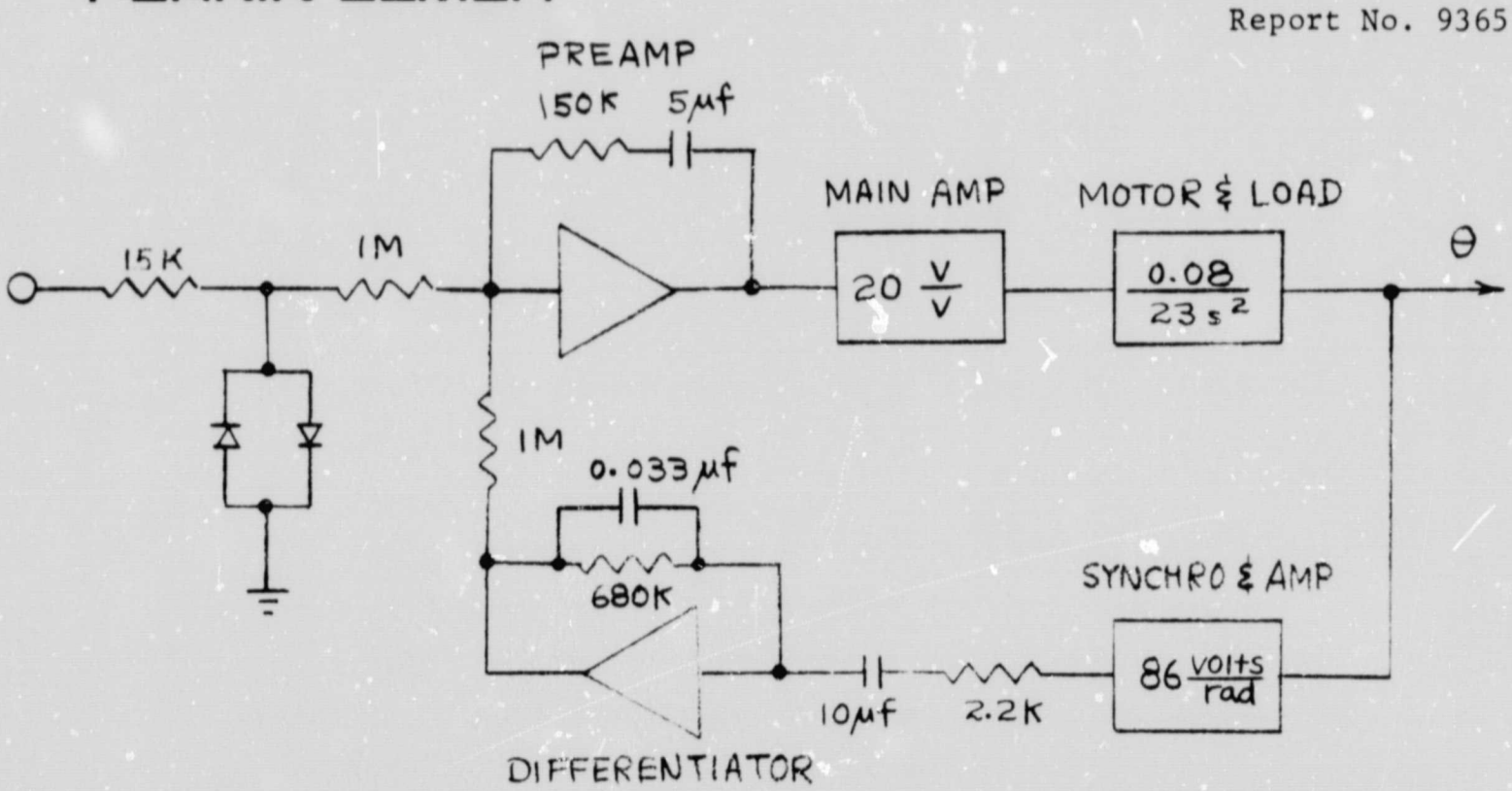

Figure 6-21. Analytical Schematic of Coarse-Acquisition Control Loop

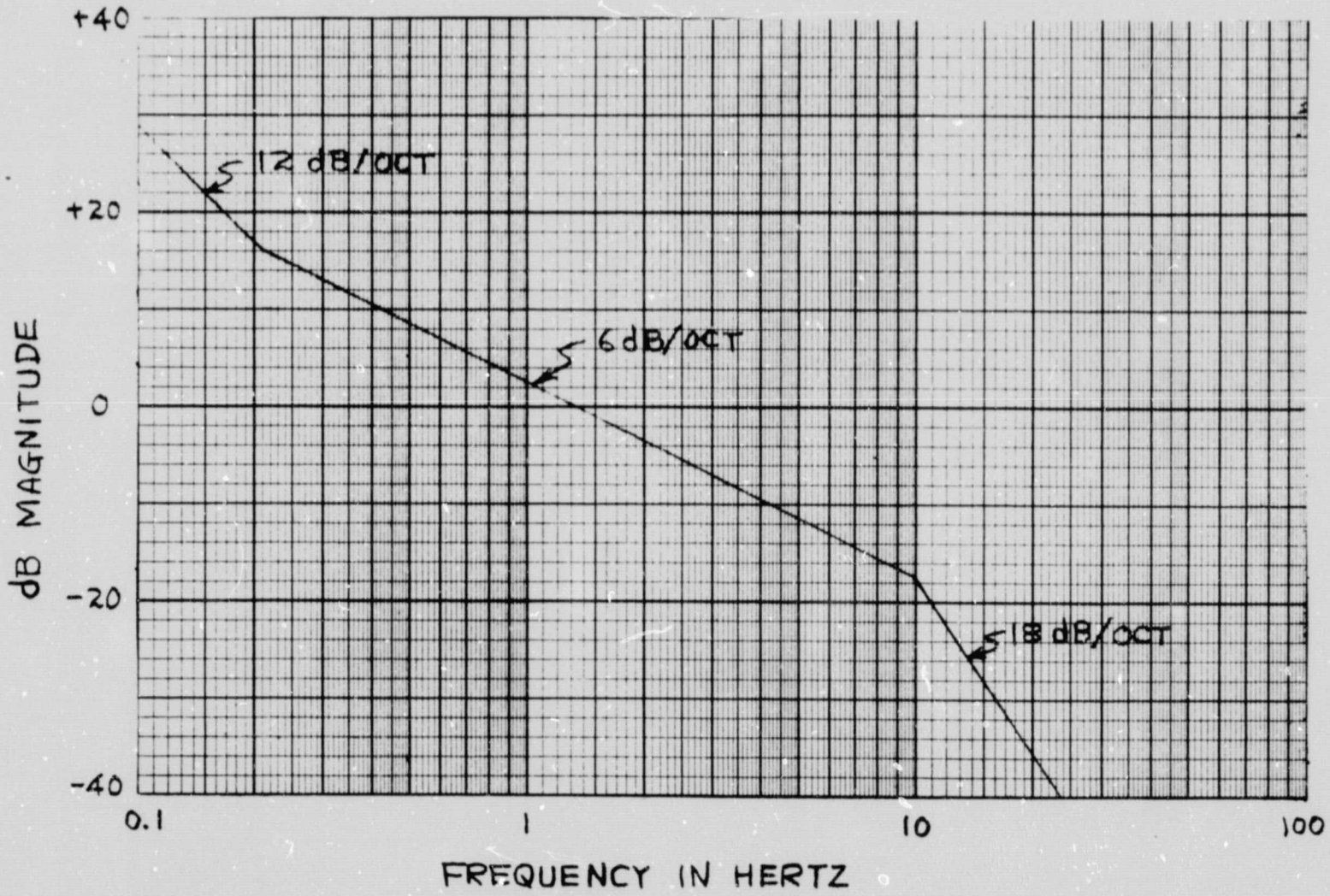

Figure 6-22. Bode Asymptotic Diagram for Compensated Open-Loop Transfer Function of Coarse-Acquisition Control Loop

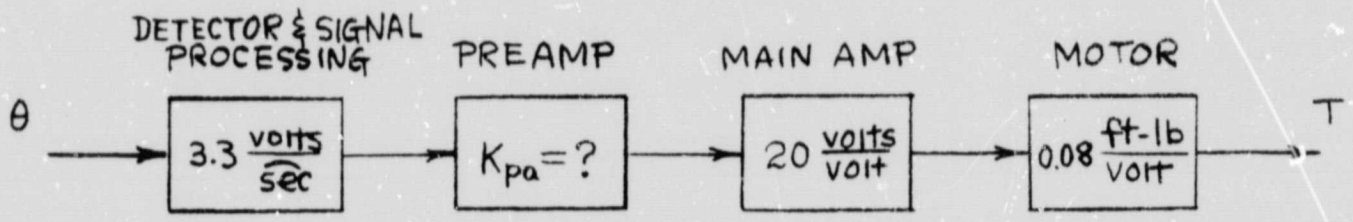

Figure 6-23. Angle-Torque Relationships for Determination of Preamplifier Gain in Fine-Guidance Control Loop

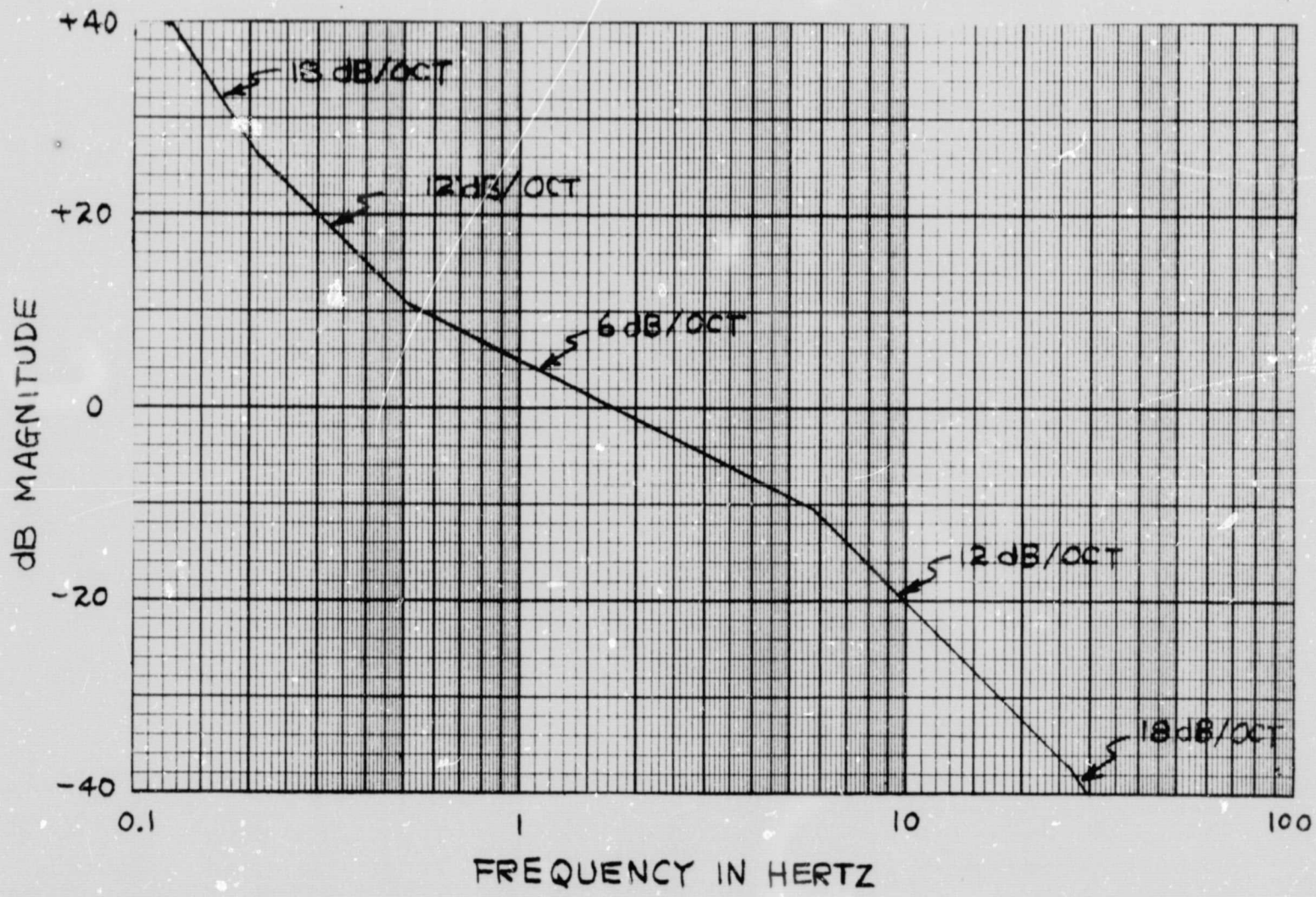

Figure 6-24. Bode Asymptotic Diagram for Compensated Open-Loop Transfer Function of Fine-Guidance Control Loop

$$3.3 \times 60 \times 57.3 \left(\frac{v}{rad}\right) \times K_{pa} \times 20 \times 0.08 \left(\frac{ft\text{-}lb}{v}\right) = 3310 \left(\frac{ft\text{-}lb}{rad}\right).$$

This leads to $K_{pa} = 0.18$.

Again for simplicity, if the transfer function of the motor including the effect of load is assumed to be $K_m/J_\ell s^2$, and if an integrater is used in the forward path to ensure high gain at low frequency, the uncompensated gain asymptote will have an 18 dB/oct slope. In order to provide adequate margins in the vicinity of ω = 12 rad/sec for stability, a log-lead compensation network is added. Cascading the error sensor scale factor, the servo amplifier gain, the torque motor transfer function, and the compensation function, we obtain the compensated open-loop transfer function as:

$$G_o(s) = \frac{47(1+0.75s)(1+0.3s)}{s^3(1+0.027s)(1+0.006s)}$$

The compensated Bode plot has a slope of 6 dB/oct at the crossover frequency of 2 Hz as shown in Figure 6-24.

The overall circuit schematic diagram for the pitch axis servo is shown in Figure 6-25, and that for the yaw axis servo is not shown since it is essentially the same.

6.4.4 Transfer Mirror Servo Drive

The Bimorph elements which support the transfer mirror are driven by a pair of high voltage operational amplifiers. The Bimorph load is highly capacitive, so a current limiting resistor is needed in series with the amplifier forward path as shown in Figure 6-26 to prevent excessive current flow. A capacitor C, is added across the input and output points of the operational amplifier to avoid instability.

The transfer function of this amplifier can be expressed as

$$\frac{E_o}{E_i}(s) = -\frac{R_2}{R_1} \frac{1}{sC(R_2+R_3)\left(1+\frac{sR_2R_3C_o}{R_2+R_3}\right)+1}$$

$$= -\frac{1}{C\,C_o R_1 R_3\left(s^2+s\,\frac{R_2+R_3}{C_o R_2 R_3}+\frac{1}{C\,C_o R_2 R_3}\right)}$$

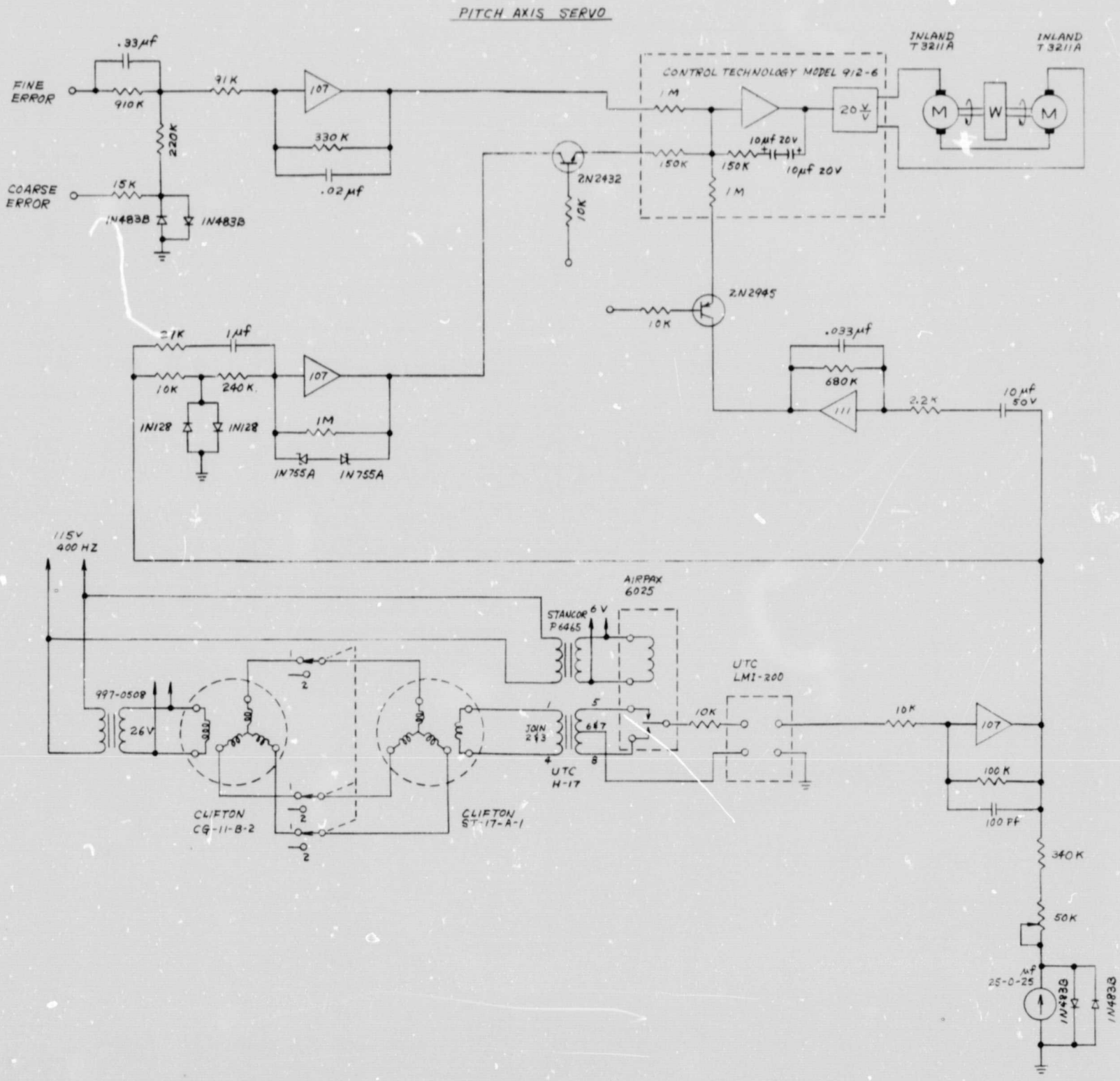

Figure 6-25. Pitch Axis Servo Circuit Schematic.

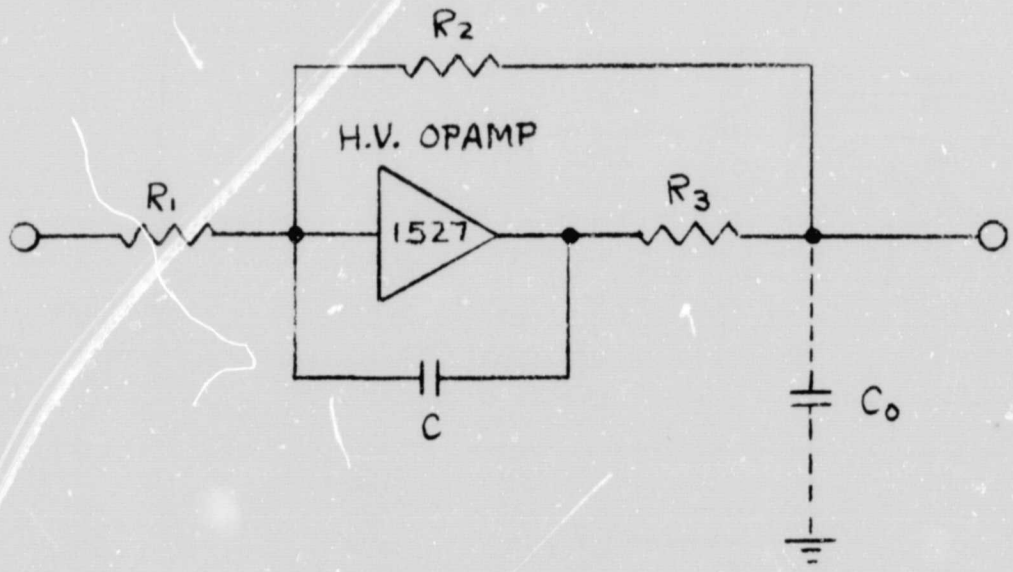

Figure 6-26. Simplified Diagram of Transfer Mirror Drive Amplifier

Therefore

$$\omega_n = \sqrt{\frac{1}{C\, C_o R_2 R_3}} = \text{undamped natural frequency}$$

and

$$\zeta = \frac{R_2+R_3}{2} \sqrt{\frac{C}{C_o R_2 R_3}} = \text{damping ratio}$$

For $\zeta = 1$, one obtains

$$C = \frac{4\, C_o R_2 R_3}{(R_2+R_3)^2} .$$

Substituting the actual values, R_2 = 330 K, R_3 = 10 K, and C_o = 0.03 μF (including cable and piezoelectric capacity), we obtain C = 0.0034 μF. The natural frequency of the circuit is approximately 1 KHz, so that it does not introduce appreciable lag in the transfer mirror loop.

The transfer mirror loop may be treated as a Type-0 servomechanism. The gain constant is selected to be about 50 dB. Since the gain may vary with telescope focus, a single lag stabilization network is used which attenuates the gain by 6 dB/oct before any remaining lag becomes effective. Since the transfer mirror mechanical assembly has a resonance frequency of about 100 Hz, a crossover frequency of 40 Hz was selected to ensure a sufficient margin against oscillation.

The transfer function of the transfer mirror loop can be expressed as

$$G_o(s) = K_{tm} K_{mp} K_{sa} K_{md} \frac{1}{1+s\tau_1} \frac{1}{1+s\tau_2}$$

where

K_{tm} = 0.6 arc-sec/volt = transfer mirror sensitivity

K_{mp} = $\frac{1}{6}$ volt/arc-sec = QMP-detector amplifier transfer ratio

K_{sa} = 82 volts/volt = decommutator and amplifier constant

K_{md} = 33 volts/volt = mirror drive amplifier constant

The time constant τ_1 is determined by the RC feedback network in the detector amplifier, which may be ignored except when operating with extremely weak signals. To avoid this additional lag in the forward loop, a 10-megohm resistor is added across the feedback photoresistor element.

The time constant of τ_2 = 1 second is used so that the crossover occurs at about 40 Hz with a nominal gain constant factor of 270.

The triangular and step responses of the transfer mirror servo have been measured and the test results are shown in Figure 6-27.

6.5 AZIMUTH AND ROLL SERVO

As mentioned previously, the basic function of the azimuth and roll axes is to facilitate testing the gimballed laser telescope in the presence of simulated spacecraft disturbances. The servo design of these axes is as follows:

6.5.1 Azimuth Axis Servo

The azimuth servo loop uses tachometer-stabilized, position-follower feedback with a direct-drive torque motor as the actuator. The requirement for the azimuth servo is to track an input angle at a uniform rate of 1 degree per second with a permissible tracking error of 0.1 degree; thus, a velocity constant of K_v = 10 rad/sec is required. To be conservative, K_v = 20 rad/sec was chosen for the design.

Figure 6-28 shows the basic configuration of the azimuth loop. The tachometer feedback inner loop is chosen with a velocity constant of 20 rad/sec. Since the moment of inertia of the azimuth gimbal is 31 ft-lb-sec^2, the equivalent damping is 620 ft-lb-sec. The required preamplifier gain, K_{pa}, in the servo amplifier is determined from the equation

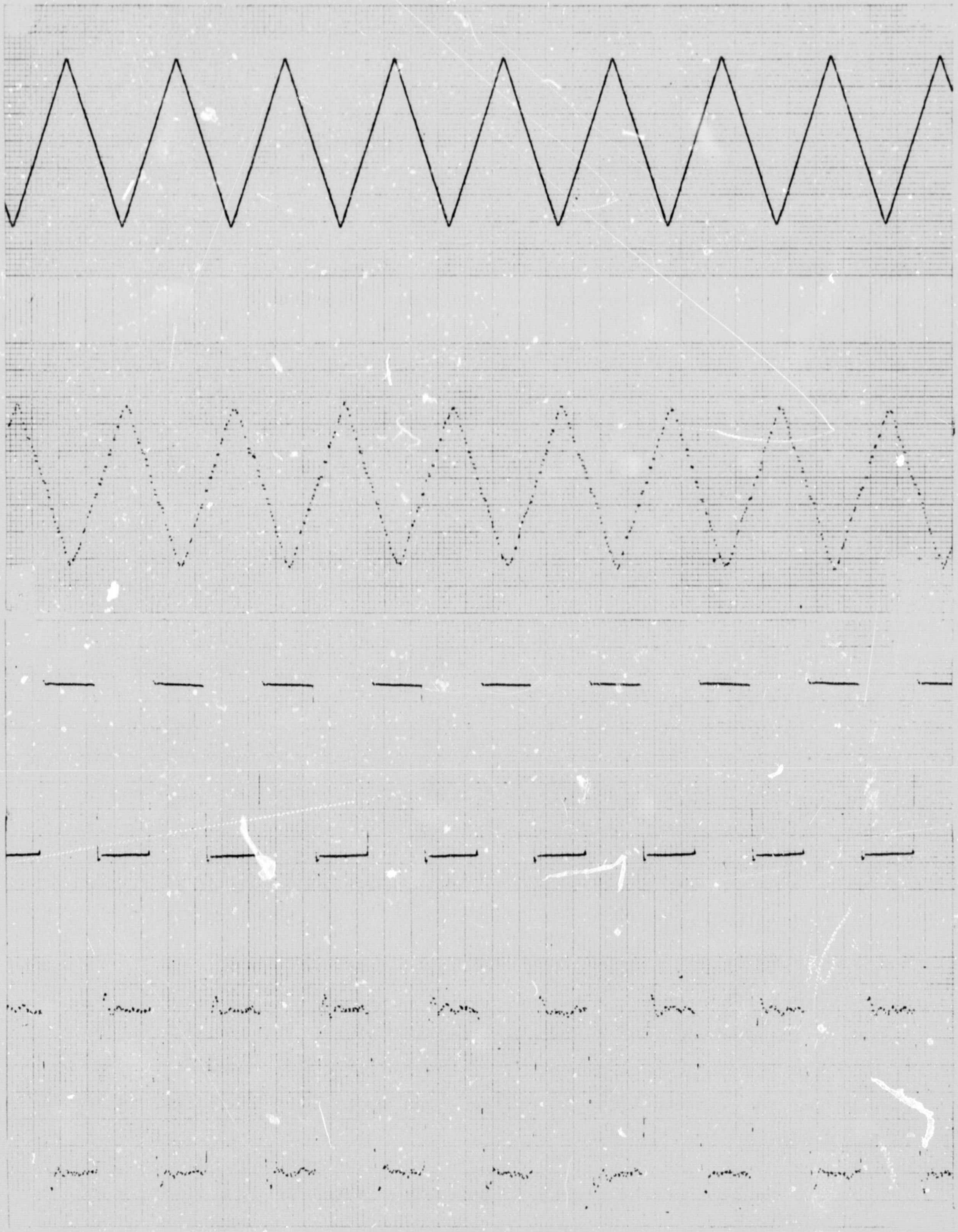

Figure 6-27. Triangular and Square Wave Responses of Transfer Mirror Servo.
Horizontal Scale: 0.1 sec/cm

$$K_{pa} K_{ma} K_m K_t = 620 \text{ ft-lb-sec}$$

where

$$K_{ma} = 20 \frac{\text{volts}}{\text{volt}} = \text{main amplifier gain}$$

$$K_m = 0.5 \frac{\text{ft-lb}}{\text{volt}} = \text{motor torque constant}$$

and

$$K_t = 10 \frac{\text{volt}}{\text{rad/sec}} = \text{tachometer constant,}$$

leading to $K_{pa} = 6.2$.

To determine the error amplifier gain, K_{sa}, the basic equation for gain constant equilibrium can be used, viz.,

$$K_{sa} K_{fb} K_t^{-1} = 20 \text{ rad/sec}$$

where

K_{fb} = 52 volts/rad = potentiometer constant.

Therefore,

K_{sa} = 3.85. The system stiffness is thus 52x3.85x62, or approximately 12,400 ft-lb/rad.

In order to stabilize the system under closed loop conditions, a lag compensator with a ratio of 5 is chosen. The compensated curve has a slope of 6 dB/oct at the crossover frequency of 4 rad/sec. The compensated asymptote is shown in Figure 6-29.

6.5.2 Roll Axis Servo

The basic design of the roll axis servo is essentially the same as that of the azimuth axis. The 25 ft-lb-sec^2 load inertia of the roll axis is driven by the servo motors through a stepdown ratio of 16:1 from motor to load by the friction wheel drive. The required velocity constant is the same as for the azimuth axis, 10 rad/sec, and again K_v = 20 rad/sec is chosen in the design.

Because of the higher friction (estimated as approximately 12 ft-lb), and lower inertia compared to the azimuth axis, a higher inner loop

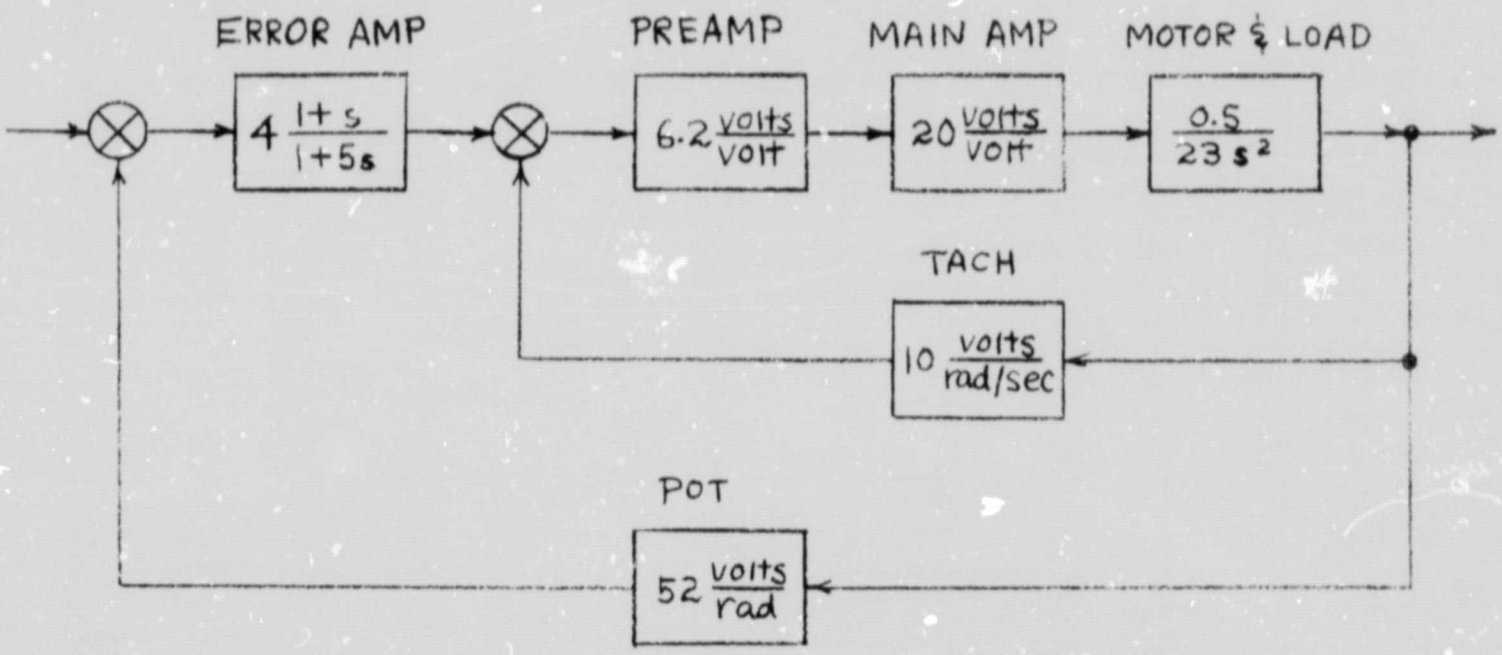

Figure 6-28. Block Diagram of Azimuth Servo Loop

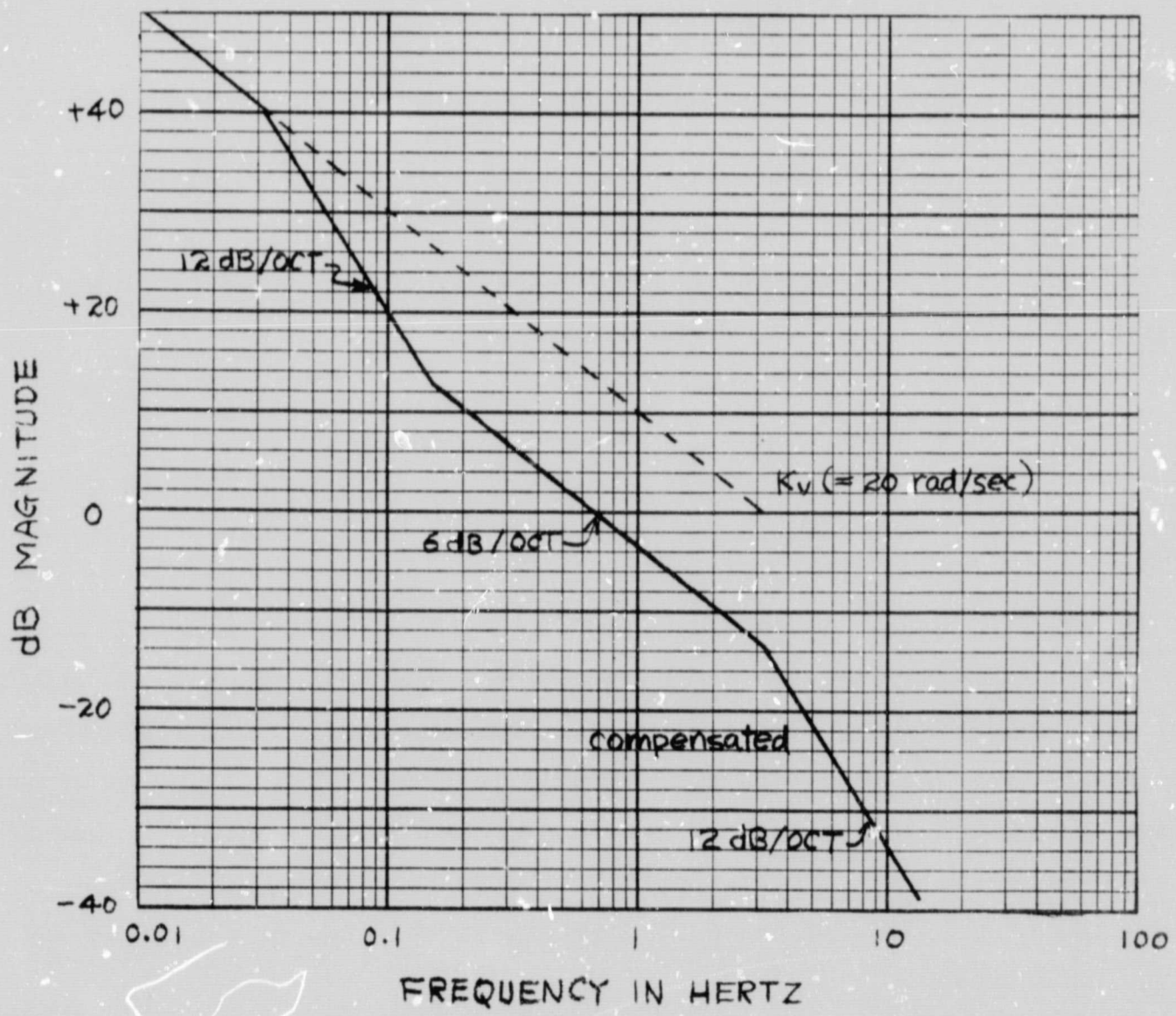

Figure 6-29. Bode Asymptotic Diagram for Compensated Open-Loop Transfer Function of Azimuth Servo Loop

gain is chosen with a velocity constant of 30 rad/sec. The load inertia reflected to the motor is $(1/16)^2$ x 25, or 0.098 ft-lb-sec^2 and the required damping in the minor loop is 0.098 x 30, or 2.94 ft-lb-sec. The required preamplifier gain is determined by

$$K_{pa} K_{ma} K_m K_t = 2.94 \text{ ft-lb-sec}$$

where

$$K_{ma} = 20 \frac{\text{volts}}{\text{volt}} = \text{main amplifier gain}$$

$$K_m = 0.12 \frac{\text{ft-lb}}{\text{volt}} = \text{motor torque constant}$$

and

$$K_t = 1.05 \frac{\text{volts}}{\text{rad/sec}} = \text{tachometer constant}$$

Therefore,

K_{pa} = 1.18 is obtained. Rewriting

$$K_{sa} K_{fb} K_t^{-1} = 20 \text{ rad/sec},$$

solving for K_{sa}, and inserting K_{fb} = 3.3 volt/rad, and K_t, one obtains K_{sa} = 6.4. The system stiffness of the roll axis is thus 3.3 x 6.4 x 16^2 x 2.94/1.05, or approximately 16,000 ft-lb-rad. A lag compensator with a ratio of 5 is used as in the azimuth axis.

6.5.3 Circuit Schematic

The overall circuit schematic diagrams for the azimuth axis and roll axis servos are shown in Figure 6-30.

6.5.4. Experimental Performance

An effort has been made to confirm how well the azimuth axis and roll axis servos behave, step voltage inputs were applied and results were recorded by Sanborn model 320 dual channel recorder. Reproductions of recorded output are presented in Figure 6-31. The position accuracy for each axis was measured with the application of 0.03 Hz sinusoidal disturbance; accuracies of 0.04 degree and 0.05 degree were obtained from azimuth and roll, respectively.

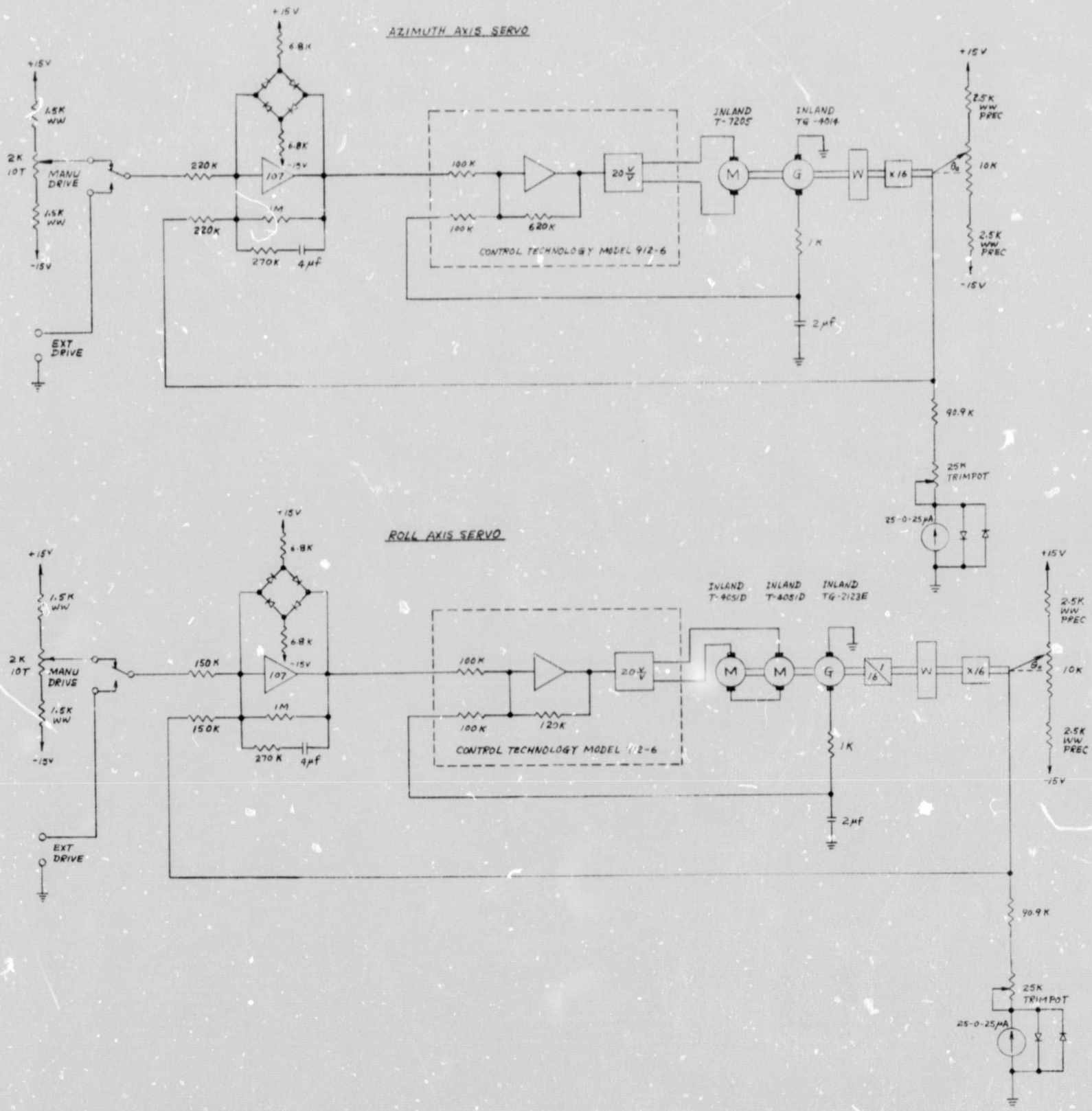

Figure 6-30. Azimuth Axis and Roll Axis Servo Circuit Schematic.

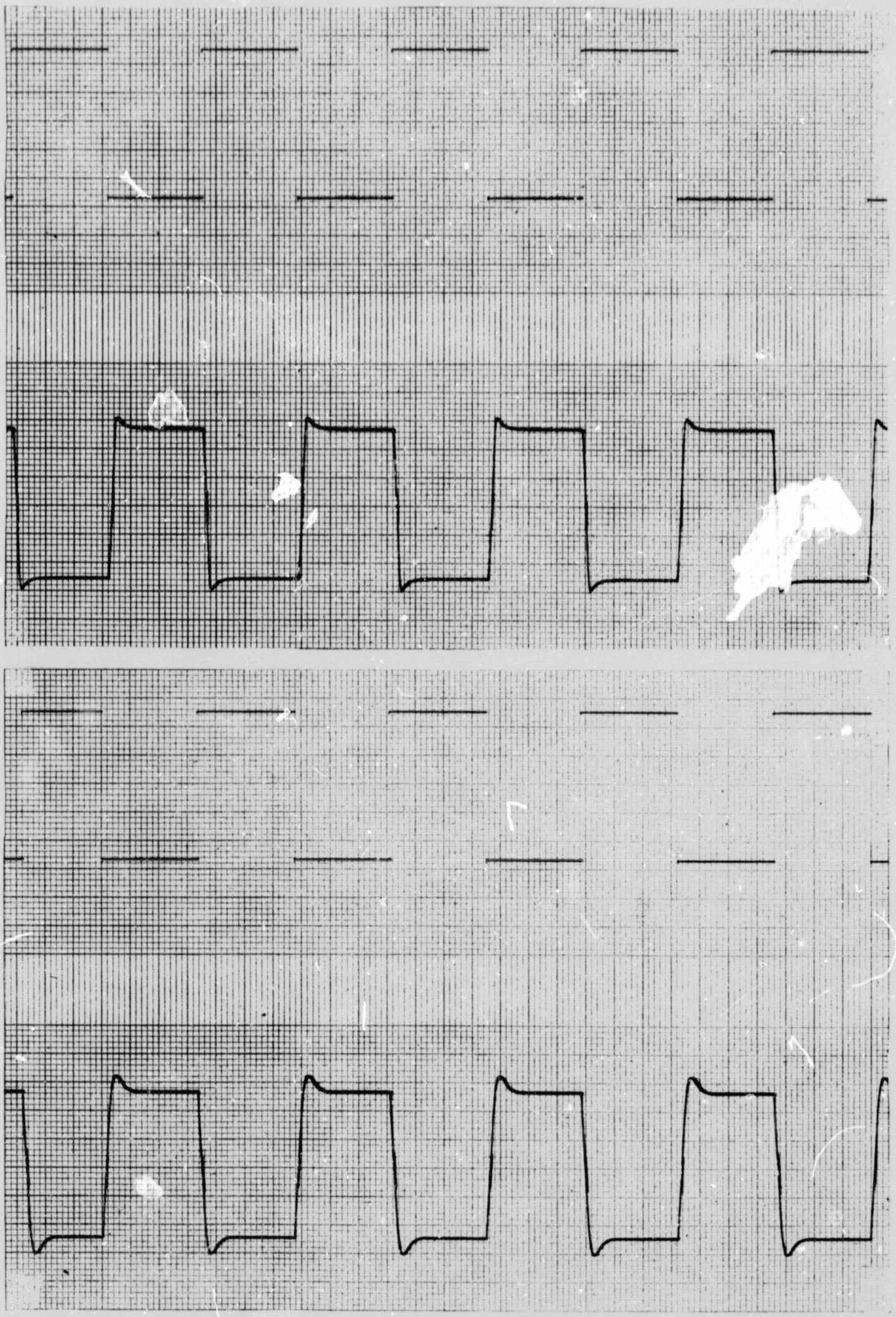

Figure 6-31. Square Wave Response, Azimuth Axis and Roll Axis Servos
Horizontal Scale: 1 sec/mm

SECTION VII

OPERATING EXPERIENCE

7.1 INTRODUCTION

As reported in the preceding section, detailed electrical measurements were taken to assess the performance of individual subsystems of the laser telescope. Here we shall briefly discuss additional observations of a more qualitative nature which were made to judge the performance of the complete system and the interactions among the various subsystems.

7.2 DESCRIPTION OF OBSERVATIONS

When the various servo loops described in Section VI were closed, it became possible to exercise the complete operational cycle of the laser telescope. The simulation equipment described in Section V was used, and a typical experiment was conducted as follows:

(a) Initially the telescope was pointed several degrees in pitch and yaw away from the beacon line of sight.

(b) The telescope was next commanded to slew toward the predicted location of the beacon.

(c) When the coarse-acquisition system picked up the beacon signal it assumed control of the pitch and yaw gimbals.

(d) The coarse-acquisition system now having control of the gimbals drove the laser telescope toward the operating field of the fine-guidance system.

(e) Hand over from coarse acquisition to fine guidance occurred and the fine-guidance system assumed control of the gimbals. The gimbals were driven in this mode to keep the transfer mirror nominally in the center of its range.

This concluded an acquisition cycle which took, on an average, between 10 and 20 seconds. The transmit laser was turned on throughout the acquisition cycle as it had little or no effect on the cycle time or performance.

The fact that fractional-arc-second-accuracy beam-pointing by the laser telescope was accomplished at the end of this cycle was displayed visually with the arrangement illustrated previously in Figure 5-2. The far field-pattern of the laser telescope was projected onto a globe of the earth as if the spacecraft-earth range were 100 million miles; i.e., to the laser telescope the globe had an apparent angular subtense of 16 arc-seconds, and the beacon appeared to originate from a specific point on the globe. When the laser-telescope had acquired and was tracking the simulated earth beacon, the central core of the Airy pattern of the transmitted beam (0.4 arc-second diameter - or 200 mile diameter on the globe) appeared almost completely stationary, and was centered on the beacon location. A photograph of this pointing performance is shown in Figure 7-1.

When spacecraft motions were simulated by producing fairly severe roll and azimuth motions with the outermost axes of the four-axis mount (typically ± 4 degrees in several seconds), the laser telescope continued to project a nearly stationary image onto the globe. As the core of the Airy pattern subtended an angle of 0.4 arc-second, and as this image moved less than 1/4 of the core diameter during this demonstration, it is evident that the system was tracking and pointing with a precision of at least 1/4 x 0.4 = 0.1 arc-second.

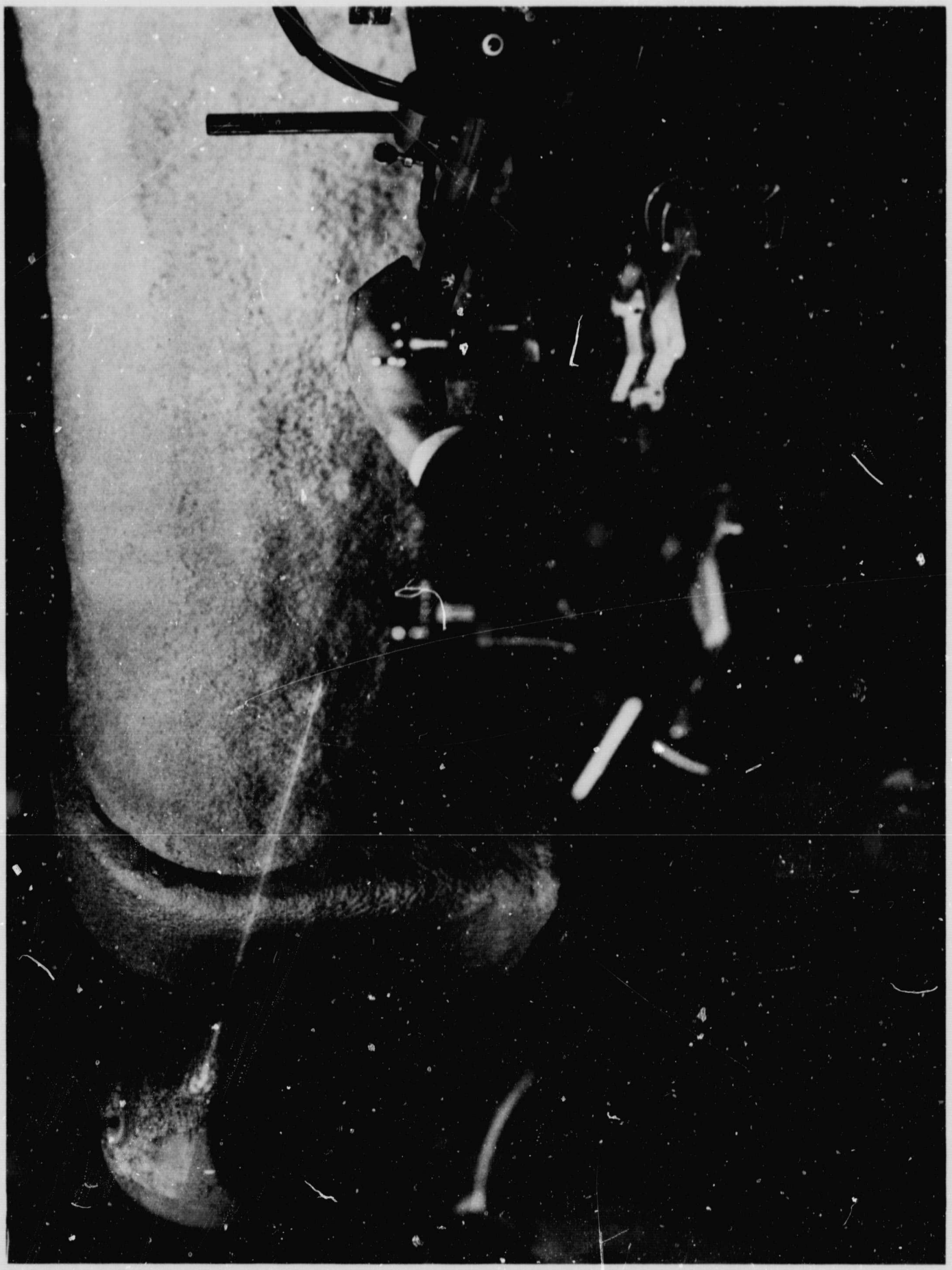

Figure 7-1. Simulation of Precision Beam Pointing from Deep Space to Earth.

SECTION VIII

DISCUSSION

This report has summarized how early concepts and development of key hardware for deep-space optical communications were refined and incorporated into a working laboratory prototype of a laser telescope for deep-space communications missions.

Proven features of the earlier breadboard hardware were retained, but important innovations were added in order to:

(a) minimize the weight of the instrumentation.

(b) package the instrumentation compactly.

(c) develop special test instrumentation by which the performance of the laser telescope can be tested via simulated space experiments.

(d) show the feasibility of adapting the system for a transmitter wavelength of 10.6 microns.

In meeting these goals a new optical design was implemented. All of the key optical components are now reflective and hence independent of operating wavelength or laser choice. Moreover, special dichroic beamsplitters were developed and incorporated which permit operating the present laser telescope at a beacon wavelength of 4880 Å and a transmitter wavelength of 6328 Å and/or 10.6 microns. As a result of the revised optical design, it was possible to develop and implement an elegant reflective version of the refractive transfer lens used previously. This new "transfer mirror" is remarkably compact and simple, yet is exceedingly powerful in terms of being responsible for the fractional arc-second pointing precision of the laser telescope. Also to help in the achievement of design goals, a new fine-guidance system was developed that combines the optical efficiency of an optical image splitter with the compactness and reliability of a quadrant multiplier phototube.

Experiments were carried out with the laser telescope to show that the system is now fully operational under conditions that validly simulate operation in space. The stage is now set to conduct a program of laboratory testing by which such space experiments as fractional arc-second tracking, point ahead, acquisition, earthshine effects, statior transfer and fading effects can all be simulated. Through such experiments, which are now underway, detailed engineering data will be gathered to help the designers of future spacecraft utilize this new communications technology.

APPENDIX A

SCATTER INVESTIGATION

Since any scattered light in the transceiver will hinder channel separation, an investigation was undertaken to determine the factors contributing to scattered light and ways to reduce their effect.[1]

Many sources of scatter were investigated and hundreds of samples were examined. Quantitative measurements of the percentage of incident light scattered in reflection from a sample were made on an instrument designed and built at Perkin-Elmer by Dr. H. Polster and Mr. J. Douglas. The instrument, seen in Figure A-1, utilizes a two-beam configuration in which the output of a laser is chopped into a sample beam and a reference beam. The sample beam is normally incident on the piece to be measured and any light scattered back from the piece will be collected by an integrating sphere. The reference beam is directly incident on the wall of the sphere after passing through variable attenuators. The measurements are taken by adjusting the reference beam intensity until the illumination in the sphere is equal to the illumination due to the scattered light from the sample. The sensitivity of the instrument is such that scatter as small as 4×10^{-6}% has been measured.

Although other schemes exist for measuring scattered light, the important thing in our study is that all samples were measured the same way and conclusions are based only on comparisons between samples. In comparing samples we found that the reflectivity of a surface has a significant effect on the scatter measurement of that surface; reflectivities had to be measured and considered in all comparisons between samples.

All optical elements scatter light but usually surfaces with multilayer dielectric coatings contribute scatter that is at least an order

---

[1] R.R. Austin, and L.P. Mott, Investigation of Low-Scatter Dichroic Beamsplitters and Their Design, J.Opt.Soc.Am., 58 736 (1968).

of magnitude larger than that due to glass alone. Our investigation was therefore concentrated on dielectric coatings.

We did, however, consider contributions to scatter due to glass elements themselves. A well polished piece of fused silica shows a scatter of only 5×10^{-5}%, an almost negligible value compared to other sources of scatter. Of course scratches, sleeks, and digs in the surface, as well as bubbles and in homogeneity in the bulk glass, will greatly increase scatter, but these are avoidable through careful selection, handling, and polishing.

Cleaning techniques, especially prior to coating, have been given much attention at Perkin-Elmer. The following is a technique that was found to leave a surface cleaner than any other technique, evaluated from a scatter measurement standpoint:

1. Ultrasonic cleaning in mild detergent
2. Hot tap water rinse
3. Methanol rinse
4. Methanol vapor degrease

We then turned to an investigation of conditions in the coating chamber as to their effect on scatter. Cleanliness of the chamber has been shown to be of prime importance in reducing scatter in the coated pieces. In a controlled experiment scatter rose from 0.14% to 0.37% in going from a clean chamber to one that had been used only two or three times. Contaminated chemicals also add to the scatter of a coating and new chemicals should be used when scatter reduction is important. The use of a shutter can help control scatter in two ways; the evaporation rate may be stabilized and impurities in the chemicals may be purged before the substrate is exposed.

In considering coating procedures, we found that high evaporation rates were the biggest contributor to scatter. When we coated some samples at various rates the scatter declined from 0.32% to 0.18% in changing the rate so that the same coating was deposited in 3 minutes instead of a half minute.

As a coating run proceeds, the temperature of the substrate rises and the evaporation rate must be raised to maintain the same deposition rate; this rate increase also causes scatter to increase. For slow evaporation rates, the powder form of the chemicals seem to perform as well as the chunk form. This of course assumes new uncontaminated chemicals. The use of glow discharge for coating durability and rotating tooling for vapor distribution can be included in a coating run without increasing scatter as long as cleanliness is observed.

Through systematic investigation we have produced coatings with 0.14% scatter at a reflectivity of better than 99%. Without taking the precautions outlined here, scatter could have run in excess of 2%.

The dichroic beamsplitter had to be made using a barium fluoride substrate. This material is very difficult to work down to an unblemished surface. The scatter from the substrate alone was at least an order of magnitude higher than the scatter of a fused silica piece. There seems to be no other material that we could substitute for the barium fluoride, therefore some effort will have to be invested to produce a polished surface with no sleeks.

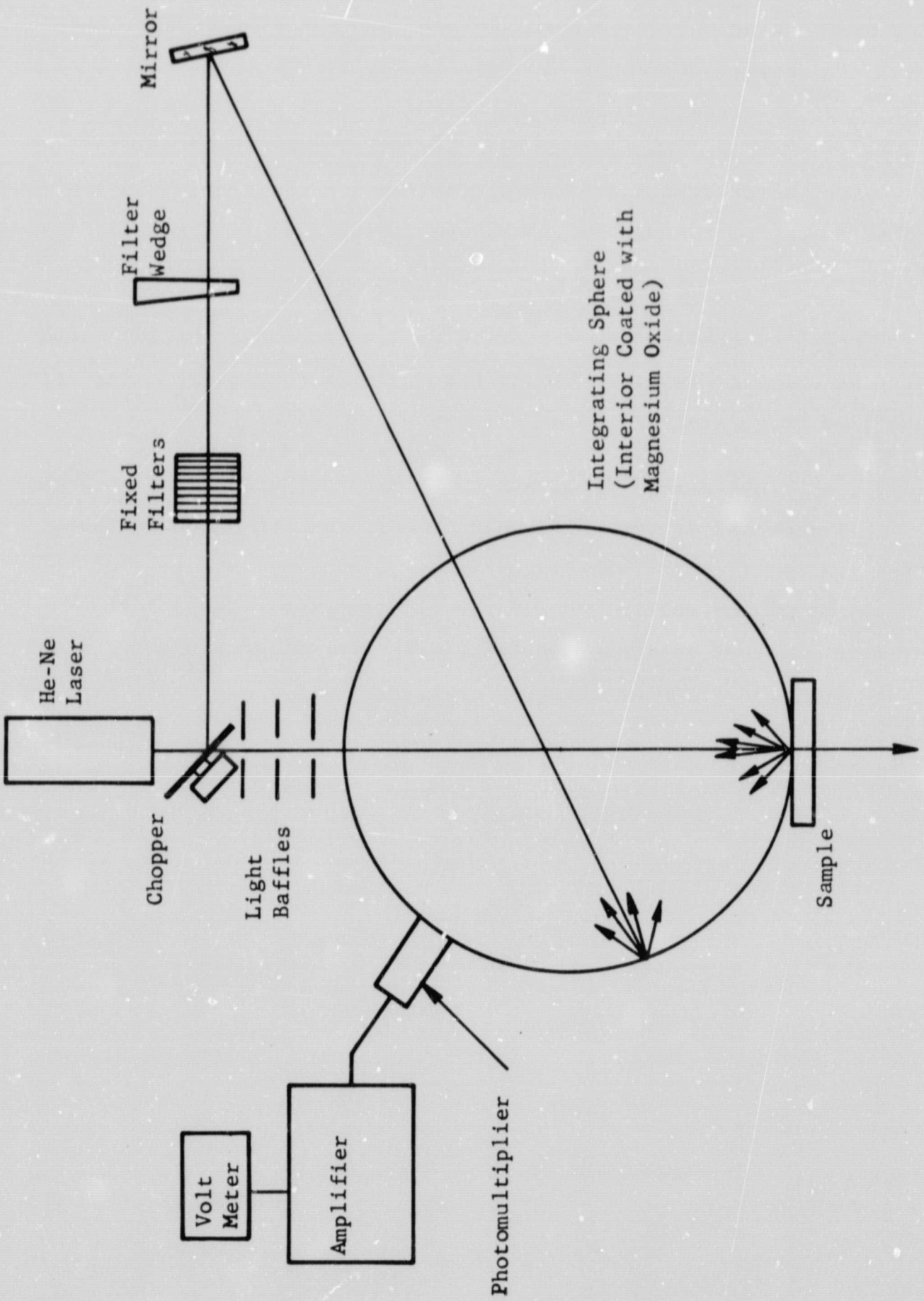

Figure A-1. Layout of Scatter Measurement Apparatus.

APPENDIX B

SUBSTRATE MATERIALS FOR INFRARED/VISIBLE
(10.6 MICRON/0.63 MICRON, 0.48 MICRON) DICHROIC BEAMSPLITTERS

The modification of the present optical fine tracking and laser transmitting system (Laser/Optics Techniques NAS 8-20115 Mod #5) to accommodate a low-power carbon dioxide (CO_2) laser transmitter (approximately 1 watt) operating at 10.6 microns, requires two dichroic beamsplitters having the following characteristics:

a) A dichroic beamsplitter capable of transmitting 10.6-micron and 0.488-micron light while reflecting 0.633-micron light.

b) A dichroic beamsplitter capable of transmitting 10.6-micron light and reflecting both 0.488- and 0.633-micron light.

Suitable designs exist for dielectric stacks to accomplish these functions but the choice of substrate material to transmit both visible and infrared radiation is limited by many factors. The main requirement is that the substrate shall not absorb significantly in the 10.6-micron channel since this will produce thermal deformation of the substrate and subsequent wavefront distortion in the visible channels (0.488 and 0.633 microns). Suitable high transmission materials in the range 0.5 to 10.6 microns are listed in Table B-I.

The Irtran materials are not satisfactory for a substrate that transmits coherent visible radiation since their polycrystalline structure results in excessive coherent scattering and wavefront degradation of visible laser beams.

TABLE B-1.*

Material	Usable Wavelength Range (Microns)
Barium Fluoride (BaF_2)	0.15 to 15
Sodium Chloride (NaCl)	0.21 to 25.0
Potassium Chloride (KCl)	0.21 to 30.0
Potassium Bromide (KBr)	0.23 to 40.0
Cesium Bromide (CsBr)	0.22 to 55.0
Cesium Iodide (CsI)	0.29 to 70.0
Irtran 3 (polycrystalline CaF_2)	0.20 to 11.5
Irtran 4 (polycrystalline ZnSe)	0.48 to 21.8

The main choice lies between barium fluoride, which has a small absorption at 10.6 microns, and sodium chloride which, is a lossless material but extremely hygroscopic. The use of a sodium chloride substrate will eliminate the problems of thermal deformation if the solubility problem can be circumvented by the use of protective coatings or by heating above ambient temperature, but it is not immediately obvious that the small absorption coefficient of BaF_2 will lead to significant wavefront distortions when transmitting a low-power 10.6-micron laser beam. As can be seen from Table B-1, BaF_2 possesses the highest thermal conductivity and lowest expansion coefficient of the alkali halide crystals and is two orders of magnitude less soluble than a crystal of NaCl. At wavelengths around 10.6 microns, barium fluoride has a small absorption coefficient of $0.15 cm^{-1}$ (Figures B-1 and B-2).

To estimate the effect of the absorption in a BaF_2 substrate, the temperature distribution and thermal deformation were calculated for a thin plate of BaF_2 and compared with experimentally measured deformations using a low-power 10.6-micron laser and a Fizeau interferometer.

Surface Deformation of an Absorbing Thin Plate

The calculation assumes that a small-diameter laser beam passes through a thin absorbing plate of infinite extent. Thermal equilibrium is

*Compiled from "Optical Materials for Infra-red Instrumentation", University of Michigan, Willow Run Laboratories, Ann Arbor, Michigan.

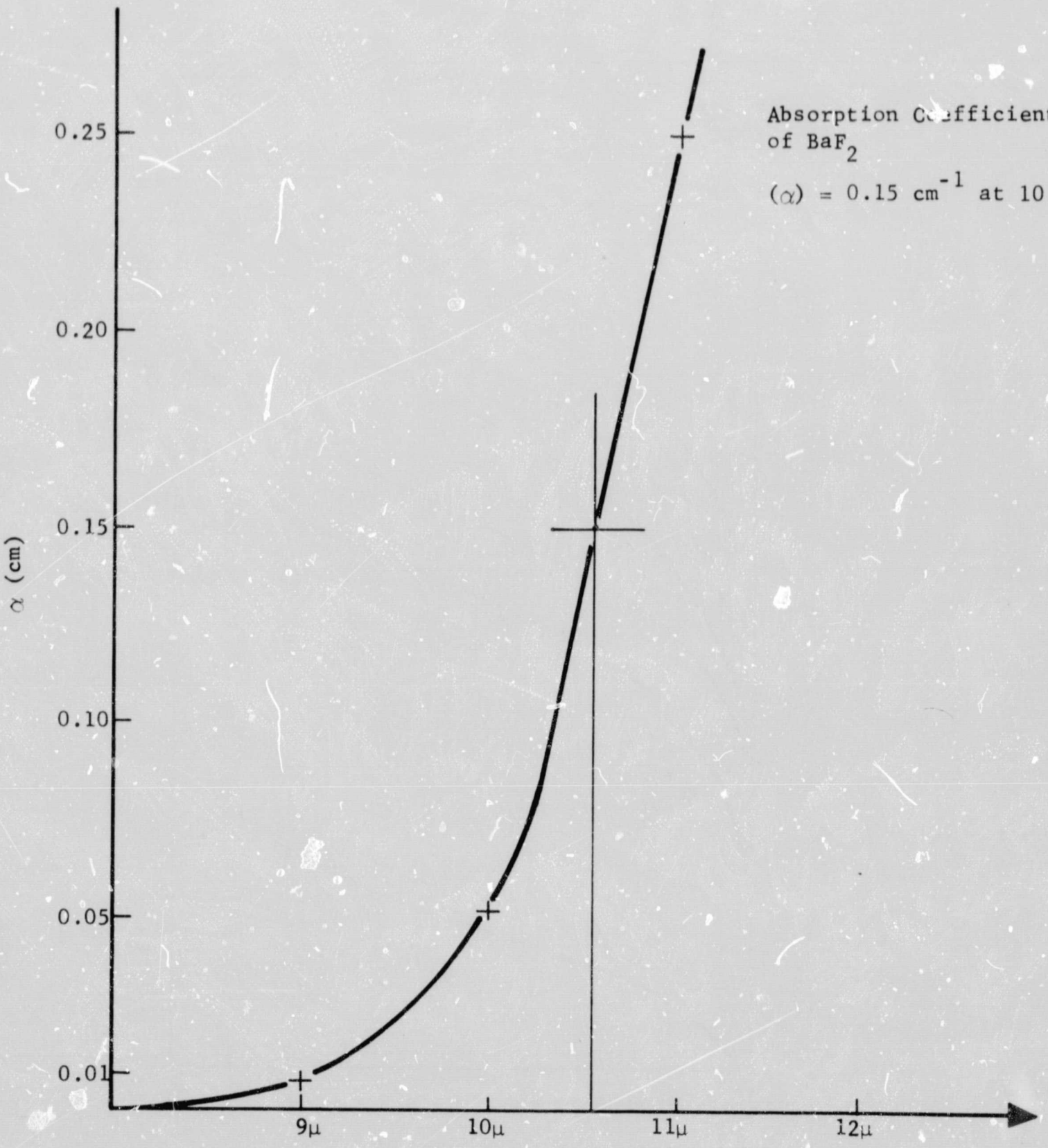

Figure B-1. Absorption Coefficient for a Selection of BaF_2 Pieces

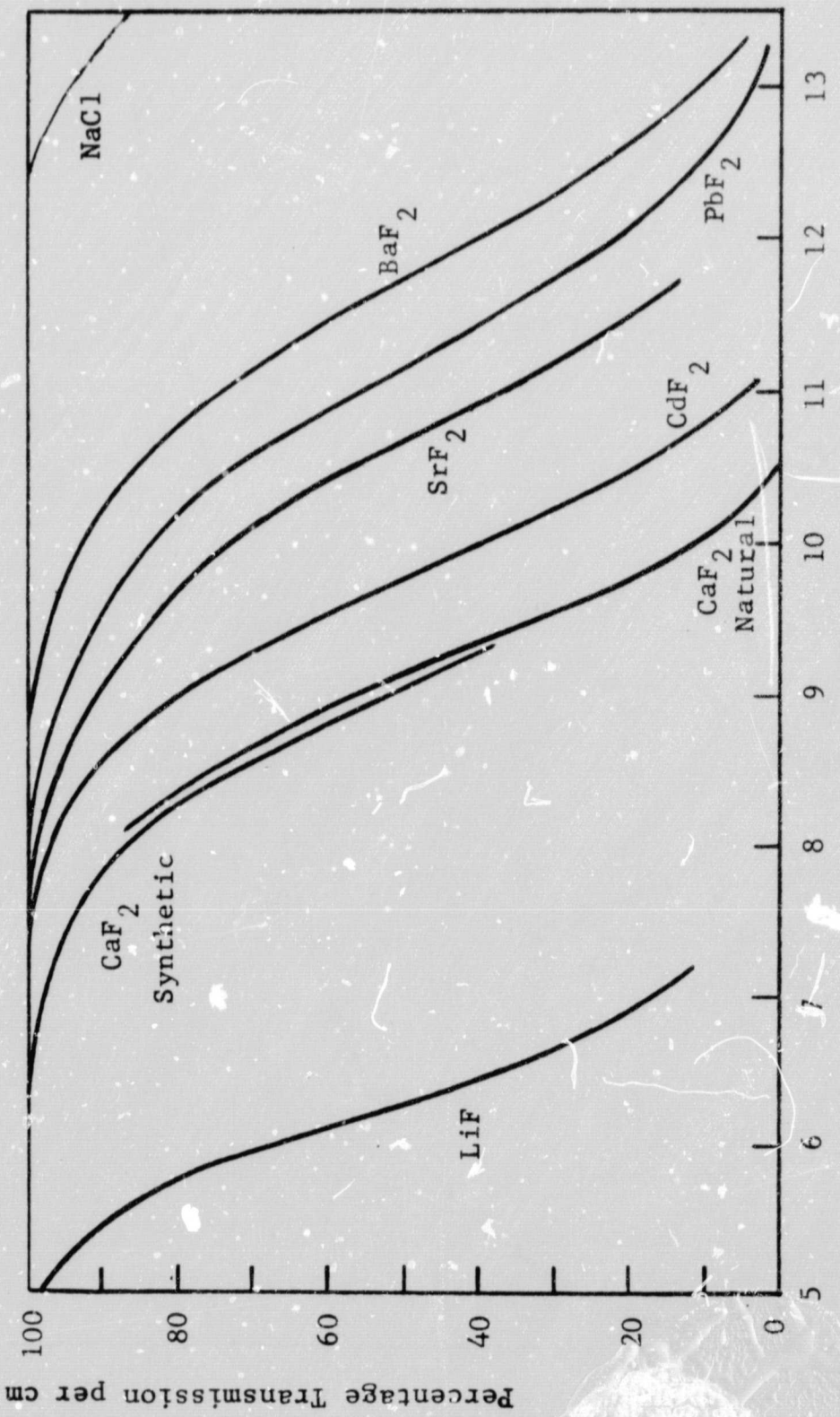

Figure B-2. Infrared Transmission of One Inch Thick Samples
(No Reflection Losses Assumed)

due only to heat conducted radially from the absorbing region, radiation and convective losses from the plate surfaces being neglected in the heat balance equation. The output intensity of a CO_2 laser can be represented by

$$I(r) = \frac{2P_o}{\pi a^2} \exp\left(-\frac{2r^2}{a^2}\right) \tag{1}$$

where,

a = radial distance at which the output falls to $e^{-2} \sim 0.1$ of the central intensity

P_o = total radiated power

r = radial distance.

The steady state heat balance equation for a cylindrical annulus can be written as

$$-KA_r \left(\frac{dT}{dr}\right)_r + I(r)2\pi r dr \alpha \ell = -KA_{r+dr} \left(\frac{dT}{dr}\right)_{r+dr} \tag{2}$$

where,

K = material thermal conductivity

α = its absorption coefficient (cm^{-1})

A_r, A_{r+dr} = cylindrical surface areas at radii r and r+dr in a plate of thickness ℓ.

The second term represents the radial distribution of heat absorbed from the laser beam. Using the mean value theorem, one can write the derivative at r+dr as

$$\left(\frac{dT}{dr}\right)_{r+dr} = \left(\frac{dT}{dr}\right)_r + \left[\frac{d}{dr}\left(\frac{dT}{dr}\right)\right]_M dr \tag{3}$$

where M is some arbitrary point between the two cylindrical surfaces. Substituting Equations (1) and (3) into Equation (2) and setting $Ar = 2\pi r\ell$, one obtains $A_{r+dr} = 2\pi(r+dr)\ell$.

When the terms of the order $(dr)^2$ are dropped, the heat balance equation becomes

$$\frac{2r\alpha P_o}{\pi a^2} \cdot \exp\left(-\frac{2r^2}{a^2}\right) + K\left[\frac{dT}{dr} + r\frac{dT}{dr^2}\right] = 0 \qquad (4)$$

Since

$$\frac{d}{dr}\left(r\frac{dT}{dr}\right) = \frac{dT}{dr} + r\frac{d^2T}{dr^2} ,$$

Equation (4) can be written as

$$\frac{2r\alpha P_o}{\pi a^2} \cdot \exp\left(-\frac{2r^2}{a^2}\right) + K\frac{d}{dr}\left(r\frac{dT}{dr}\right) = 0.$$

This can be integrated in a straightforward manner to yield

$$\frac{dT}{dr} = -\frac{1}{Kr}\frac{2P_o\alpha}{4\pi}\left(1 - \exp\left(-\frac{2r^2}{a^2}\right)\right) + \text{constant}. \qquad (5)$$

The arbitrary constant is set equal to zero to fit the boundary condition

$$\lim_{r \to o}\left(\frac{dT}{dr}\right) = 0.$$

A further integration to obtain the radial temperature distribution can be obtained by expanding the exponential term, i.e.,

$$T(r) = -\frac{1}{K}\frac{2P_o\alpha}{r\pi}\int_o^r \frac{dr}{r} + \frac{2P_o\alpha}{4\pi K}\int_o^r \frac{1}{r}\left(1 - \frac{2r^2}{a^2} + \left(\frac{2r^2}{a^2}\right)^2\frac{1}{2!} - \left(\frac{2r^2}{a^2}\right)^3\frac{1}{3!} + \ldots\right)dr$$

Since the first two integrals cancel and eliminate any problems at the origin, the radial temperature distribution can be written

$$T(r) = \frac{2P_o\alpha}{4\pi K}\int_o^r \frac{1}{r}\sum_{n=1}^{\infty}(-1)^n\left(\frac{2r^2}{a^2}\right)^2\frac{1}{n!} = \frac{2P_o\alpha}{4\pi K}\sum_{n=1}^{\infty}\int_o^r (-1)^n\frac{2^n r^{2n-1}}{n!\,a^{2n}}$$

$$= \frac{2P_o\alpha}{4\pi K}\sum_{n=1}^{\infty}(-1)^n\frac{2n}{2n\cdot n!}\left(\frac{r}{a}\right)^{2n} + \text{constant}$$

The constant can be evaluated by requiring that

$$T(r) \rightarrow T_o \text{ (ambient) for } r >> a.$$

Hence choosing a value of $r = 100a$, one obtains

$$T_o = \frac{2P_o\alpha}{4\pi K} \cdot \sum_{n=1}^{\infty} (-1)^n \frac{2^n}{2n \cdot n!} (100)^{2n} + \text{constant}$$

giving

$$T(r) = \frac{2P_o\alpha}{4\pi K} \sum_{n=1}^{\infty} (-1)^n \frac{2^n}{2n \cdot n!} \left[\left(\frac{r}{a}\right)^{2n} - (100)^{2n}\right] + T_{amb} \qquad (6)$$

The expansion of the substrate, if one assumes no radial temperature induced stresses, can then be written as

$$\ell(r) = \ell_o (1+\alpha^* T(r)) \qquad (7)$$

where α^* is the expansion coefficient of the material.

A quick estimate of the effect can be obtained without evaluating the expansion in Equation (6) by calculation of the value of the paraxial radius of curvature ($r \rightarrow o$) which is defined as

$$R_o = \lim_{r \rightarrow o} \left| \left(1 + \left(\frac{d\ell}{dr}\right)^2\right)^{3/2} \Big/ \frac{d^2\ell}{dr^2} \right|$$

The boundary condition that $\frac{dT}{dr} \rightarrow o$, i.e., $\frac{d\ell}{dr} \rightarrow o$, simplifies the problem to that of determining the value of

$$\lim_{r \rightarrow o} \left(\frac{d^2T}{dr^2}\right)$$

since the paraxial radius of curvature now becomes

$$R_o = \left| \quad \Big/ (\alpha^* \ell_o \frac{d^2T}{dr^2}) \right| .$$

From equation (5) and using L'Hopital's rule, one obtains

$$\lim_{r \to o} \left(\frac{d^2T}{dr^2} \right) = - \frac{P_o \alpha}{K\pi a^2}$$

and the paraxial radius of curvature becomes simply

$$R_o = \frac{K\pi a^2}{\alpha^* \alpha \ell_o P_o} \tag{8}$$

The surface deformation obtained from the sag formula is thus

$$\Delta Z = \frac{\alpha^* \alpha \ell_o P_o}{K\pi} \tag{9}$$

and the equivalent focal length of the substrate can be obtained from the thin lens formula.

An exact solution for the radial temperature distribution can be obtained by numerically integrating Equation 5 out to sufficiently large radii since the equation reduces to

$$\frac{dT}{dr} = - \frac{1}{Kr} \frac{2P_o \alpha}{4\pi} \text{ for } r > 3a \text{ ,} \tag{10}$$

i.e., within good approximation the radial temperature variation becomes logarithmic. Figure B-3 shows the expected radial temperature distribution for laser beams of various diameters. The expansion of one surface of the substrate can be calculated from this if one takes into account thermally induced radial stress as

$$\Delta Z = (\nu+1) \frac{\ell}{2} \alpha^* \Delta T \tag{11}$$

where ν is Poisson's ratio (approximately 0.1 to 0.3 for most glasses).

To verify this analytical model, measurements were made for a BaF_2 plate (25 mm x 5 mm thick) heated by a low-power CO_2 laser beam (1.3 watts).

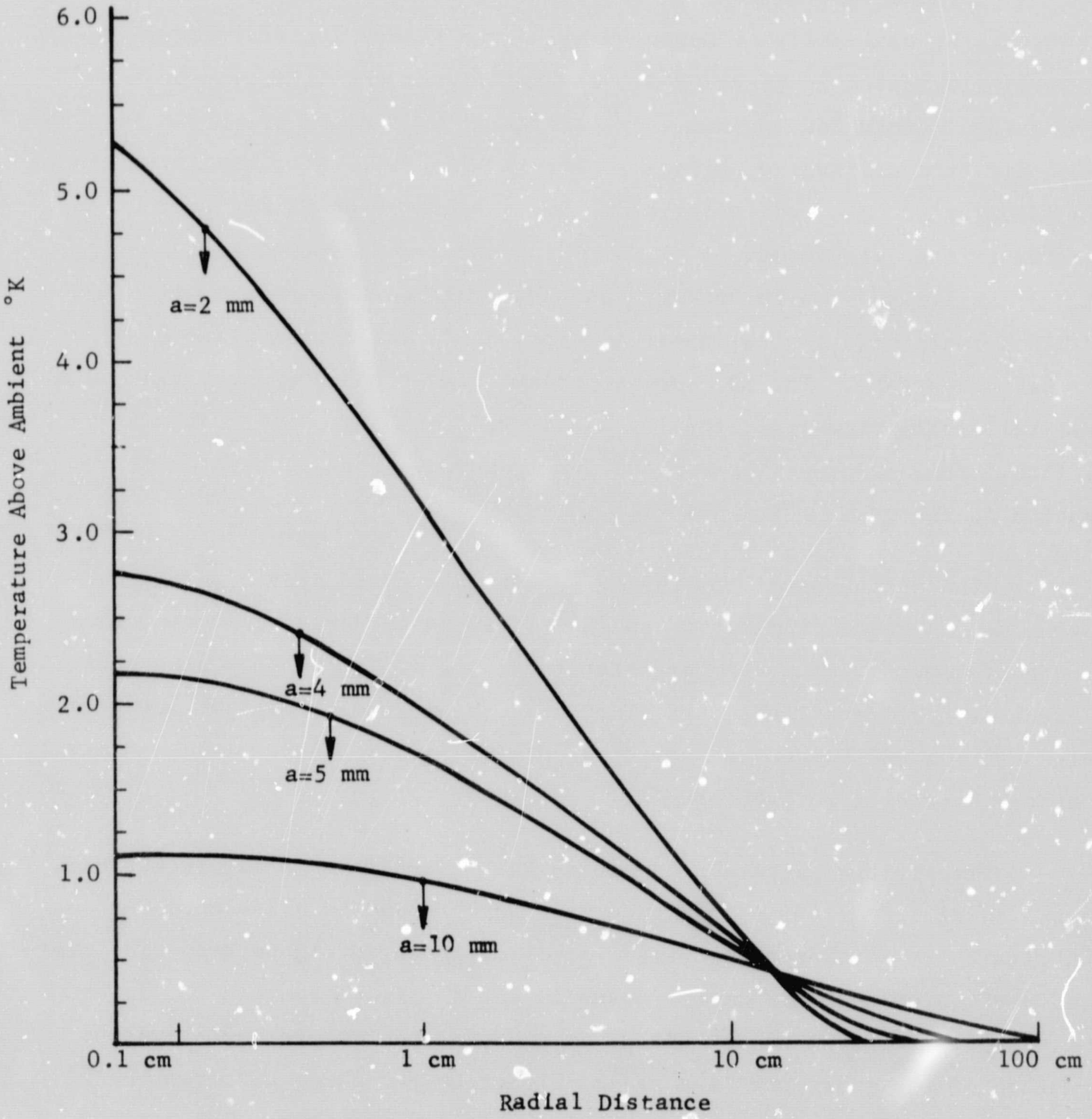

Figure B-3. Radial Temperature Distribution in a Thin Plate of BaF_2 with 1 Watt of CO_2 (Gaussian) Passing Through It. $\alpha = 0.15\ cm^{-1}$ at 10.6μ

Thermal Deformation of a BaF_2 Substrate - Experimental

Thermal deformations of the order of fractions of the wavelength of visible light can easily be measured using the Fizeau interferometer (multiple beams) illustrated in Figure B-4. The interferometer is formed by a BaF_2 substrate (A), coated for maximum reflectivity at 6328 Å and separated by a thin wedge of air from a silvered optical reference flat (B). When the interferometer is illuminated by a collimated beam from a helium-neon laser, very bright and narrow fringes are formed in transmission and are localized in the air wedge. These fringes can be observed and photographed through the mirror (C) which has a small hole in its center to allow a CO_2 laser beam to be directed at the BaF_2 substrate. The CO_2 beam is transmitted through the substrate and the red reflecting dielectric coating and is reflected from the silvered optical flat. This ensures that none of the measured deformations are due to absorption in the glass reference flat.

The output beam from the CO_2 laser is focused by a 25-cm Irtran 4 lens to allow the beam diameter in the BaF_2 flat to be varied by moving the whole interferometer. The beam diameter is estimated by the spot size charred in a piece of heat-sensitive paper (Thermofax paper) and the output power is measured using a calibrated set of thermocouples attached to a blackened metal disc at the base of a reflecting metal cone.

The fringe pattern produced in the interferometer before the BaF_2 substrate is heated is shown in Figure B-5 and that due to a 5-minute heating period with a 3-mm-diameter beam (1.3 watts) is shown in Figure B-6. The overexposed portion on the left of the frame is due to light from the CO_2 laser plasma being reflected into the camera by the mirror. Figure B-7 shows the deformation of the substrate in a radial direction for three different beam diameters as obtained from photographs of the fringe patterns. The maximum deviations for a 1-cm radius from these curves are compared with the deformations calculated from Figure B-3 and Equation 10 for a double pass through the substrate and are as follows:

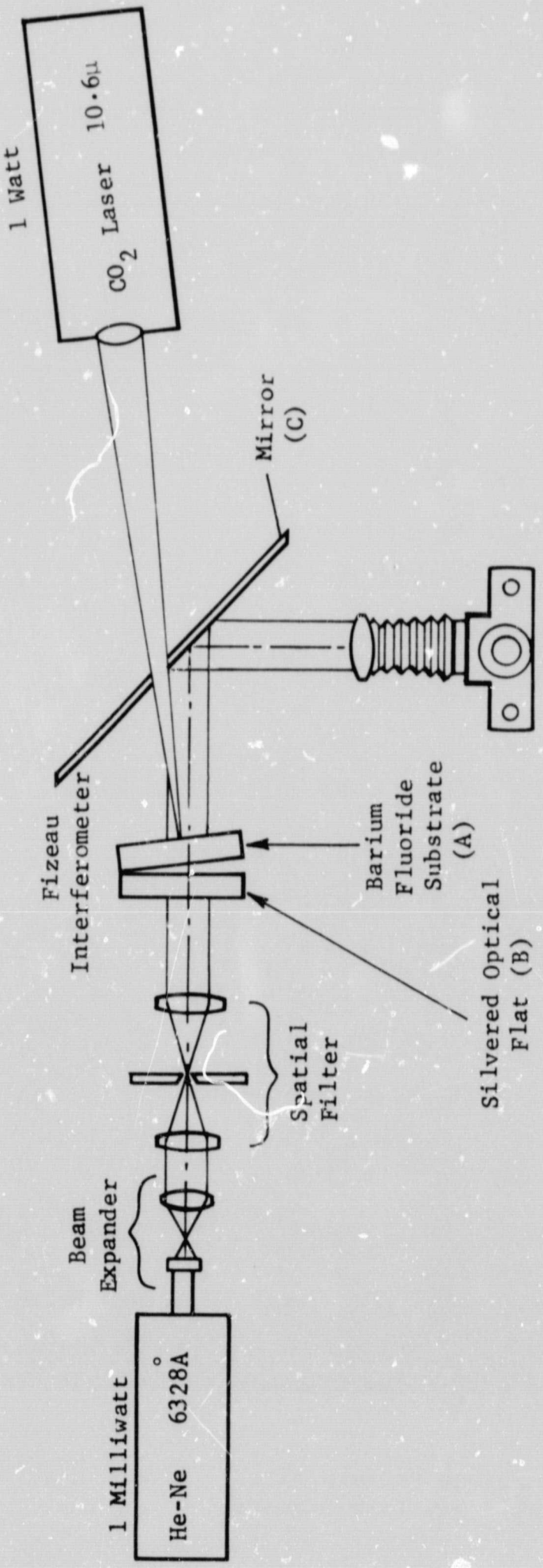

Figure B-4. Fizeau Interferometer Optical Layout

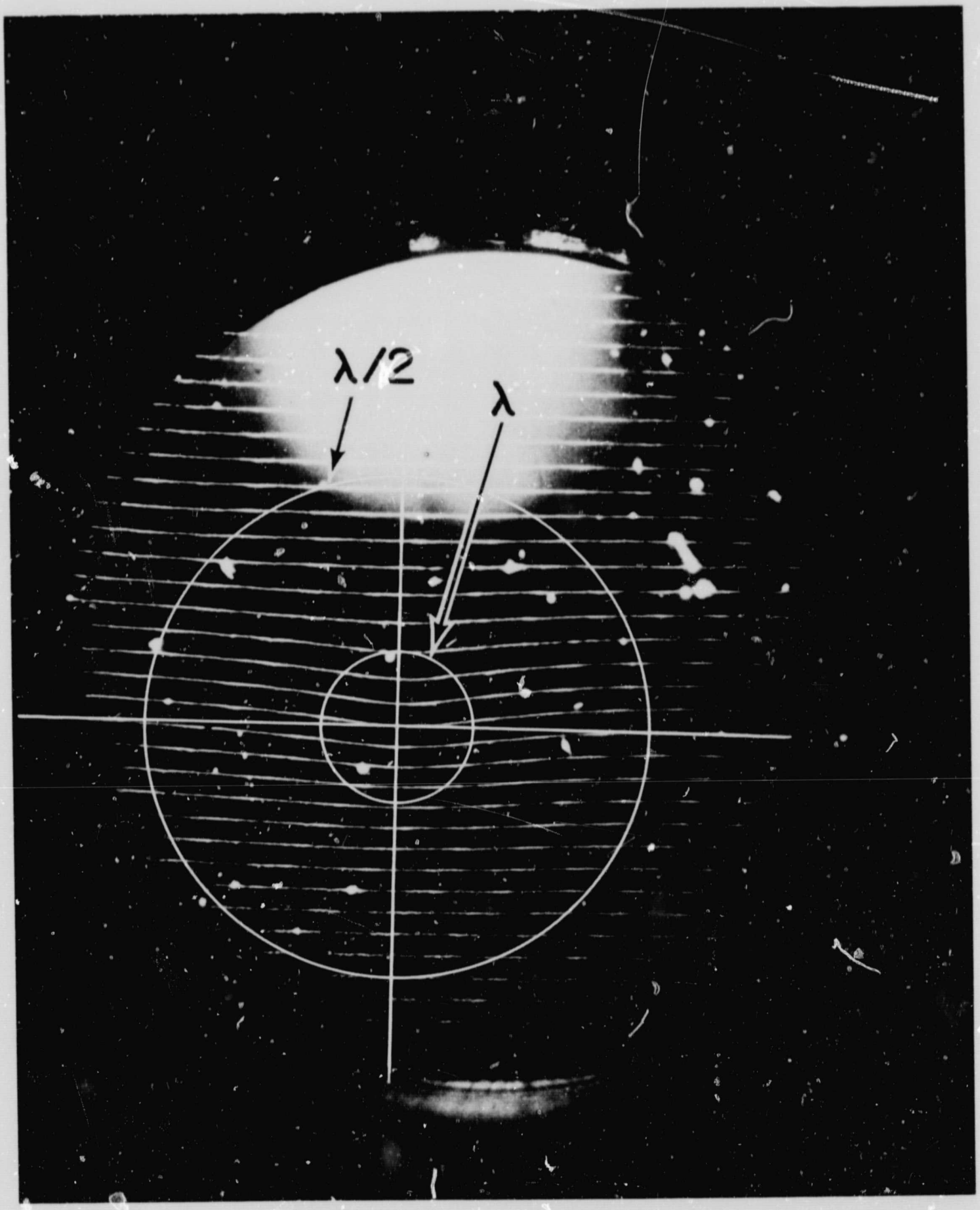

Figure B-5. Fizeau Fringe Pattern After 5 Minute Heating with a 1.3 Watt CO_2 Laser (3mm Beam Diameter)

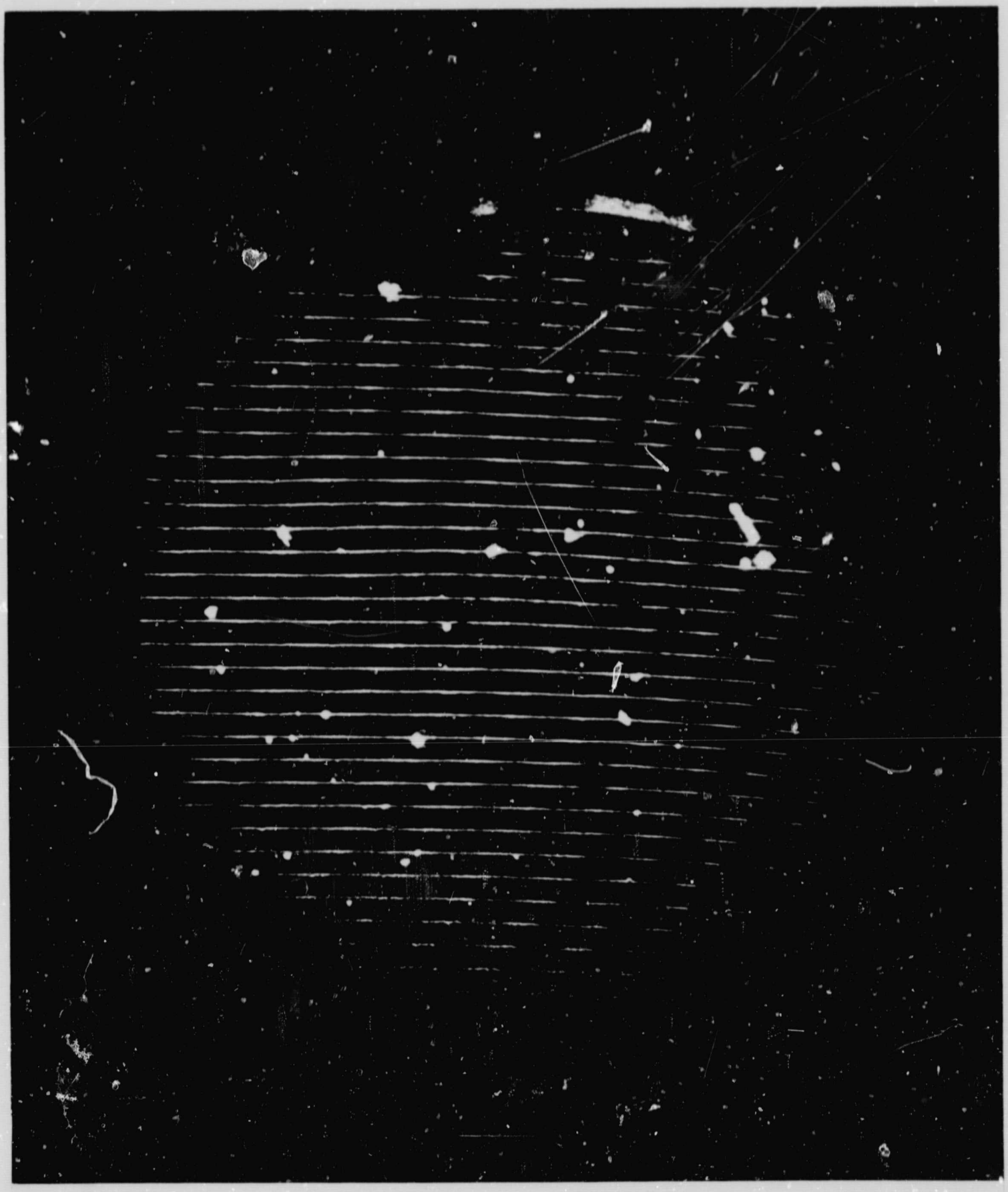

Figure B-6. Fizeau Fringe Pattern for the Unheated BaF_2 Substrate

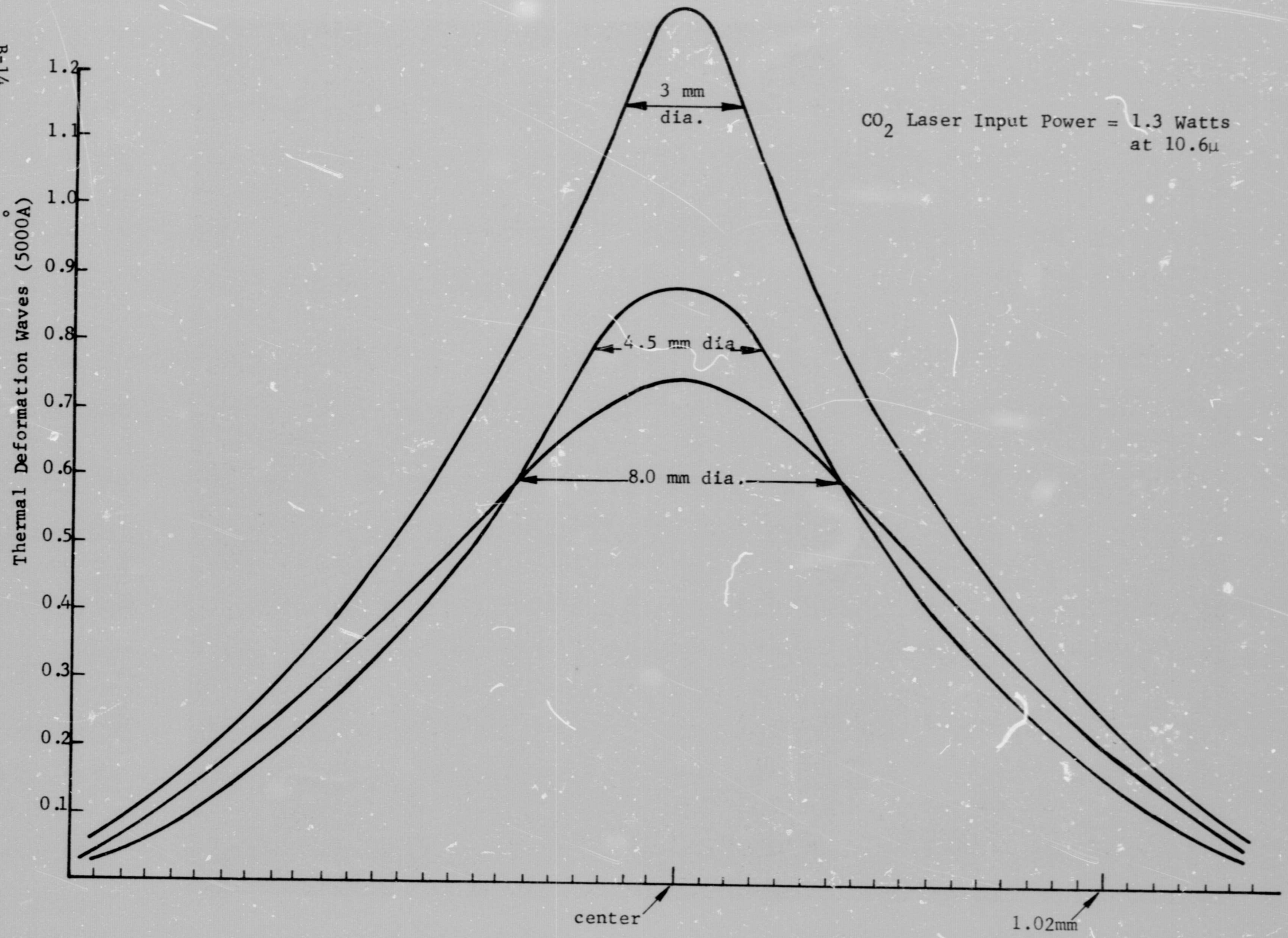

CO_2 Laser Input Power = 1.3 Watts at 10.6μ

Figure B-7 BaF$_2$ Dichroic Deformation for [illegible]

CO_2 laser power	1.3 watts	1.3 watts	1.3 watts
Beam diameter	4.0 mm	8.0 mm	10.0 mm
Temperature difference between center and a 1-cm radius (analytical)	2.1°K	0.85°K	0.5°K
Deformation (ΔZ) in waves (0.5 micron) (analytical)	0.65λ	0.27λ	0.16λ
Deformation (ΔZ) in waves (0.5 micron) (experimental)	0.75λ	0.55λ	

The surface deformation can be reduced by using a thinner substrate and larger diameter beams, but even for a 2-mm-thick substrate and an 8-mm-diameter beam the surface would be deformed by 1/10th wave producing wavefront distortions of 1/5th wave on reflection.

It is evident that even in low-power CO_2 laser applications, dichroic filters coated onto barium fluoride substrates will undergo substantial surface deformations. Therefore sodium chloride substrates should be used where 10.6μ laser power exceeds about 0.5 watt in an 8-mm-diameter beam provided that adequate precautions are taken against damage to the substrate by water vapor.

APPENDIX C

MODULATOR FOR 10.6-MICRON CO_2 LASER LIGHT

Several new solid state modulators have been proposed for CO_2 laser light in recent years and these are reviewed here with a view to choosing the most suitable one for systems use.

The most recent device utilizes field-induced free carrier absorption of 10.6-micron light at the surfaces of a semiconductor crystal (Ce).[1] The intensity of the laser beam is controlled by a modulation voltage applied to the crystal, which in turn controls the density of the space charge on the semiconductor surfaces. The device, as constructed, essentially traps the laser beam inside the crystal by total internal reflection and in this way the beam interacts with the surface space charge many times. Small signal analysis of the device shows that the modulation depth is proportional to the cube of the radiation wavelength but quantitatively amounts to only 1.5 percent at 10.6 microns for a drive voltage of 500 volts. The author states that a 40 percent modulation may be possible with a reasonable amount of development by using higher field strengths, reducing the surface state density, and by using absorption by holes rather than by electrons; however, the device has limited application since only amplitude modulation can be produced.

Ultrasonic diffraction has been used by several researchers[2,3] to produce both CW and pulsed modulation of 10.6-micron laser light. A modulation depth of 0.5 percent at 10.6 microns has been observed using an ultrasonic carrier frequency of 20 MHz[2] and 16 percent modulation obtained by using standing acoustic waves. Acoustic diffraction in crystals of tellurium[3] is

---

[1] D.W. Peters, Applied Optics, Vol. 6, No. 6, June 1967.

[2] H.R. Carleton and R.A. Soref, Applied Phys. Letters, Vol. 9, No. 3, Aug. 1966.

[3] R.W. Dixon and A.N. Chester, Applied Phys. Letters, Vol. 9, No. 5, Sept. 1966.

considerably more efficient (40 to 100 percent) since the amount of light diffracted is proportional to the cube of the crystal refractive index ($n^o \simeq 4.8$, $n^e \simeq 6.2$). Pulsed acoustic waves (2 μsec duration) were used in a 1 cm of tellurium to avoid acoustic resonances. Although theoretically capable of diffracting 100 percent of the incident radiation, Bragg effect devices are only suitable for amplitude modulation of CO_2 laser light.

An electro-optic modulator (RCA Model J2036VI) using a long crystal of gallium arsenide has been constructed by Walsh[4] and is capable of modulating the amplitude, phase, and polarization of a CO_2 laser beam over a 100 megacycle bandwidth. The device produces a modulation depth of 60 percent for a 700-volt rms signal at 10.6 microns and is also capable of efficient modulation at all wavelengths in the region 2 to 12 microns.

The performances of the three types of modulators are summarized in Table C-I and, as is evident, the electro-optic gallium arsenide modulator provides the only practical device at present.

---

[4]T.E. Walsh, R.C.A. Review, Vol XXVII, No. 3, Sept. 66.

TABLE C-I

SUMMARY OF MODULATOR CHARACTERISTICS

Modulator	λ	Drive Voltage	Power	Modulation Index	Bandwidth	Refs
Free Carrier Absorption in Ge	10.6μ	500V	-	12%	200 MHz	1
Acoustic Light Modulation Te, Si, GaAs, CdS	10.6μ	Pulsed	1/2W acoustic power	79%	20-300 MHz	2,3
GaAs Electro-Optic Modulators (RCA J2036V1)	10.6μ	700V	-	70%	100 MHz	4